Breaking Waves and the Dispersion of Surface Films

Ted Schlicke

A thesis submitted in fulfilment of the requirements

for the degree of Doctor of Philosophy

to the

University of Edinburgh

2001

Abstract

The techniques of Laser Induced Fluorescence (LIF) and Dual-Plane Particle Image Velocimetry (PIV) were applied to the investigation of breaking waves and the dispersion of surface films.

LIF was used to obtain widescreen images of the concentration distribution of a methanol-rhodamine B film after breaking. Five different wave amplitudes were studied, corresponding to a range of breaker types from weakly spilling to strongly plunging. Spatial and temporal information to quantify the dispersion was extracted from these images, such as the depth reached and area covered by the film, the motion of its centre of mass, dispersion coefficients and exponents, and the fractal dimension of the film-water boundary. The depth measurements and fractal dimension calculations compared well with related work.

All three velocity components of the water motion were measured using dual-plane PIV and a single camera. The vector maps obtained revealed the cascade from large to small scale vortices, and the transition from two to three dimensional flow after breaking. A 4-camera system was built, capable of producing sequences of images triggered in rapid succession up to a total of 120 frames per second. Each camera could be individually filtered, allowing the possibility of simultaneous PIV and LIF.

Declaration

I do hereby declare that this thesis was composed by myself and that the work described within is my own, except where explicitly stated otherwise.

Ted Schlicke

June 2001

Acknowledgements

Thank you to my supervisor Prof Clive Greated for his help and support thoughout. Many thanks also to the following people: Tim Dewhirst, Alistair Arnott, Jim Buick, Frank Morris, Andrew in the mechanical workshop; Colin, Jim and Andrew in the electronics workshop; Dr Will Hossack, Hequan Sun, Pablo Huq, Paul Addison, Neale Thomas, Peter Tuffy, Dr Francis Barnes and many other clever and helpful people, not least the secretaries and the librarians.

I'd especially like to thank family and friends who have provided encouragement during my time at Edinburgh, especially Alex, Mum and Dad; Mhairi, Fraser and the Sandeman family; Rebecca; Mike; Dippy and the teddies, and many others.

Thanks to the 4201 work-related-aquaintances : Susan, Anthony, Tom, Scott, Alix, Alistair, Dawn, David, Alan, Orlando, Mark, Narumon, the Johns and the rest of the fluids folk.

Finally, thank you to EPSRC for funding the first three years of my PhD.

Contents

List of Figures

List of Tables

Chapter 1

Surface Films and Breaking Waves

1.1 Background

Human beings, like all of the Earth's land-based creatures and plants, evolved from organisms which emerged from the oceans around 400 million years ago. Seemingly reluctant to move onwards, around half of the world's population lives within 200 kilometers of a coastline [1]. The oceans provide people with food, work, recreation and a dumping ground for waste, although the over-exploitation of any of these resources can be detrimental to the others. Covering 71% of the Earth, the oceans significantly influence the climate of the planet, and with the increasing impact of global warming, oceanography and atmospheric studies are

becoming more and more relevant. Yet much about the oceans remains to be explored: more people have been to the moon than to the deepest ocean floor, at the bottom of the Mariana trench.

1.2 Properties of Water

Each water molecule consists of one oxygen and two hydrogen molecules, held together by a covalent bond. Because it contains more protons, the shared electrons are attracted closer to the oxygen nucleus than the hydrogen nuclei, resulting in a dipole moment across the water molecule.

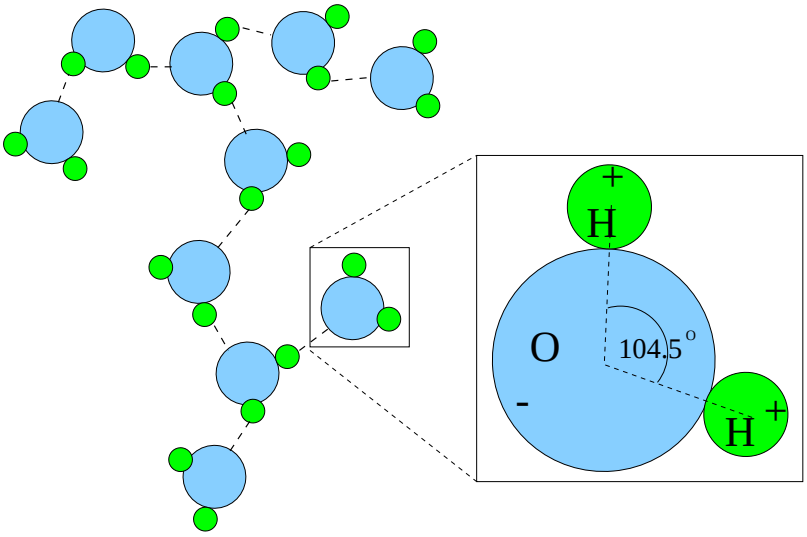

Figure 1.1: Hydrogen Bonding in water molecules

Since a water molecule has a positively and negatively charged end, it is attracted to other water molecules, forming *hydrogen bonds*. Despite being weak

and transitory, these bonds are responsible for some peculiar properties of water, for instance:

- High boiling point and specific heat capacity
- Maximum density at 4^oC; solid state less dense than liquid state
- Large cohesion and therefore high surface tension
- Powerful solvent, effective at dissolving ionic and polar-covalent molecules.

The high boiling point and specific heat occur because a great deal of energy is required to break the hydrogen bonds present between each water molecule. The large specific heat of water provides thermoregulation for all living beings, and moderates the ocean temperature and hence the climate of the Earth. Ice is less dense than water because of its regular crystalline structure, held together by hydrogen bonds.

If a water molecule is surrounded by others, it is attracted equally, on average, in all directions. At a free surface, however, water molecules experience a net attractive force towards the main body of the liquid. The mean separation of water molecules is therefore less at a surface, resulting in a skin resistant to deformation. This *surface tension* also accounts for water's tendency to form small spherical drops.

Without these and other unusual properties of water, life as we know it could not exist on Earth.

1.3 Water Waves

Surface waves are the most obvious form of oceanic movement. The discussion of waves will begin with some terminology. Waves are quantified in terms of their *wavelength* λ, the distance between two consecutive crests, *frequency* f, the number of waves passing a fixed point in one second, *local wave height*, H, the vertical difference between the trough and crest and the *amplitude*, a, equal to $\frac{H}{2}$ (figure 1.2).

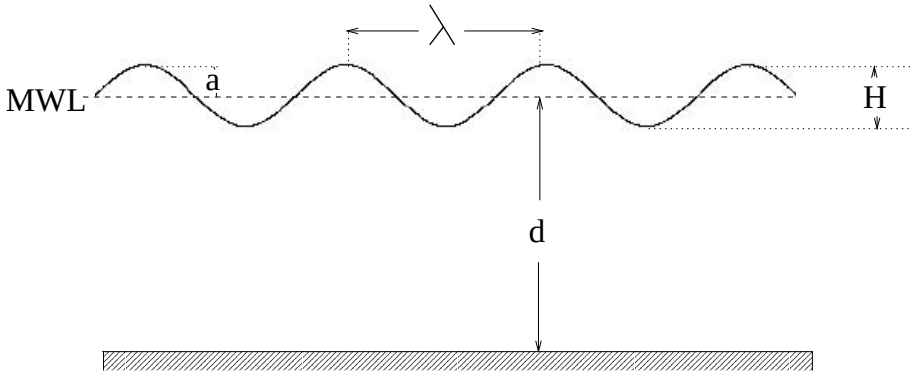

Figure 1.2: Definition of some wave parameters

Related to these are the *wavenumber* $k = \frac{2\pi}{\lambda}$ and *angular frequency* $\omega = 2\pi f$. The *water depth* d is defined as the distance between the water bed and the *mean water level*, MWL.

The mean slope between the wave node and crest equals $\frac{4a}{\lambda}$, or $\frac{2ak}{\pi}$. The non-dimensional parameter ak is thus a measure of the steepness of a wave. In the experiments described in this thesis, k has a constant value of $3.17m^{-1}$, so ak can

also be thought of as a non-dimensional amplitude.

There are three principal mechanisms for the generation of surface waves. Wind is a pressure fluctuation in the atmosphere caused mainly by the temperature difference between the tropics and the poles. The pressure variations create shear stresses on the surface of the water and result in tiny ripples. These disturbances produce roughness on the surface and provide additional area for the wind to act against, resulting in positive feedback. The waves grow both in wavelength and amplitude as momentum is transferred from the wind to the sea, until the phase speed of the water equals the wind speed.

The tides are a large scale wave motion caused predominantly by the gravitational attraction of the sun and moon. The lunar and solar orbits are elliptic and precess, resulting in a number of tidal frequencies. The semidiurnal and diurnal tides have periods of approximately 12 and 24 hours respectively. Examples of longer tidal periods include the spring and neap tides, and the annual solar tide [2].

Finally, waves can occur as a result of a sudden displacement of water. The scale of these waves ranges from small ripples caused, for instance, by falling raindrops, to mega-tsunamis, waves up to and above $500m$ in height, the result of large volcanic landslides or asteroid impacts. Waves of intermediate amplitude include wakes from ships and tsunamis, produced by underwater earthquakes.

1.3.1 Mathematical Description of Water Waves

Two restoring forces, gravity and surface tension, are responsible for the vertical accelerations of surface oscillations. These disturbances can be described mathematically using potential theory by solving Laplace's equation with the appropriate boundary conditions [3]. This linear theory applies if the amplitude of the wave is assumed to be small relative to the wavelength and water depth. The *dispersion equation*, which relates angular frequency to wavenumber, can then be written as

$$\omega^2 = \left(gk + \frac{\sigma k^3}{\rho}\right) \tanh(kd) \tag{1.1}$$

where g is the gravitational acceleration ($9.81 ms^{-2}$), σ is the surface tension of water ($73 mN m^{-1}$ at room temperature), ρ is its density ($1 gcm^{-3}$) and d is the water depth. In this context, dispersion refers to the fact that the celerity C (also known as the phase speed) of a wave, the speed of propagation of the disturbance, depends on its wavenumber:

$$C = \frac{\omega}{k} = \sqrt{\left(\frac{g}{k} + \frac{\sigma k}{\rho}\right) \tanh(kd)} \tag{1.2}$$

Since an arbitrary wave can be considered to be made up of a number of waves of different wavenumbers, in general a surface disturbance will tend to

spread out as it propagates. In much of the rest of this thesis, *dispersion* will be taken to mean one distinct physical phase in the presence of another, specifically a pollutant within water. This definition will be discussed in much greater detail in section 6.7.

The water depth is considered *deep* when the waves are not significantly affected by the bottom. The same depth of water can be deep for short waves yet shallow for waves of long wavelength; indeed, the entire ocean is effectively shallow for tidal waves. Water is usually termed deep when $\frac{d}{\lambda} > \frac{1}{2}$, or $kd > \pi$ [4]. Then $\tanh(kd)$ tends to one and the celerity is independent of depth. A graph of celerity against wavelength in deep water is shown in figure 1.3.

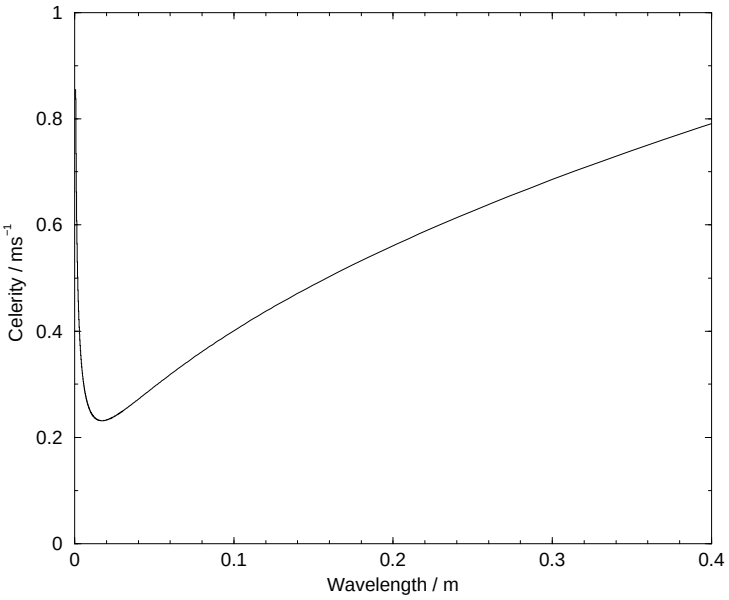

Figure 1.3: Graph of Celerity against Wavelength

The graph has a minimum speed of $23cms^{-1}$ at a wavelength of approxi-

mately $1.7cm$. For wavelengths less than this, surface tension is the predominant restoring force; such waves are termed *capillary* waves and their phase speed increases with decreasing wavelength. At larger wavelengths, the first term under the square root sign in equation 1.2 dominates and the resulting disturbance is called a *gravity* wave whose celerity increases as $\sqrt{\lambda}$.

In shallow water, $\tanh(kd)$ can be approximated by the first term in the Taylor expansion, kd. The celerity is then $C = \sqrt{\left(g + \frac{\sigma k^2}{\rho}\right) d}$. The two terms within brackets, g and $\frac{\sigma k^2}{\rho}$, are equal when the wavelength is $1.7cm$. The second term decreases rapidly with increasing wavelength; at $5.4cm$, it is less than 10% of g. Thus for gravity waves, the phase speed can be closely approximated by $\sqrt{gd}$ and is independent of wavenumber. This allows the possibility of non-dispersive waves.

Real waves tend to consist of a number of waves of different frequencies and wavelengths. To determine how such a group would move, consider just two sinusoidal waves of frequency ω_1 and ω_2, wavenumbers k_1 and k_2 and each of amplitude a. The surface elevation due to the superposition of these waves, $\eta(x,t)$, is then

$$\eta(x,t) = a\cos(\omega_1 t - k_1 x) + a\cos(\omega_2 t - k_2 x) \tag{1.3}$$

Using the trigonometric identities, this can be rewritten as

$$\eta(x,t) = 2a\cos\left(\frac{\omega_1+\omega_2}{2}t - \frac{k_1+k_2}{2}x\right)\cos\left(\frac{\omega_1-\omega_2}{2}t - \frac{k_1-k_2}{2}x\right) \tag{1.4}$$

If it is assumed that the two waves have similar periods, and therefore similar wavenumbers, then the surface elevation of equation 1.4 can be considered to consist of a high frequency oscillation, $cos\left(\frac{\omega_1+\omega_2}{2}t - \frac{k_1+k_2}{2}x\right)$, modulated by a low frequency envelope, $\cos\left(\frac{\omega_1-\omega_2}{2}t - \frac{k_1-k_2}{2}x\right)$; see figure 1.4.

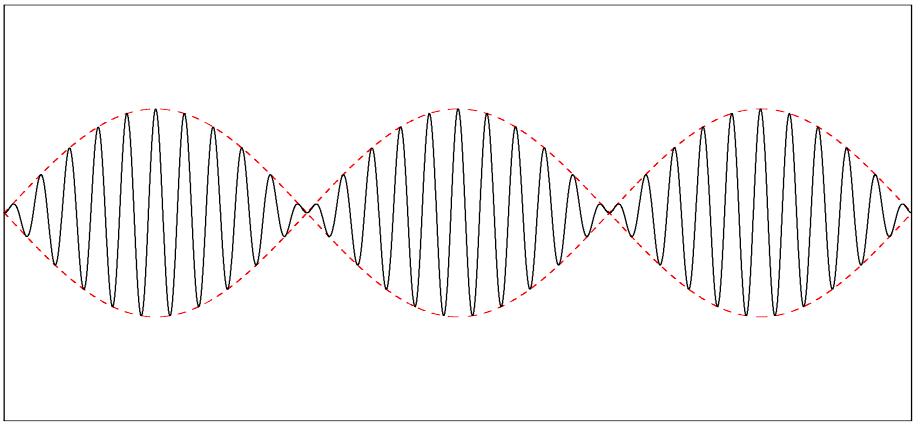

Figure 1.4: Superposition of two sinusoids

The rapidly varying oscillation travels at a speed $\frac{\omega_1+\omega_2}{k_1+k_2}$, or $\frac{\omega_m}{k_m}$ where ω_m is the mean angular frequency and k_m is the average of the two wavenumbers. This the equivalent to the phase speed introduced in equation 1.2. The speed of the envelope, meanwhile, is $\frac{\omega_1-\omega_2}{k_1-k_2}$. The *group speed*, C_g, is defined as the limit as k_1 approaches k_2; that is, the derivative of equation 1.1:

$$C_g = \frac{d\omega}{dk} = \frac{C}{2}\left[1 + \frac{2\sigma k^2}{g\rho + \sigma k^2} + \frac{2kd}{\sinh(2kd)}\right] \tag{1.5}$$

The energy contained within such a group is proportional to the square of the wave amplitude. Because this energy is conserved, it must propagate with the group.

The energy of gravity waves in deep water therefore travels at half of the phase velocity, and at the phase velocity in shallow water. Conversely, the energy contained within capillary waves travels at $\frac{3}{2}$ times the speed of the surface profile. When gravity waves are observed in deep water, therefore, they appear at the rear of a group, advance forward because the phase velocity is greater than the group velocity, and vanish at the front of the group. Ripples, on the other hand, appear to form at the front of a group, moving backwards relative to the group before disappearing at the rear.

The trajectories of the water motion as waves pass can also be determined by manipulating the potential function [3]. In deep water, the particles have circular trajectories whose diameter decreases exponentially with depth. In shallow water, the particles move in ellipses whose vertical axis increases linearly from zero at the bottom to H at the mean water level. At intermediate depths, the particle trajectories are a combination of these motions (figure 1.5).

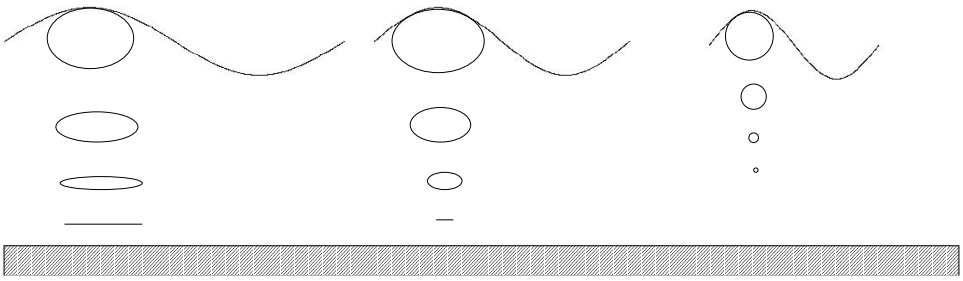

$\frac{h}{\lambda} < \frac{1}{20}$ $\qquad \frac{1}{20} < \frac{h}{\lambda} < \frac{1}{2}$ $\qquad \frac{h}{\lambda} > \frac{1}{2}$

Figure 1.5: Water trajectories

1.3.2 The Surf Zone

A gravity wave approaching a coastline will slow down and refract towards the normal of the shoreline, completely analogous to the bending of light due to changes in refractive index (figure 1.6). Another important property of waves travelling towards shallower water is that their amplitude increases. If it is assumed that no reflection occurs as waves approach the shore, the conservation of energy flux states that

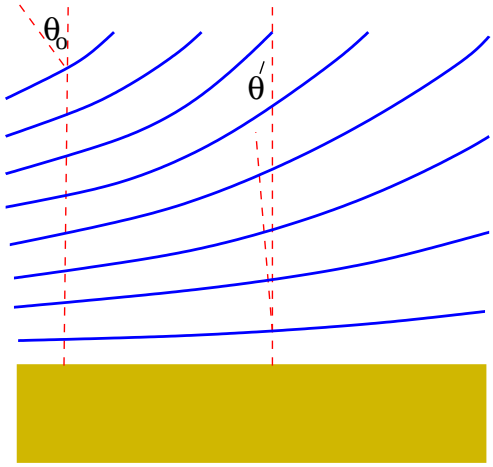

Figure 1.6: Refraction of water waves

$$H' = H_0 K_s K_r \tag{1.6}$$

where H_0 is the initial wave amplitude, H' is the new amplitude, and K_s and K_r are the shoaling and refraction coefficients respectively. K_s is given by $\sqrt{\frac{C_0}{2C_g}}$, where C_0 is the deep water celerity and C_g is the local group velocity. K_r can be expressed as $\left(\frac{1-\sin^2\theta_0}{1-\sin^2\theta'}\right)^{\frac{1}{4}}$, where θ_0 and θ' are the initial and final angles to the shore. Since θ' is always less than θ_0, K_r is always less than unity. K_s, however, can increase without limit since the group velocity tends to zero as the water depth decreases. This suggests that the height of a wave could tend to infinity as it approaches the shore.

1.3.3 Breaking Waves

Clearly, infinitely high waves do not occur. As the wave amplitude rises, the assumptions of linear theory are violated, and the equations above are no longer valid. Instead, the wave becomes unstable and breaks, dissipating energy via turbulence and friction.

There are several definitions of the precise moment of breaking. It is often considered to occur when the wave front becomes vertical but this does not happen in all breaking events [5]. McCowan [6] was the first to define a breaking criterion, stating that a wave will break if the ratio of wave height to water depth, $\frac{H}{d}$ exceeds 0.78. This neglects the fact that wave breaking occurs in deep as well

as shallow water. Another possible condition is that the fluid velocity at the crest exceeds the phase velocity at breaking. The drawback of this definition is that the phase velocity is not well defined in highly non-linear waves. Perhaps the most useful definition is that breaking occurs when the wave slope, ak, exceeds a critical value, equal to approximately 0.32 [7].

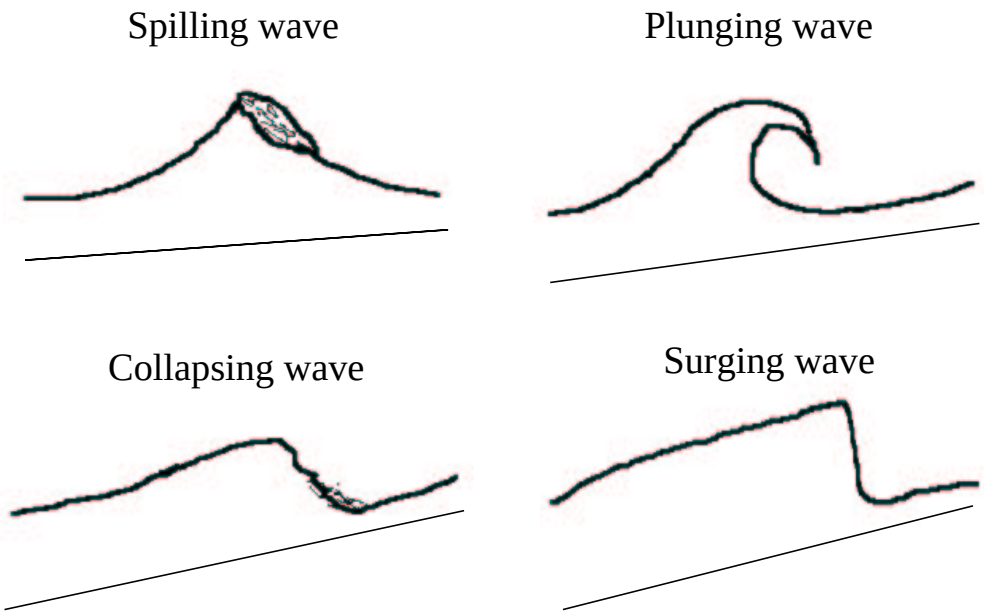

Figure 1.7: Four types of breaking wave

It is generally accepted that there are four types of breaking wave: spilling, plunging, collapsing and surging.

In *spilling* breakers, the crest becomes unstable and flows down the front part of the wave, resulting in frothy water remeniscient of a bore. In the surf zone, spilling occurs when steep waves advance up a gentle beach and continues over a number of wavelengths.

Plunging is the most dramatic form of breaking, with the crest curling over and crashing into the water below, creating a large splash which advances like a bore. Plunging occurs on slightly steeper beaches and often within a single wavelength.

Surging occurs on the steepest beaches: the crest does not break, but the base of the wave's front face advances rapidly up the beach with mild breaking and significant reflection.

Collapsing is the most recent classification of breaker, between plunging and surging, where the crest itself does not break but the lower part of the front face steepens and falls, creating a foamy surface which slides up the beach.

Of these, only spilling and plunging occur in deep water as well as on beaches. The surface profile of each type of breaker is indicated in figure 1.7.

Experiments by Duncan [8] have shown that during the breaking process, a bulge initially forms at the front of the wave crest. Either side of the leading edge of this bulge, known as the *toe*, parasitic capillary waves are formed; those above the toe tend to have longer wavelengths than those below the toe.

The linear theory outlined above cannot predict the profiles of these breaking waves. Stokes was the first to develop a non-linear theory of wave motion, using a perturbation method to extend the description to third order, and higher order approximate solutions have since been obtained [9]. In order to describe wave

deformation, numerical methods such as the boundary integral method and the Boussinesq model have been developed [10]. Longuet-Higgins has accounted for the high-frequency detail present in breaking waves in terms of crest-instabilities. He further suggests that the troughs of these capillary waves provide a source of vorticity, and that viscosity and surface tension are significant for waves up to $2m$ in wavelength [7].

Although these models can accurately describe the wave deformation up to breaking, they cannot account for the profile or subsequent water motion after breaking occurs. For this reason, much of the research into post-breaking eddy formation and the development of turbulence has been experimental. The majority of wave breaking experiments are carried out in wave tanks due to the difficulty in obtaining repeatable measurements in the ocean itself.

Chang and Liu [11] measured velocities in the overturning tip of breaking waves and found that after the jet collapses, it creates a coherent horizontal vortex. The splash-up produced by plunging breakers forms secondary eddies downstream. In addition, random oblique eddies are formed which suggests that while the water velocity prior to breaking is essentially two-dimensional, three dimensional structures develop after breaking. This transition from 2d to 3d motion has also been measured in the field [12].

Lin and Liu [13] stated that the primary horizontal vortex diffuses rapidly into the interior of the fluid after breaking due to strong eddy viscosity at the

surface. Advection, molecular diffusion and vortex stretching then redistribute the vorticity and form turbulence cascades, by which the energy of large vortices is transferred to small, isotropic vortices.

Haydon [14] and Emerat [5] conducted experiments to investigate the evolution of post-breaking turbulence in deep water and on a beach respectively, for a number of waves. Their research found that plunging breakers generate stronger vorticity and greater turbulent energies than spilling breakers.

Emerat noted that aerated water in the flow affects the transport of vorticity. The presence of bubbles also hinders the acquisition of accurate velocity measurements [13]. The entrainment of air bubbles is a process which qualitatively changes at different scales: bubble formation is disproportionally small in most laboratory experiments [15]. Furthermore, surface tension and viscosity have greater relative importance in small scale wave processes, and most wave flumes use fresh rather than salty water [16]. These factors mean that scaling laboratory results such that they can be applied to real oceans is not easy.

In these experiments, the scaling approach used by Rapp and Melville [17] is adopted. They characterised waves in terms of non-dimensional parameters such as amplitude ak and frequency bandwidth, $\frac{\Delta f}{f_c}$. That is, distances are non-dimensionalised by multiplication with the central wavenumber, while non-dimensional times are obtained by multiplying the actual time by the central angular frequency of the wave.

1.4 Surface Films

Approximately 96.5% of the oceans, by volume, is water. The other 3.5% consists of dissolved salts, organic material, particles and gases and has a large influence on oceanic circulation and the climate [18]. The interaction of organic material with the water surface, for instance, affects the wave motion discussed in the previous section.

A *surfactant*- SURFace ACTive AgeNT- is a material whose properties change at a surface or, more generally, any fluid interface.

Organic molecules frequently contain either hydroxyl (OH group) or carboxyl (COOH) groups which are termed *hydrophilic* because they are readily adsorbed by water molecules. Long carbon chains, however, are *hydrophobic* as they are reluctant to interact with water. Thus organic molecules frequently accumulate at the surface, with the OH groups orientated towards the water ions and the long chains at the water-air boundary (figure 1.8).

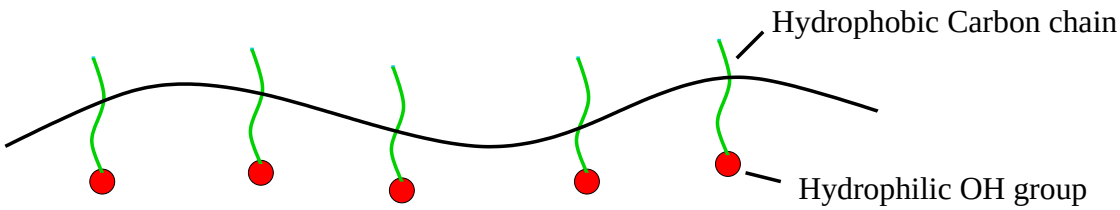

Figure 1.8: Orientation of Organic Molecules

This accumulation of organic molecules reduces the number of hydrogen bonds

at the surface, and hence lowers the surface tension. It is believed that phytoplankton, which produce natural surfactants as byproducts of their metabolism, are the largest single source of surfactants. Petroleum products, decaying vegetation and wastewater discharges also produce surface films of surfactant material [19].

Surfactants are often defined as materials which reduce surface tension and have practical uses as detergents, foaming agents and so on. Some inorganic salts and other highly ionic materials *increase* the surface tension of water slightly, but are often more energetically stable away from the surface, so are not generally termed surfactants [20]

Equation 1.2 suggests that the reduction of surface tension will decrease the celerity of capillary waves and have little direct effect on gravity waves. Of more significance is the fact that the surface tension is also non-uniform in the presence of surfactants; in the next section, the effect of this will be discussed.

1.4.1 Damping by Surface Films

The presence of surfactants, even a film of mono-molecular thickness, can dramatically damp water waves. This effect was first investigated scientifically by Benjamin Franklin in 1774, who conducted experiments with oil films on Clapham Common and at sea [21]. But the calming effect of oil on waves has

been known for at least 2000 years [22] and the expression *to pour oil on troubled waters* is a well-known metaphor in popular language.

Damping is a consequence of the boundary condition at the surface, which states that the sum of the surface stresses must be equal and opposite to the sum of the viscous stresses [23]. For pure liquids, the surface tension is approximately uniform, so the surface stress and hence the viscous stress vanish. The flow beneath the surface is essentially potential in the absence of surfactants, and little damping therefore occurs. If the surface is covered by a film, however, the periodic contractions at the front of the wave and expansions at the rear introduce gradients in the surface tension and thus result in finite viscous stresses. These viscous stresses introduce large velocity gradients which in turn cause significant damping.

The amount of damping is dependent on the *surface dilational modulus*, ϵ, defined by

$$\epsilon = \frac{d\sigma}{d \ln A} \tag{1.7}$$

which describes how surface tension σ changes with a change in a surface element A. The value of ϵ varies from zero for a clean surface to infinity for a completely inextensible surface.

Damping can be quantified as a decrease in wave amplitude either over dis-

tance or time. Lucanssen [23] defined a complex wavenumber $k = k_0 - i\beta$ and frequency $\omega = \omega_0 + i\alpha$ where β is a distance damping coefficient and α is a time damping coefficient. The amplitude of a wave travelling in the x direction, $y(x,t)$, in complex notation is given by

$$y(x,t) = Ae^{ikx+i\omega t} \tag{1.8}$$

$$= Ae^{\beta x}e^{-\alpha t}e^{i(k_o x+\omega_0 t)} \tag{1.9}$$

At low viscosity, the ratio of α to β is equal to the group velocity, $\frac{d\omega}{dk}$.

The temporal damping coefficient of a wave of wavenumber k and angular frequency ω can be approximated by [24]

$$\alpha = \frac{1}{2}k\delta\omega\frac{1+2k\delta\gamma(\gamma-1)}{(\gamma-1)^2+1} \tag{1.10}$$

δ is the width of the viscous shear layer and γ is a dimensionless parameter given by

$$\gamma = (2\nu)^{\frac{1}{2}}\rho C_s\omega^{\frac{3}{2}}k^{-2} \tag{1.11}$$

Here, ν is the kinematic viscosity of the water and C_s is proportional to $\frac{1}{\epsilon}$. If δ

is given by $\sqrt{\frac{2\nu}{\omega}}$, [25], equation 1.10 can be rewritten as

$$\alpha = \sqrt{\frac{\nu\omega k^2}{2}} \quad \frac{1 + \sqrt{\frac{8\nu k^2}{\omega}}\gamma(\gamma - 1)}{(\gamma - 1)^2 + 1} \tag{1.12}$$

For clean water with no film present, $\epsilon = 0$, $\gamma = \infty$ and the damping coefficient is

$$\alpha_{\gamma=\infty} = 2\nu k^2 \tag{1.13}$$

At the other extreme, for a film of infinite dilational modulus, $\gamma = 0$ and the damping coefficient is given by

$$\alpha_{\gamma=0} = \frac{1}{2}\sqrt{\frac{\nu\omega k^2}{2}} \tag{1.14}$$

These two results were obtained independently by Lamb [26].

A graph of $\frac{\alpha}{\alpha_{clean}}$ against $\frac{1}{\gamma}$, generated using equation 1.12 for several values of k, is shown in Figure 1.9. Significantly, maximum damping occurs not if $\gamma = 0$, but rather when γ is approximately equal to 1. The maximum damping coefficient is then

$$\alpha_{\gamma=1} = \sqrt{\frac{\nu\omega k^2}{2}} \tag{1.15}$$

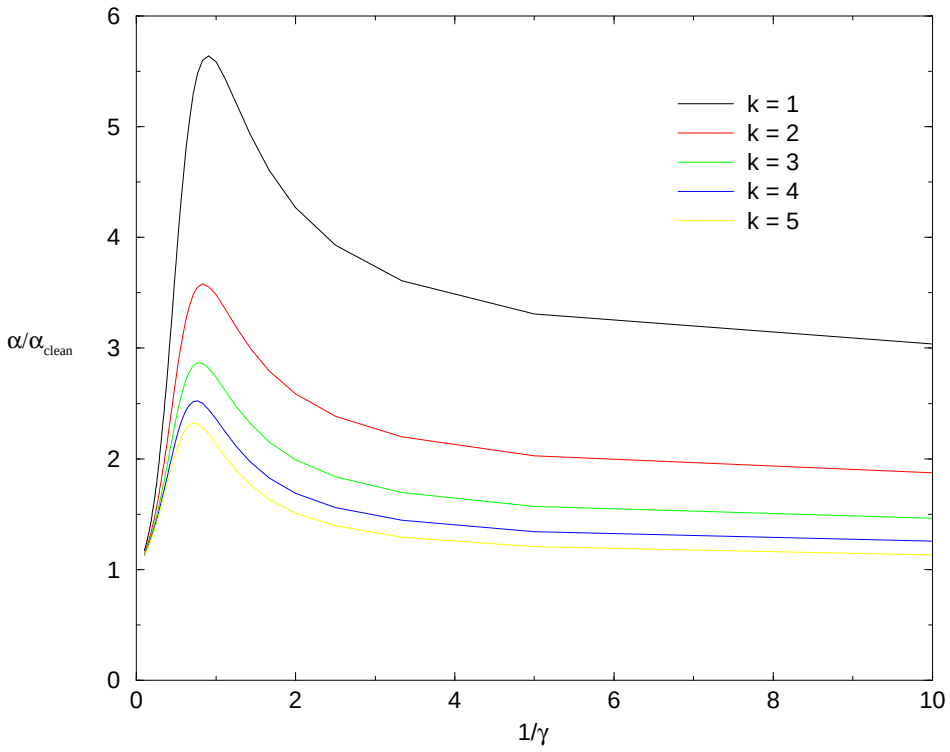

Figure 1.9: Graph of damping coefficient against dilational modulus

or twice the value for the inextensible film. This maximum occurs because the variation in surface tension allows the possibility of longitudinal wave motion, in addition to transverse oscillations, as a solution of the governing wave equations [27]. These longitudinal wave disturbances are called Marangoni waves. At $\gamma \approx 1$, these two motions have the same wavelength but are out of phase, which results in resonant damping.

Because damping is the result of variations in surface tension, one might expect that capillary waves rather than gravity waves are affected. However, the ratio of damping coefficients of a surface with finite dilational modulus to a clean surface where $\gamma = \infty$ actually increases with wavelength, as can be seen in figure

1.9. This suggests that waves of longer wavelength will be damped more rapidly in comparison to a clean surface than shorter waves.

As the wavelength increases, C_s in equation 1.11 must decrease in order for γ to equal unity for maximum damping. Thus the dilational modulus ϵ must increase as λ increases. For many surfactants, ϵ is of the order $20mNm^{-1}$ or less, which is insufficient to cause significant damping of gravity waves. In practice, therefore, damping by surface films does primarily affect capillary waves.

Nevertheless, gravity waves are still influenced indirectly by the presence of surfactants. By damping ripples, the surface of the water becomes aerodynamically smoother, and so wave growth due to the action of the wind is suppressed. Also, a smoother surface has fewer high frequency components and is therefore less likely to break. The presence of a surface film can thus be sufficient to inhibit or suppress breaking completely.

This could have practical applications, since the sudden dissipation of energy which occurs at breaking can be hazardous to ships, oil rigs and coastal structures. In 1887, Shields poured oil into the sea at Aberdeen and Peterhead, and noted that the wave action at the harbour entrance was diminished [28]. But the difficulties in obtaining conclusive results in the field, and environmental concerns, mean that the deliberate contamination of the ocean surface has not been widely adopted.

A further feature of the presence of surfactants is that the trajectories of the fluid motion become approximately elliptical, due to a reduction in the horizontal motion. Also, there is a finite angle between the minor axis and the vertical, which increases as the film concentration rises [25].

1.4.2 Dispersion of Surface Films

A surface film on the ocean will tend to disperse horizontally. There are a number of mechanisms responsible for this dispersion, such as eddy diffusivity, turbulence and advection, and in practice it is difficult to compare the significance of each. Dispersion measurements frequently involve recording the motion of a number of tracers over long periods of time and results have shown that the rate of dispersion increases with scale [29]. At smaller scales, random variations in the Stokes drift due to wave action have been predicted [30] and found experimentally [31] to cause dispersion. Measurements obtained by Sanderson and Booth [32] and Osborne [33] suggest that horizontal dispersion in the oceans can be effectively modelled by fractional Brownian motion, which will be discussed in section 6.7.4.

By performing these dispersion experiments, information about the nature of oceanic movement is gained. In turn, this knowledge could be used to help predict the spreading of the 700 million gallons of oil which enters the world's oceans each year.

Surfactants generally remain at the surface of the water, even in the presence of strong wave action. Significant dispersion beneath the surface occurs only when the surface itself is broken, for instance after wave breaking. In the previous section, it was noted that the presence of surfactants can suppress breaking. Thus surface films inhibit the mechanism primarily responsible for their dispersion beneath the water surface.

1.5 Aim and Overview of thesis

The purpose of this research is to investigate the mixing of surface films after wave breaking. Particular emphasis is placed on the downward dispersion, which has not been widely studied. Although Rapp and Melville [17] measured the extent of post-breaking mixing, detailed concentration measurements of the mixing distribution have not been obtained prior to this study.

A further aim of this work is to measure the three-dimensional water velocities after breaking occurs. This is to establish which features of the flow are most responsible for the redistribution of the surface contaminant.

The experimental apparatus used to carry out this research is described in the following chapter. Two experimental techniques are used to study the dispersion: *Laser Induced Fluorescence*, LIF, and *Particle Image Velocimetry*, PIV. LIF is used to obtain concentration measurements of a film, and is described in detail

in chapter 3.

PIV yields velocity information about the flow and is discussed in chapter 4, while chapter 5 describes the 4 camera system build for the dual-plane PIV experiments .

The image processing of the LIF images is covered in chapter 6, and the results obtained from the LIF experiments are presented in chapter 7.

The PIV experimental results are included in chapter 8. Finally, conclusions and proposals for further work are reviewed in chapter 9.

Chapter 2

Experimental Apparatus

2.1 Introduction

The Navier-Stokes equation, which describes all fluid motion, was first derived nearly 200 years ago but, because of its non-linearity, it can be solved analytically in only the simplest of flows. Thus, despite being a classical theory, much progress in fluid dynamics has been made only relatively recently, with the rapid development of computer power, lasers and camera technology. This chapter reviews the equipment common to both the LIF and PIV experiments; descriptions of the precise experimental set-ups are provided in chapters 3 and 8 respectively.

2.2 Wave Tank

The majority of the experiments described in this thesis were carried out in the wave flume built by David Skyner [34], and known locally as the *Green Tank*; see figure 2.1.

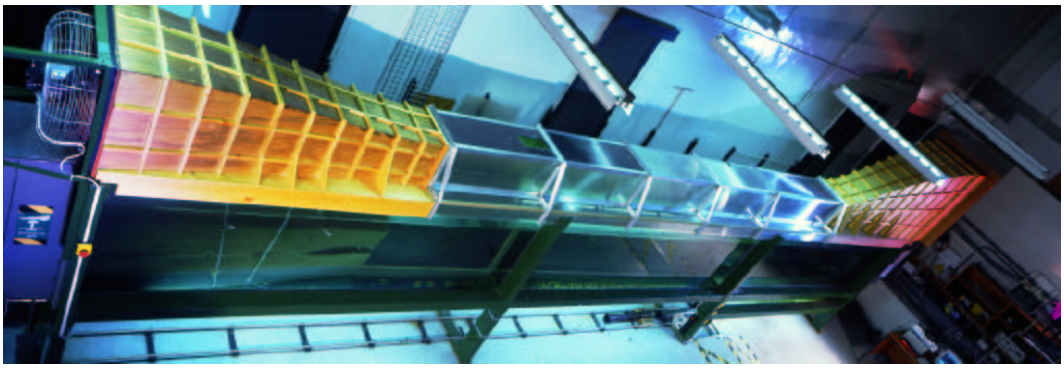

Figure 2.1: "The Green Tank"

The tank is $9.77m$ long, $0.40m$ wide with a mean water depth of $0.75m$. At one end of the tank is an absorbing, computer-controlled wave paddle, which can generate waves of user-specified amplitude, frequency and phase. Breaking waves can be generated using the property of dispersion described in section 1.3.1, which states that celerity is dependent on wavelength in deep water. Waves of different frequencies are produced such that they focus at the required time and location down the tank, interfering to create a profile of critical steepness which then breaks.

At the opposite end of the tank from the wave paddle is a foam beach designed to inhibit wave reflections.

The tank is capable of generating a mean current along the tank and has a wind tunnel which can generate steady wind speeds of up to $6ms^{-1}$ along the water surface. However neither of these facilities was used in the course of these experiments to reduce the number of variables influencing the dispersion.

The paddle is capable of of generating waves of frequencies between approximately $0.5Hz$ and $1.6Hz$. Thus the minimum wavelength produced by the paddle is around $60cm$. Because this wavelength is significantly larger than $1.7cm$, the value at which gravity and surface tension are equally important, it is not believed that the films used in these experiments will have a discernible effect on the wave profile.

The central frequency, f_c, of the breaking wave packets was $0.88Hz$, and the frequency spread Δf was $0.6424Hz$, leading to a frequency bandwidth of $\frac{\Delta f}{f_c} = 0.73$. The central wavenumber of the packet is $3.17m^{-1}$, and five different amplitudes were investigated: $9.9, 10.2, 10.5, 10.8$ and $11.1cm$. The largest of these, $ak = 0.352$, was also used by Rapp and Melville [17], with the same frequency bandwidth, allowing a direct comparison of results.

2.3 Laser Illumination

An Argon-Ion laser was used to illuminate a vertical plane through the centre of the wave tank. This laser has a maximum output of $15W$ and produces a

number of wavelengths, most prominent of which are the $488nm$ and $514nm$ lines, resulting in a green beam.

The radius of the beam at the aperture of the laser is $0.79mm$, and its divergence, θ, is $0.56mrad$. The laser is located in a separate room to the wave tank, and the path length between the laser aperture and scanning beam box is approximately $9m$. Over this distance, the beam spreads to a diameter of approximately $10mm$. In order to control the beam thickness and reduce its divergence, collimating optics are required. The beam divergence can be cancelled out by inserting two lenses, one converging and one diverging, into the beam path, as shown in figure 2.2.

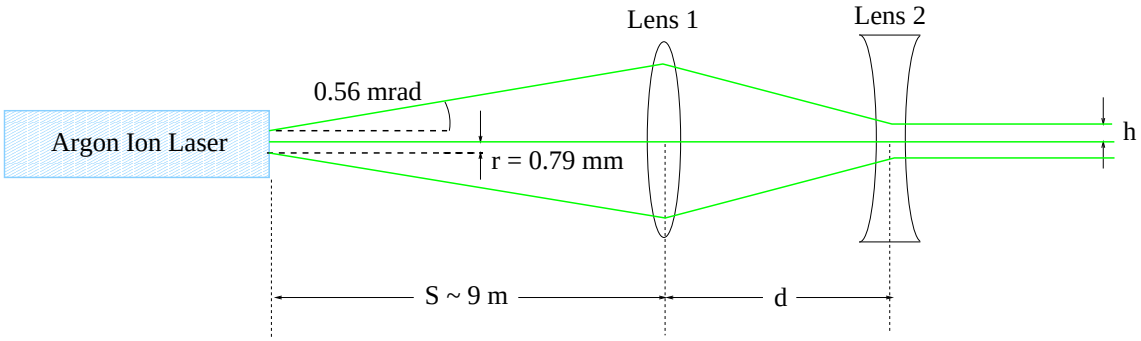

Figure 2.2: Light Sheet Collimating Optics (not to scale)

If the distance from the aperture to the collimating optics is S, the required light sheet radius is h and the focal length of lens 1 is f_{l_1}, then the focal length for lens 2, f_{l_2}, and the lens separation, d, required to collimate the beam are given by:

$$f_{l_2} = -\frac{f_{l_1} h}{r + (S - f_{l_1}) \tan\theta} \tag{2.1}$$

$$d = \frac{f_{l_1}(r + S\tan\theta - h)}{r + (S - f_{l_1}) \tan\theta} \tag{2.2}$$

In the LIF experiments, the focal lengths of lens 1 and 2 were $+200mm$ and $-25mm$ respectively. This produced a collimated beam when the lens separation was $18cm$. It was noticed that the actual beam diameter, $2h$, was larger than the $1.43mm$ predicted by the equations above. The reasons for this will be discussed in section 8.2.3, which describes the measurement of the beam profile.

In order to illuminate a significant section of the wave tank, the beam is converted into a pseudo-lightsheet. This is done using a *Scanning Beam Box*, developed by Gray [35] and shown in figure 2.3.

The beam is reflected onto a rotating octagonal mirror, located at the focus of a parabolic mirror. The rotational frequency of the octagonal mirror is set by a motor and can range from $25Hz$ to $250Hz$. For each revolution of the mirror, the laser beam sweeps across the parabolic mirror eight times. Because the beam arrives from the focus of the parabola, it is reflected to the vertical, creating the appearance of a steady sheet of light. If the form of the parabola is expressed as $y = \frac{x^2}{2L}$, where L is the radius of curvature, then the focus is located at a height $\frac{L}{2}$. The horizontal length of the parabolic mirror is equal to the radius

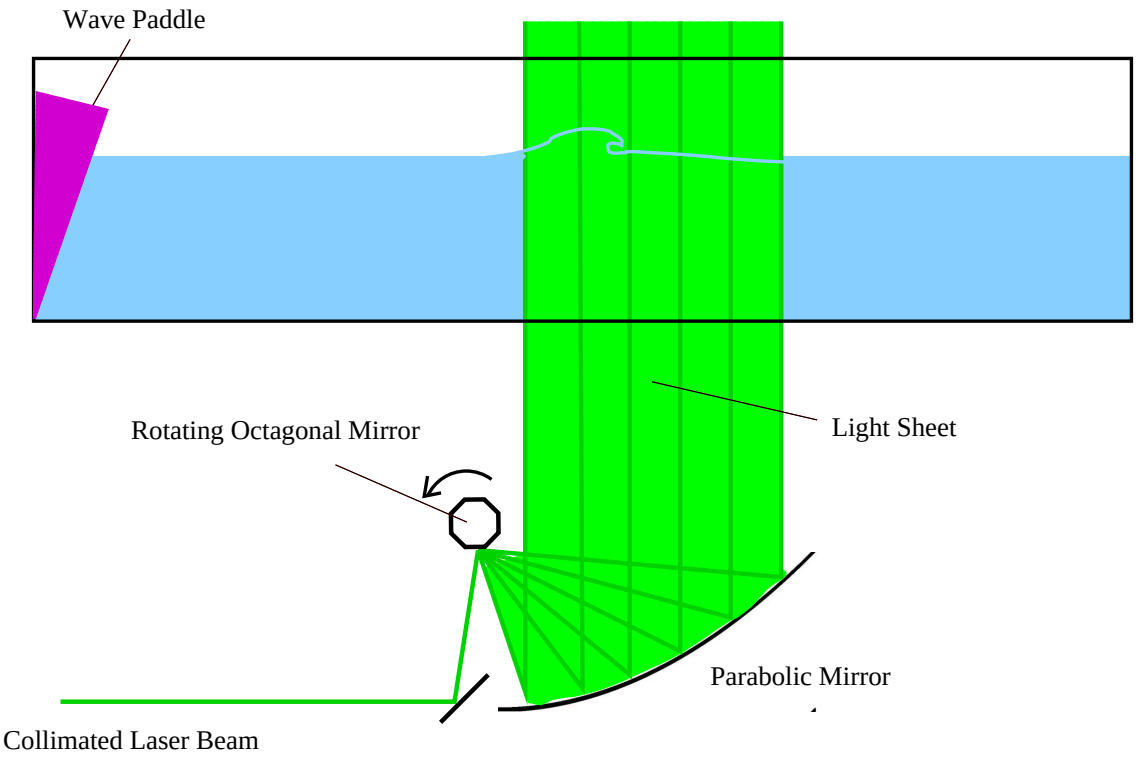

Figure 2.3: Scanning Beam Box

of curvature in the Edinburgh Scanning Beam Boxes; one has $L = 1m$ and the other has $L = 0.5m$. The value of L determines the width of the lightsheet, while its thickness is determined by the collimating lenses.

2.4 Digital Cameras

Digital cameras were used in these experiments to record the flow illuminated by the lightsheet. These offer the advantage over wet-film photography that the image data can be transferred directly to a computer for immediate inspection, without the delay inherent in the chemical development of film.

All digital cameras consist of an array of *Charge Coupled Devices*, CCDs, each of which converts photons into electrical signals via the photoelectric effect. Essentially, a CCD consists of a semiconducting material bordered by a conductor. A small voltage is applied across the semiconductor creating a potential well within it. When a photon of the appropriate frequency enters the semiconductor, an electron-hole pair is formed. The hole is absorbed in the p-layer of the semiconductor, while the electron moves towards the potential well, where it is stored. Electrons accumulate within the well throughout the duration of the exposure; the amount of charge is proportional to the total light received. This CCD is also called a *pixel*; digital cameras generally consist of an array of thousands or millions of these pixels.

In order to generate an image, the charge built up in each pixel must be measured, and the way in which this is done is the main distinction between the different types of digital camera. Each photosensitive area is coupled to a Charge Transfer Device, or CTD, which is responsible for shifting the charge accumulated in each CCD to a common output without interference between the individual charge packets. These charge packets are then passed through a charge-to-voltage converter, which outputs a voltage proportional to the charge and thus the amount of incident light arriving at the CCD.

The CCD sensor read-out can either be sequential (progressive scan) or interlaced, where all the odd rows are read before the even rows. Either way, the time

taken for the entire array to be read out depends on the number of pixels, and a new exposure cannot occur until all pixels have been read. Thus the frame rate of a camera is inversely proportional to the pixel resolution. This means that there is a compromise between the spatial and temporal resolution of the flow.

2.4.1 Camera Noise

Like all electronic devices, a CCD camera is affected by noise. The main contribution to this noise is thermal, from the creation of electron-hole pairs indistinguishable from those caused by the photo-electric process. Thermal noise, also known as dark current, is constant for a given temperature and exposure, and can therefore be compensated for by subtracting a fixed bias voltage from the camera output. Nevertheless, the generation of thermal electron-hole events is random, resulting in dark current noise, roughly proportional to the square root of the dark current. Thermal noise reduces by 50% for every $6 - 7^oC$ decrease in temperature, which is why many newer CCD arrays are cooled [36].

Another source of camera noise is the clock frequency, which determines how fast the pixel data is output by the camera. For this reason, the clock frequency of most CCD cameras is limited to a maximum of $20MHz$ [37].

2.4.2 Camera Specifics

The cameras used in these experiments are Pulnix TM9701. The main properties of the TM9701 are listed in table 2.1.

Array Size	768 (H) x 484 (V)
Pixel Size	11.6μm (H) x 13.3μm(V)
Frame Rate	$30fs^{-1}$
Array Type	Full Frame Interline Transfer
Fill Factor	60%
Triggering	Asynchronous Reset

Table 2.1: Specifications of Pulnix TM-9701 camera

Full Frame Interline Transfer (FFIT) means that each pixel in the CCD array has its own area for storing charge. The charge produced in the CCD during the exposure is transfered to its storage area in less than $1\mu s$. This charge is then shifted vertically downwards into a masked-off shift register at the base of the array, and clocked through a charge-to-voltage converter. Because this transfer is rapid, FFIT cameras tend to have relatively high frame rates. An important property of such cameras is that each pixel is exposed at the same time, which is essential for accurate flow records.

Since each pixel consists of both a photosensitive area and a storage site, not all of the light reaching the pixel is stored. The *fill-factor* is the percentage of each pixel which is sensitive to light. For the Pulnix TM-9701, the fill factor is only 20%, though this can be increased to 60% by placing a microlens in front of

each pixel.

The cameras are asynchronously resettable, so the exposure can be controlled by an external trigger pulse. They have undergone factory modification 29-5 which means that the exposure is triggered by a negative TTL pulse: the exposure begins on the falling edge and lasts for the width of the pulse.

The TM9701 is an 8-bit camera, thus capable of distinguishing 256 grey levels. Each second, the camera outputs 8*30 bits per pixel, or approximately 8.9×10^7 bits in total. Dedicated hardware is required to handle such a quantity of data.

2.4.3 Frame Grabber

The Coreco Viper Quad is a single-slot frame grabber for the PCI bus, capable of acquiring the data output from four separate, non-synchronised cameras. It has four independent channels, each of which comprises an analogue-to-digital converter (ADC) and synchronisation circuitry. The analogue data output from the camera passes through the ADC and is stored in a buffer in system memory. In addition to acquiring image data, each channel can also send power and trigger signals to the camera, all via a single, 12 pin Hirose cable.

Associated with the Viper Quad hardware is Sapera, a high-level library of C-callable functions required for controlling the operation of the framegrabber. Tim Dewhirst has incorporated Sapera into a graphical user-interface software

package capable of grabbing and displaying images, setting trigger options and saving image data to the hard disk of the host computer.

The maximum number of images in a single sequence is limited by computer RAM. A Gigabyte of RAM was purchased for the host, allowing over 2000 images to be stored in each experimental run.

Chapter 3

Laser Induced Fluorescence

3.1 Introduction to LIF

Laser Induced Fluorescence (LIF) is a full field, non-intrusive, optical technique for obtaining concentration measurements of a material within a fluid.

Fluorescence is a quantum mechanical interaction between electromagnetic radiation and electrons. A photon of frequency ν colliding with an atom will either be absorbed or scattered. The probability of absorption is greatest when the energy of this photon, $h\nu$ (where h is Planck's constant), matches one of the atom's excitation energies. If the photon is absorbed, its energy is transferred to one of the atom's electrons. The atom is now excited and therefore unstable. If the atom is relatively isolated, as in a low-pressure gas, this additional energy is

dissipated by the emission of another photon of the same frequency in a random direction. This is the origin of the dark, Fraunhofer absorption lines in a stellar spectrum. In denser gases, liquids and solids, however, the energy is dissipated by intermolecular collisions, resulting in the emission of a band of photon frequencies. If these photons have frequencies within the visible spectrum, the material will appear to glow. If this energy decay occurs rapidly (within around $10^{-7}s$), the process is termed *fluorescence*; otherwise, the transition is called *phosphorescence* [38].

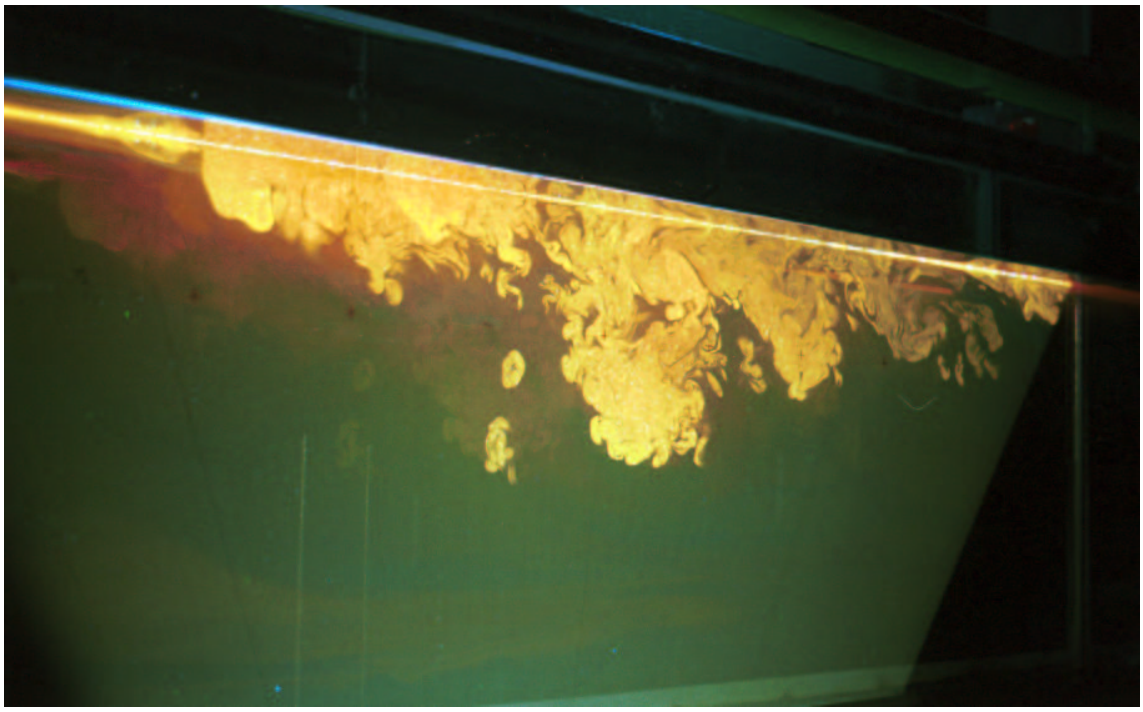

Figure 3.1: Laser Induced Fluorescence (photograph by Alistair Arnott)

Rhodamine B was used in the experiments described in this thesis. Chemical formula $C_{28}H_{31}N_2O_3Cl$, Rhodamine B is an organic dye which contains an ex-

tended chain of conjugated bonds (alternating single and double carbon bonds) and is therefore highly fluorescent [39]: concentrations of the order of parts per billion can be seen with the human eye. Rhodamine B is soluble in water, producing a pink solution but when illuminated, it glows a bright orange colour (figure 3.1).

The purpose of these experiments is to gain understanding in the dispersion of surface contaminants, in particular petroleum products. However, for reasons of cleanliness and safety, oil was not considered suitable for use as the surface film. The following properties for a solvent for the rhodamine were required: inexpensive, readily available, soluble in water and buoyant. Methanol was chosen since it fulfilled all of these criteria, and has been previously used in LIF experiments with rhodamine [40].

During preliminary experiments, it was noted that the mixing region is considerably wider than $1m$, even after a weak breaking event. For this reason, the Scanning Beam Box described in section 2.3 was modified. Instead of reflecting the beam onto a parabolic mirror, the rotating mirror was positioned to reflect the beam upwards such that it sweeps though a 90^o arc eight times per revolution (figure 3.2). The rotational frequency is sufficiently high that, as before, the beam produces an apparently steady fan of light.

With this Scanning Beam Box, a larger section of the tank is illuminated: the

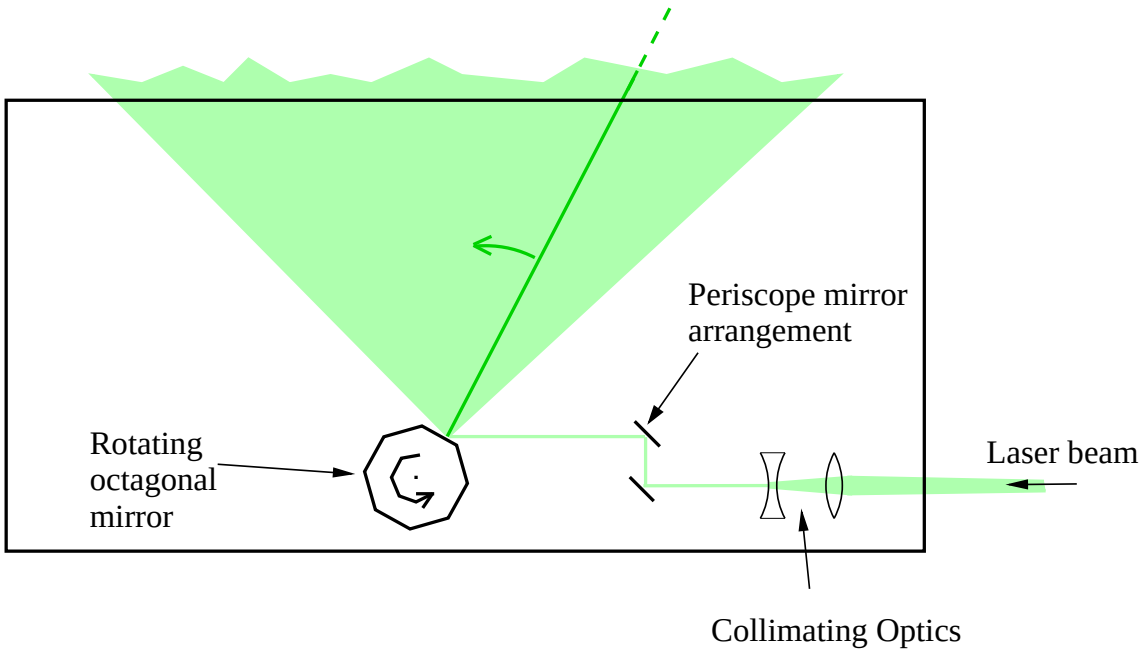

Figure 3.2: Modified Scanning Beam Box

lightsheet sweeps through just over $2m$ of the water surface; see figure 3.3[1].

The water depth in the tank is $0.75m$ and the wave heights are not more than $0.11m$. The region of interest illuminated in the tank is therefore approximately $2m$ by $0.8m$, a width-to-height ratio of 2.5.

3.1.1 Camera Arrangement

Using the information about the TM9701 pixel dimensions in table 2.1, it can be seen that the width-to-height ratio of the Pulnix images is 1.35.

[1]Based on diagram by Arnott [41]

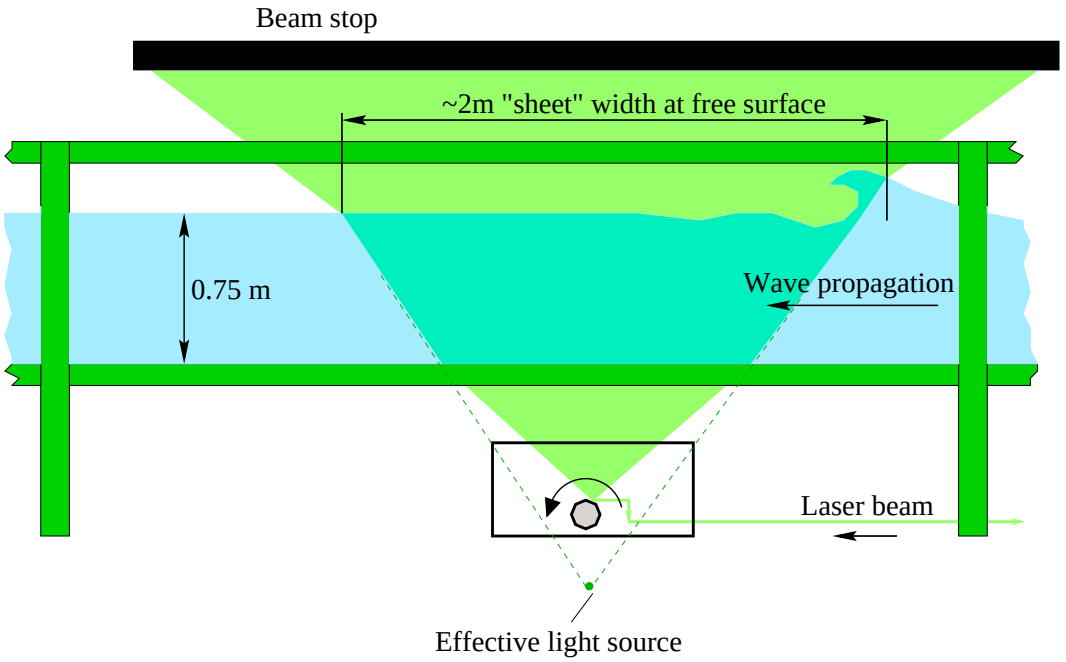

Figure 3.3: Side View of Wave Tank

After comparing the width-to-height ratios of both the Pulnix camera and the diverging lightsheet, it was decided to image the scene with two cameras positioned side by side, as shown in figure 3.4[2]. Due to space restrictions in the lab, it was not possible to position the cameras more than $3m$ from the wall of the tank, placing an upper limit on the distance between the object and image planes. This distance, and the focal length of the imaging lens, determine the magnification of the optical system (equation A.3 in Appendix A). The magnification required is determined by dividing the size of the array by the size of the area to be imaged, and is approximately 0.01. Using these restrictions, it was decided to use a $28mm$ focal length lens for each camera. The cameras were separated by $1m$, arranged

[2]Based on Diagram by Arnott [41]

to overlap by a few pixels to allow the images from each to be combined into a single, wide image.

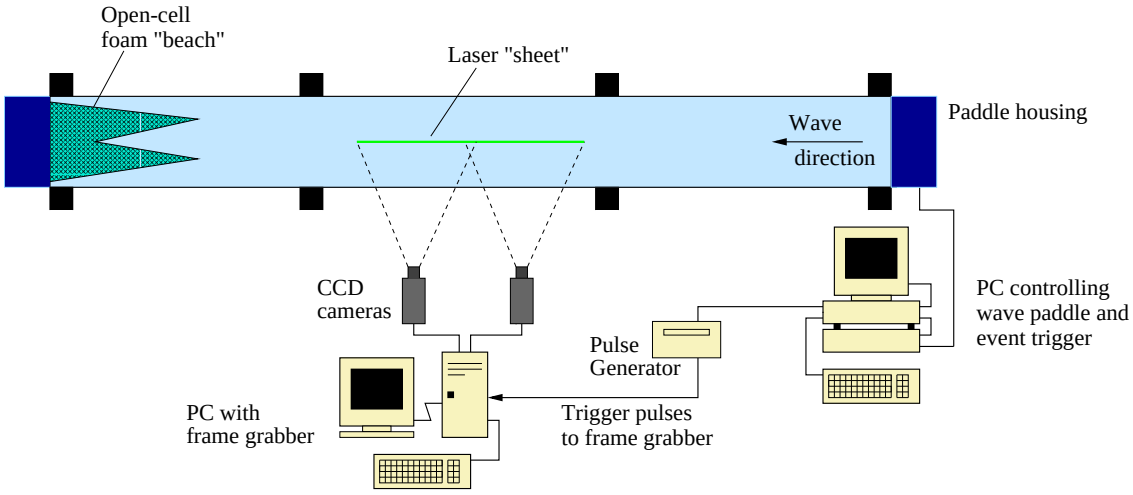

Figure 3.4: Plan of LIF Apparatus

Laser safety goggles are placed in front of each camera lens; these goggles remove the Argon-ion laser light, leaving only the fluorescence.

The cameras were triggered simultaneously by a burst of pulses from a signal generator. This burst of pulses was started by a relay switch in the wavemaker interface box.

3.2 Application of the Surface Film

In order to investigate the factors affecting its dispersion, the film should be as uniform as possible. Ideally, the film would lie entirely on the surface of the

water and have constant thickness. In addition, the application of the film should be repeatable so the initial concentration distribution is not a variable.

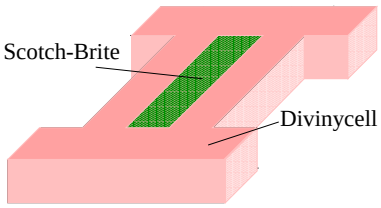

Figure 3.5: Film Applicator

Initially, a syringe was used to apply the contaminant to the surface. Although this produced a film of known volume, it proved difficult to prevent the fluid from breaking the surface and diffusing downwards. A better quality film was obtained by applying the rhodamine solution to a saturated sponge floating on the surface, and gently pouring water onto the sponge to expel the rhodamine. However, the high absorbency of the sponge meant that there was a large uncertainty in the quantity of rhodamine escaping to form the film.

The method of application that was finally adopted involved the float shown in figure 3.5. The float consists of an 'I' shaped section of divinycell, a lightweight, high strength foam material, with a central strip removed. This gap contains Scotch-Brite, a brand of cleaning wool. The Scotch-Brite is soaked in water until saturated, and then the rhodamine solution is added. A flow of water on to the Scotch-Brite flushes out the rhodamine solution and spreads it over the surface; see figure 3.6[3]. Care must be taken when removing the floats to avoid drips which disturb the film.

[3]Diagram by Alistair Arnott

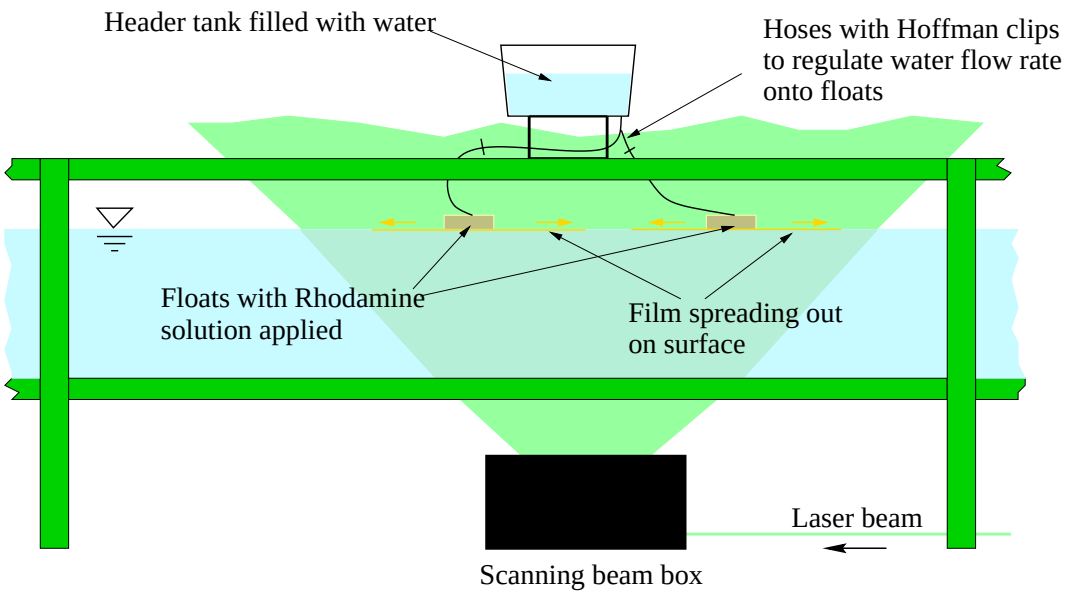

Figure 3.6: Application of Surface Film

In most of the experiments undertaken, the film volume was $5ml$. This was found by trial and error to be the smallest quantity that did not produce a patchy film. The $5ml$ was divided equally between two floats, positioned approximately $1m$ apart. This resulted in a film approximately $3m$ long with a mean thickness of the order of several microns.

The surface of the water was skimmed prior to the application of the rhodamine to remove dust and other particles that would interfere with the spreading of the film.

3.3 Preparation of LIF images

On completion of the experiment, the image data in system memory is written to the hard disk. Before information from the images can be extracted, each image must be processed in two ways, which will be described in the following subsections.

3.3.1 Correction for Lightsheet Variation

The test section of the tank observed by the cameras is not uniformly illuminated. The lightsheet is effectively a 90^0 sector of a thin disk whose centre is below the actual point of contact with the mirror due to refraction at the base of the tank. The light intensity decreases as $\frac{1}{r}$ where r is the distance from the effective source, so at the water surface, the middle of the lightsheet is brighter than the edge. In addition to this $\frac{1}{r}$ fall-off, the lightsheet is attenuated due to reflection off the tank bottom and absorption by the water. The same concentration of rhodamine will therefore produce a different brightness in the raw LIF images, depending on its position.

The variation in lightsheet intensity is compensated for as follows: once the experimental run is complete, the rhodamine present in the tank is thoroughly mixed until its concentration throughout the tank is approximately uniform. An image of the lightsheet is then taken. Since the concentration is constant, any

variation in the brightness of the image is due to the lightsheet rather than the rhodamine concentration. The grey level of each pixel in the raw images, GL_{raw} can then be divided by the corresponding pixel in this background image, GL_{back}, and multiplied by an appropriate scale factor S, chosen so the final image is neither too dark nor too bright:

$$GL_{corrected} = \frac{GL_{raw}}{GL_{back}} \times S \tag{3.1}$$

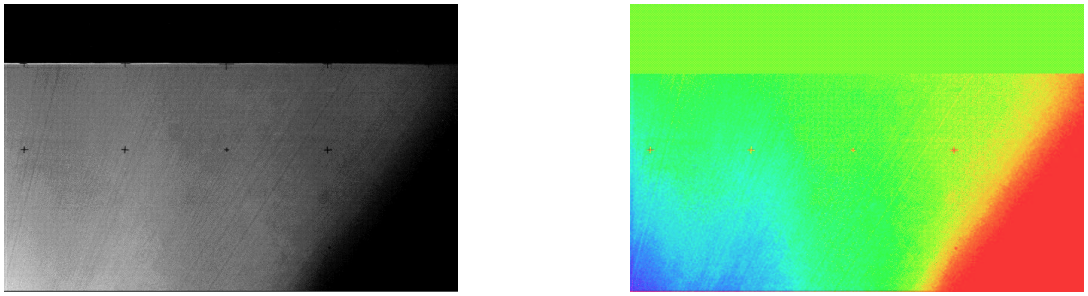

(a) (b)

Figure 3.7: Compensation for Lightsheet variation

In practice, several background images are taken and averaged, to minimise any remaining concentration gradients. Figure 3.7 (a) is the average of four background images. For the reasons mentioned above, the lightsheet is brighter near the bottom and middle of the tank. The MWL in the image is artificially bright due to reflection of the laser beam off the surface. Also, the brightness above the surface is zero since there is no rhodamine present there. Thus the image as it stands cannot correct for lightsheet variations near the MWL or in

the crests of waves. A least squares quadratic curve is fitted to the mean pixel variation below the surface and extrapolated to the top of the image. The original pixel values at and above the surface can then be replaced by these extrapolated values. This is a rather crude solution, but it was not possible to fill the tank until the MWL was above the field-of-view of the camera, and the replacement only really affects crests of waves which reduce in amplitude soon after breaking. A false coloured version of this extrapolated background image is shown in figure 3.7 (b), with red corresponding to low brightness and blue to high brightness. This correction implicitly assumes that the brightness of the fluorescence (as recorded by the camera) is proportional to the the concentration of the rhodamine. This relationship will be discussed further in the following section.

Once the raw images have been corrected in this way, the brightness of the processed image is related to the concentration of the rhodamine alone.

3.3.2 Calibration of LIF Images

In order to relate the pixel brightness to an actual concentration, an image of a calibration vessel is taken. This vessel is made of perspex, sealed with silicon and contains 12 compartments containing different, but known, concentrations of the rhodamine/methanol stock solution in water (see figure 3.8).

The image of the vessel must first be corrected for lightsheet variation as

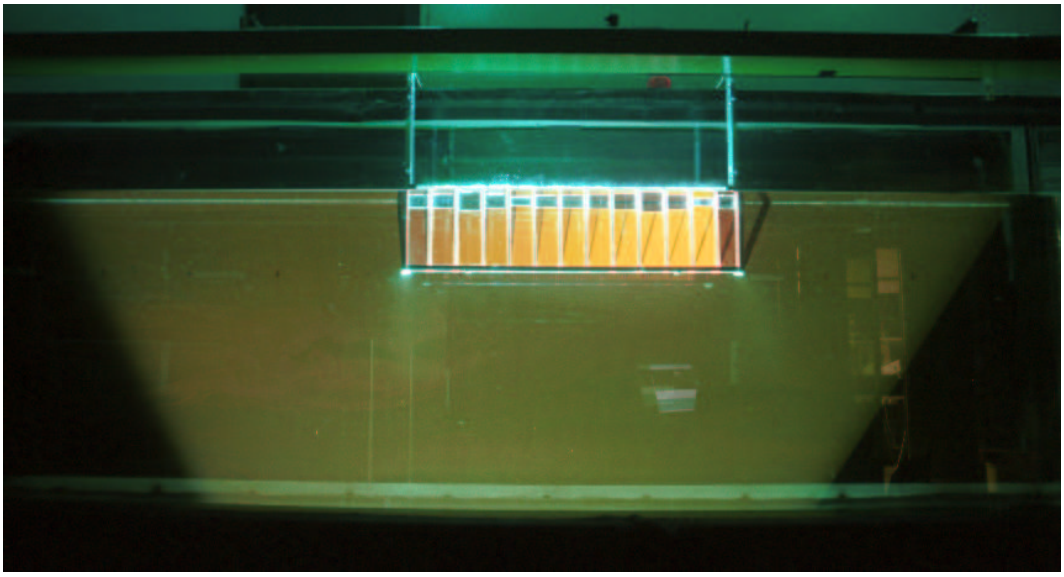

Figure 3.8: Calibration Vessel (photograph by Alistair Arnott)

described above; indeed the scale factor S required for equation 3.1 is chosen by trial and error such that the grey level of the compartment containing the highest concentration of rhodamine is near the upper limit of grey level values (255) while the grey level of the lowest concentration is just above zero. The same value for the scale factor is subsequently used in the dispersion images.

The mean pixel value of each compartment of the calibration vessel is recorded. A graph of pixel value against concentration is shown in figure 3.9.

The graph is nearly a straight line through the origin, suggesting that in this range of concentrations, the pixel brightness is directly proportional to the rhodamine concentration. It was found that rhodamine solutions of significantly higher concentration fluoresced *less* brightly, due to attenuation of the laser beam.

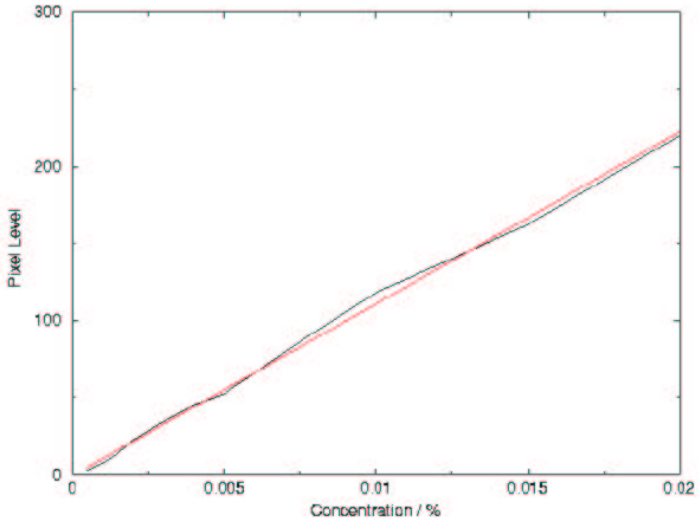

Figure 3.9: Graph of Pixel Level vs Concentration

The maximum concentration in the vessel is 0.02% of the stock solution used for the film, equivalent to $0.02g$ of rhodamine per litre.

The concentration at a particular pixel in the LIF image is determined by comparing its grey level, $GL_{corrected}$, with the mean grey levels of the various concentrations of rhodamine in the calibration image, according to table 3.1.

Once the concentration at a particular pixel has been determined, it is assigned the corresponding grey level in the third column. These values are approximately equally spaced between 0 and 255. By assigning them fixed values, the same concentration of rhodamine will result in the same pixel value in both images. In addition, the even spacing maximises the contrast between each of

Pixel Condition	Concentration / %	Grey Level
$GL_{corrected} < GL_{0.0005\%}$	0	0
$GL_{0.0005\%} \leq GL_{corrected} < GL_{0.001\%}$	0.0005	21
$GL_{0.001\%} \leq GL_{corrected} < GL_{0.0015\%}$	0.001	42
$GL_{0.0015\%} \leq GL_{corrected} < GL_{0.002\%}$	0.0015	63
$GL_{0.002\%} \leq GL_{corrected} < GL_{0.003\%}$	0.002	85
$GL_{0.003\%} \leq GL_{corrected} < GL_{0.004\%}$	0.003	106
$GL_{0.004\%} \leq GL_{corrected} < GL_{0.005\%}$	0.004	127
$GL_{0.005\%} \leq GL_{corrected} < GL_{0.0075\%}$	0.005	148
$GL_{0.0075\%} \leq GL_{corrected} < GL_{0.01\%}$	0.075	170
$GL_{0.01\%} \leq GL_{corrected} < GL_{0.0125\%}$	0.01	191
$GL_{0.0125\%} \leq GL_{corrected} < GL_{0.015\%}$	0.0125	212
$GL_{0.015\%} \leq GL_{corrected} < GL_{0.02\%}$	0.015	233
$GL_{0.02\%} \leq GL_{corrected}$	0.02	255

Table 3.1: LIF Concentration Mappings

the concentration bands, which is useful for visual inspection.

3.3.3 Combining the Images

Once every image captured from both cameras has been corrected for light-sheet variation and calibrated, the images can be combined.

The cameras were carefully arranged such that there was a small horizontal overlap between their fields of view. By inspecting the corresponding image from both cameras, this misalignment can be ascertained and used by a program to combine the images. The heights of the cameras were adjusted such that the MWL was at the same position for both. In most of these experiments, the overlap was approximately 8 pixels, resulting in a combined image size of (768+768-8) by 484.

The top corner of each page in this thesis contains a miniature version of such a combined image. The join between the two original images is generally smooth unless waves are passing. Then, the water height appears to contain a discontinuity at the join, due to refraction at the moving water surface. This is not considered to be a problem since this study is more concerned with long term dispersion.

3.4 Summary

In this chapter, the technique of Laser Induced Fluorescence has been reviewed, and a method for applying LIF to measure the dispersion of a surface film has been described.

Chapter 4

Particle Image Velocimetry

4.1 Overview

Like LIF, Particle Image Velocimetry (PIV) is a non-intrusive, full field optical measuring technique. PIV is used to obtain velocity information about fluid motion and has been applied to a diverse range of flows including water dynamics, aerodynamics, air-conditioning systems, acoustics, blood circulation and boundary layer turbulence.

In PIV experiments, the fluid of interest is seeded with tracer particles which are illuminated by a sheet of bright light. The positions of these particles at different times are recorded on a camera. Then, by measuring the particle displacements, the motion of the fluid can be ascertained.

4.2 Tracer Particles

Tracer particles may be naturally occuring impurities or, more commonly, are added to the fluid prior to the experiment. The velocity of the fluid is assumed to determine the motion of these particles; therefore it is important that the particles faithfully follow the fluid.

4.2.1 Fluid Properties of Tracer Particles

Any discrepancy between the density of the tracer particle, ρ_p, and the density of the fluid, ρ, results in both gravitational and inertial drag velocities. The gravitationally induced velocity, U_g, is caused by a difference between the gravitational and buoyancy forces, and for a spherical particle of diameter d_p is given by [36]

$$U_g = d_p^2 \frac{(\rho_p - \rho)}{18\mu} g \tag{4.1}$$

where g is the gravitational acceleration and μ is the fluid viscosity. Similarly, the particle velocity will lag behind the velocity of an accelerating fluid due to its inertia; the magnitude of this velocity lag is identical to equation 4.1, but with g replaced by a, the fluid acceleration.

These velocities increase as the square of the particle diameter, implying that

small particles will follow the flow more accurately than larger particles. A further constraint on particle size is that d_p should be small in comparison to structures present in the flow, so that the fluid velocity does not change significantly across the tracer particle.

4.2.2 Light Scattering by Tracer Particles

These considerations suggest that the ideal tracer particle would have a small diameter. However, the tracer particles must also scatter sufficient light to be detected. Mie's scattering theory, which applies to particles with diameters larger than the wavelength of light, states that the average intensity of the light scattered by a particle is roughly proportional to the square of its diameter [42].

In practice, there is a compromise between these two size requirements. In experiments involving water, conifer pollen, with a diameter of around $70\mu m$ and a density slightly less than that of water, is often used.

4.2.3 Concentration of Tracer Particles

PIV is just one of several techniques which use tracer particles to make the flow visible.

If the density of the tracer particles is low, the average particle separation is considerably larger than the mean displacement between images. Thus individual

particles can be tracked, and the displacement of a particular particle reveals the local velocity in the fluid. However, because of the low density, velocity information can only be obtained where a particle happens to be present. Thus there may be regions of the flow where the local velocity can not be measured. This method of analysing flow motion is called *Particle Tracking Velocimetry* (PTV).

At the other extreme, the tracer particle density is high, and individual particles tend to overlap. An image of the flow will then be speckled. Since it is impossible to identify individual particles, the motion between images is obtained by a statistical analysis. This approach reveals the most likely displacement of a group of particles, and the technique is referred to as *Laser Speckle Velocimetry* (LSV). The problem with LSV is that the high density of particles tends to affect the fluid motion, for example by introducing two-phase flow effects.

In PIV, the seeding density is between these two regimes. There are still too many particles to track them individually, so a statistical approach is required, as in LSV. But the density is not so high that the particles have a significant effect on the fluid flow.

4.2.4 Imaging Tracer Particles

The image size of a tracer particle depends on the particle's diameter, d_p, and the point spread function of the imaging lens (neglecting lens aberrations). The point spread function of a lens describes the irradiance of an image when the object is a point source. If the lens has no aberrations, the intensity distribution of the object is described by the Airy function, which mathematically is the square of the first order Bessel function. The first zero of the Bessel function results in a dark ring in the image plane; the light within this ring produces the *Airy disk*, which is the smallest particle image that can be obtained for a given lens system. The diameter of the Airy disk, d_{Airy} is given by:

$$d_{Airy} = 2.44 f_{\#}(M+1)\lambda \tag{4.2}$$

where $f_{\#}$ is the ratio of the focal length of the lens to its aperture diameter (the f number), M is the magnification factor of the lens and λ is the wavelength of the light. For a typical lens system, the diffraction-limited image diameter is of the order of several microns.

The Airy function, which describes diffraction-limited imaging, can be closely approximated by a Gaussian function. In the analysis of PIV images, the assumption that the intensity distribution of the particle images are Gaussian is often used as it simplifies the mathematics. However, equation 4.2 only applies to

small particles at low magnifications. For larger particles and/or magnifications, the image diameter, d_{image}, can be approximated as:

$$d_{image} = \sqrt{(Md_p)^2 + d_{Airy}^2} \tag{4.3}$$

where d_p is the diameter of the particle being imaged. This equation neglects factors such as further scattering of the scattered light, out-of-focus effects and lens aberrations. In practice, the actual diameter of the image of a particle can be an order of magnitude larger than this theoretical value [14]. The size of the particle image affects the quality of the PIV analysis, as will be seen in section 4.7.

4.3 Illumination

In order to locate a tracer particle accurately, the duration of the illumination must be short enough that the particle does not move significantly and hence streak the image. In addition, the particle must scatter enough light to be visible; thus a large amount of light must be available in a short time. The laser is ideal for this purpose. The type of laser required depends on the speed of the fluid. For air flows, where the speed can range from a few metres per second to supersonic, a pulsed laser is typically required. For the experiments described in this thesis, involving breaking water waves, the speeds involved rarely exceed $1ms^{-1}$, and a

continuous wave laser is adequate. The Scanning Beam box described in section 2.3 was used, because it can provide around 20 times the exposure energy of a lightsheet produced by refraction through a diverging lens [35].

4.4 Camera Exposure

There are two main methods of recording the positions of the tracer particles in PIV experiments: (1) two or more exposures of the particles on a single frame (*single frame/multi-exposure*) and (2) two or more exposures of the particles, each on separate frames (*multi-frame/single exposure*). The main difference between these two approaches is that the first is inherently directionally ambiguous, since it is not possible to determine which images correspond to which exposure.

Early PIV used wet-film photography to image the tracer particles. Due to the difficulty of winding the film on between exposures, the single frame/multi-exposure was most commonly used. The main drawback of wet-film PIV is that obtaining the velocity measurements involved developing the film and analysing the negatives, a process which takes several hours [43]. Since a single experiment may involve hundreds of images, a complete analysis was very time consuming.

The increasing popularity of PIV is, to a large extend, due to recent advances in computer and CCD digital camera technology. The bottleneck inherent in wet-film PIV was removed as digital images could be downloaded to a computer,

and the analysis automated. Another advantage of digital PIV was that it became practical to obtain separate frames for each exposure, thereby removing the directional ambiguity.

It should be noted that the spatial resolution of CCD arrays is at least two orders of magnitude lower than photographic film. This is not a serious drawback, however, since the purpose of a PIV image is *not* to recreate the scene as precisely as possible, but rather to provide sufficient samples of the flow such that a statistical analysis can be applied. Westerweel showed that the minimum required sampling rate for PIV images is 3-4 times less than the optical bandwidth [43]. Therefore, the lower resolution of the CCD array does not adversely affect the PIV analysis.

The analysis of single frame/multi-exposure and multi-frame/single exposure PIV images is described in the following section.

4.5 Correlation

In multi-frame/single exposure PIV, two images revealing the positions of tracer particles within a fluid are taken a short time, Δt, apart. As mentioned in section 4.2, it is not possible to track individual particles, so a statistical analysis is required. Each image is divided into a grid of small sections known as *interrogation areas*. The corresponding interrogation areas within each of the

two images are then *cross-correlated*. The cross-correlation function is effectively a pattern-matching routine which determines which displacement to shift the first area to best overlap the second area. By scaling this displacement by the magnification of the camera lens and dividing by Δt, an average velocity for the fluid within the interrogation area can be obtained. This process is repeated at each grid point within the image, resulting in a map of velocity vectors to describe the flow.

The definition of the cross-correlation function, $R_{fg}(i,j)$, is:

$$R_{fg}(i,j) = f(i,j) \otimes g(i,j) = \int_{-\infty}^{\infty} \int_{-\infty}^{\infty} f(\alpha,\beta) g^*(\alpha - i, \beta - j) d\alpha d\beta \qquad (4.4)$$

The digitally recorded interrogation areas are discrete rather than continuous, and have a finite size. Thus equation 4.4 becomes:

$$R_{fg}(i,j) = \sum_{x=0}^{M} \sum_{y=0}^{N} f(i,j) g(x - i, y - j) \qquad (4.5)$$

where M and N are the dimensions of the interrogation area, and $f(i,j)$ and $g(i,j)$ are functions representing the pixel values of the two images.

The cross-correlation function is frequently normalised to remove effects such variations in the light sheet brightness, and the number and size of the tracer images:

$$R_{fg}(i,j) = \frac{\sum_{x=0}^{M}\sum_{y=0}^{N}\Big[f(x,y)-\bar{f}\Big]\Big[g(x-i,y-j)-\bar{g}\Big]}{\sigma_f \sigma_g} \tag{4.6}$$

where $\bar{f}$ and $\bar{g}$ are the average values of the functions f and g respectively, and σ_f and σ_g are their standard deviations. $R_{fg}(i,j)$ then varies between -1 and 1, and its average value across the interrogation area is 0.

The cross-correlation function can be considered to consist of two parts:

1. Correlation between images of particles in the first interrogation area with images of the *same* particles in the second area (particle pairs), and

2. Correlation between images of particles in the first interrogation area with images of *different* particles in the second area (i.e. random correlations).

The random correlations contribute towards noisy peaks in the correlation plane. If, however, the displacement of each of the particles between images is constant, the correlations between each of the particle-pairs combine to produce a prominent peak, significantly higher than the noise peaks. The location of this peak relative to the centre of the plane then corresponds to the constant displacement, while the height of the peak depends on the number of particle pairs. The signal-to-noise (S/N) ratio is defined as the height of the highest peak to the mean peak height, and is a measure of the quality of the correlation. For the S/N ratio to be large, a number of conditions must be met:

- Time separation of images: Δt should be long enough to resolve the displacement of the particles to sufficient accuracy, yet short enough that the particles do not move outwith the light sheet.

- The size of the interrogation area must be sufficiently small that the velocity gradient across it can be neglected, but large enough that there are sufficient particle pairs to contribute to the correlation.

- The seeding of the tracer particles should be homogeneous, so that a statistical analysis can be applied.

- The out-of-plane motion should be small, again so that there are enough particles common to the interrogation area of each image.

Figure 4.1 contains two synthetic interrogation areas of tracer particles, and the correlation plane obtained by cross-correlating them.

The correlation plane consists of a series of peaks, one of which is significantly higher than the others. The location of this principal peak is below right of centre, implying that the average particle displacement in sample 1 is down and to the right. This can be seen to be the case. Dividing this displacement by the time separation between the images yields the mean velocity within the interrogation area.

By averaging the particle displacements within the interrogation areas, the cross-correlation function effectively low-pass filters the fluid motion: the larger

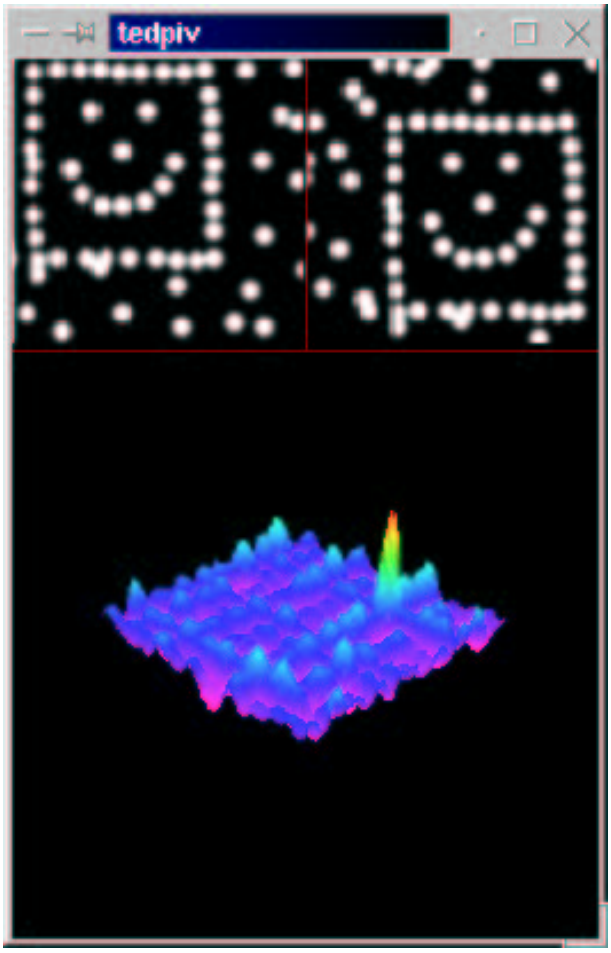

Figure 4.1: Interrogation Areas and Correlation Plane

the interrogation area, the more smoothing takes place. Thus the size of the interrogation area limits the spatial resolution of the flow that can be measured. Nyquist's Sampling theorem states that the highest frequency that can be detected is half the sampling frequency. An interrogation area whose side has length N has a spatial frequency of $\frac{1}{N}$. In order to measure this frequency correctly, the sampling frequency should be twice this frequency, or $\frac{2}{N}$. This corresponds to a grid point spacing of $\frac{N}{2}$. Therefore, to represent a flow with spatial frequencies

of up to $\frac{1}{N}$, the velocity vectors should be a distance $\frac{N}{2}$ apart. The interrogation areas then overlap by 50%. Increasing the grid spacing (thereby reducing the number of velocity vectors) reduces the spatial resolution of the representation; decreasing the spacing results in over-sampling, so despite the extra velocity vectors, there is no additional velocity data because these extra vectors are not statistically independent.

The size of the interrogation area, like the size of the tracer particles, is a compromise. Too small, and there will be insufficient particles to obtain a good correlation; too large, and velocity gradients across the area and a loss of spatial resolution due to low-pass filtering become problematic.

If the criteria required for a high S/N ratio are not fulfilled, the principal peak in the correlation plane may not represent the mean displacement within the interrogation area. If this occurs, the velocity vector obtained from this peak will not accurately describe the local fluid velocity. Such a vector is termed an *outlier*. The presence of outliers is undesirable but inevitable, and detecting them is in important part of PIV post-processing. Appendix B is devoted to this topic.

The advantage of measuring fluid motion by recording two single exposures of the tracer particles rather than taking a single, double exposure can be seen by considering the analysis of the double exposed image. Instead of cross-correlating two distinct images, the double exposure is correlated with itself. This process is called *auto-correlation*. The auto-correlation plane consists of a large, central

peak corresponding to the perfect correlation of an image superimposed upon itself. Located symmetrically about this central peak are two smaller peaks representing the mean displacement within the interrogation area. There are two peaks because of the directional ambiguity in the image: it is not possible to determine which particle images were recorded in the first exposure, and which correspond to the second exposure. A synthetic interrogation area and its auto-correlation function are shown in figure 4.2.

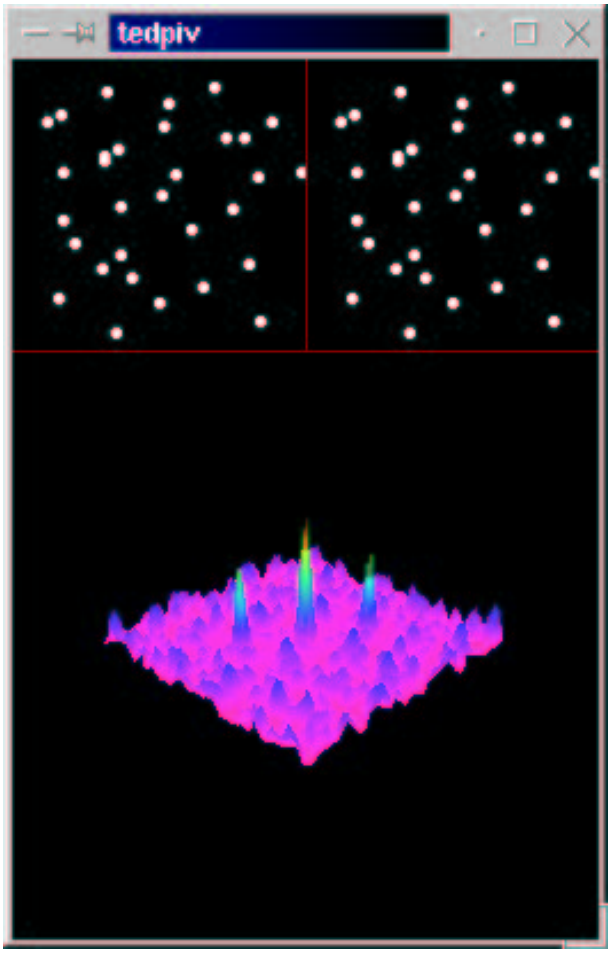

Figure 4.2: Double Exposure and its Auto-Correlation Function

Distinguishing the displacement peaks becomes more difficult as the displacements approach zero. If the particle pairs overlap in the image, the displacement peaks merge with the the central correlation peak, making an accurate velocity measurement difficult. Indeed, if the local velocity is zero, the correlation plane will consist solely of a central peak and random noise. An outlier will then certainly occur.

A further problem is distinguishing which of the two displacement peaks corresponds to the flow. If the flow is predominantly in one direction, the appropriate displacement peak can be identified; however for any flow which reverses direction, the relevant peak is unknown. It is possible to remove this directional ambiguity by *image shifting* which involves moving the image relative to the camera between exposures, effectively superimposing a mean flow onto the motion [44]. This, however, introduces further experimental difficulties, and can introduce distortions into the PIV images.

The inability of auto-correlation to resolve small displacements reduces the dynamic range of the velocity measurements possible. The directional ambiguity and increased likelihood of outliers at low velocities are drawbacks which can be avoided by using a separate image for each exposure and cross-correlating.

4.6 Fourier Space

According to equation 4.5, every point in the correlation plane requires $M \times N$ multiplications and $M \times N$ additions. There are $M \times N$ such points in each interrogation area, so to obtain the entire correlation function, and thus a single velocity vector, requires at least $2M^2N^2$ calculations. Repeating this process to obtain a set of vectors is therefore computationally very expensive.

The Wiener-Khintchine theorem states that a correlation in real space is equivalent to a multiplication in Fourier space. Mathematically,

$$R(i,j) = f(i,j) \otimes g(i,j) \Longleftrightarrow FT(R(i,j)) = F(u,v).G^*(u,v) \qquad (4.7)$$

where $F(u,v)$ and $G(u,v)$ are the Fourier Transforms (FTs) of $f(i,j)$ and $g(i,j)$ respectively and $*$ denotes the complex conjugate.

To obtain the correlation in Fourier space, therefore, each of the interrogation areas is Fourier Transformed. These Fourier Transforms are then multiplied together, and the product is inverse Fourier Transformed to produce the cross-correlation plane.

Evaluating the correlation plane in this way sounds more complicated, yet by using the fast Fourier Transform, this method is significantly more efficient. Each FFT involves $N^2 log_2 N$ calculations, where $N \times N$ is the size of the inter-

rogation area. The efficiency can be further increased since the real part of the Fourier Transform is symmetric, while the imaginary part is anti-symmetric. One restriction of the FFT is that the size of the input data (i.e. the interrogation area) must be a power of two. This is not really a problem, but there are further properties of the FFT which can affect the nature of the velocity data in more serious ways.

Firstly, the Fourier Transform is by definition an integration from negative infinity to plus infinity. By Fourier Transforming an interrogation area of finite size, it is implicitly assumed that the input data is periodic, consisting of continually repeating copies of the interrogation area data. In turn, this means that the correlation plane itself is periodic. Cross-correlating two interrogation areas of size $N \times N$ in Fourier space results in a correlation plane also of size $N \times N$. The location of the displacement peak is relative to the *centre* of the correlation plane; therefore a peak corresponding to a displacement d_{actual} of greater than $\frac{N}{2}$ will be 'wrapped around' and mapped to a new position $d_{measured}$ such that $d_{measured} = d_{actual} - N$. The correlation function is then said to be *aliased*, and the displacement peak will not result in a velocity vector that accurately represents the flow. This problem can be avoided by either increasing the size of the interrogation area or reducing the frame time separation, Δt.

The finite size of the interrogation area also results in a bias towards small velocities. Only particles common to both samples will contribute to the dis-

placement peak. As the mean displacement increases, there will be fewer particles imaged within both interrogation areas, so the correlation peak will be lower. The correlation function is thus weighted by a window function which depends on the area of overlap. This can be seen in figure 4.3.

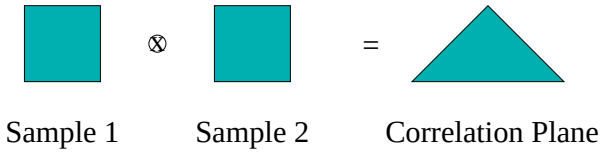

Figure 4.3: The Window Function

If the correlation coefficients are not weighted to compensate for this, the displacement peak will be shifted towards the centre of the correlation plane, and the velocity vector obtained from this will be lower than the actual fluid velocity.

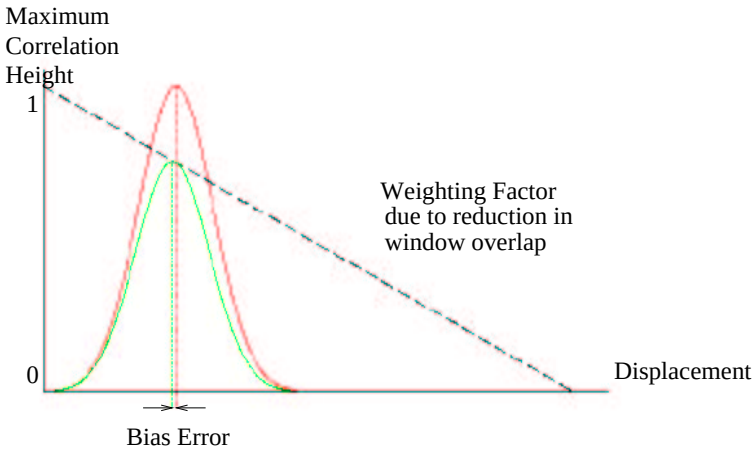

Figure 4.4: Bias Error

There are three methods for removing this bias. The first is to use the window function to calculate coefficients for adjusting the correlation values. Specifically,

each point in the correlation plane should be divided by $1 - \frac{r}{I}$, where r is the distance from the point being corrected to the centre of the plane, and I specifies the size of the interrogation area. This correction factor involves scaling the correlation data by a factor greater than 3 at the corners of the correlation plane, which can lead to outliers if the signal-to-noise ratio of the displacement peak is less than 3. Since the optimum displacement should be less than a quarter of length of the interrogation area, one can assume that peaks at the edges of the correlation plane correspond to noise rather than the mean displacement. The correction factor can modified to reflect this [37].

Another way is to use unequal sizes for the interrogation area. If one interrogation edge is twice the other, the window function then has a plateau, as seen in figure 4.5.

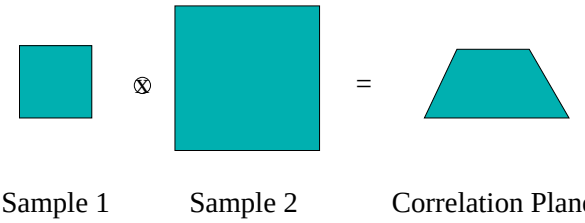

Figure 4.5: The Window Function for unequal Interrogation Areas

One way of increasing the size of an interrogation area is to centre the original data and surround these points with zero values. This method is known as *zero padding*. The abrupt change between recorded pixel values and these zero values can introduce high frequency artifacts into the correlation plane. This can

be avoided by removing the mean value of the interrogation area's pixels and performing a normalised correlation.

The third and most effective method of removing this bias error is called *re-interrogation*. This technique of PIV analysis has other advantages and is discussed further in section 4.8.

4.7 Peak Detection

The maximum value in the correlation plane yields the mean displacement to an accuracy of $\pm\frac{1}{2}$ pixel. A size of 32×32 is commonly chosen for the interrogation area, so the *minimum* error is 3%, corresponding to the maximum displacement of 16 pixels. For smaller displacements, this error will be significantly larger. The error can be reduced, however, by using the correlation coefficients of the peak value's neighbours. There are different ways in which this can be done. One method is to calculate the *centroid* of the peak, defined as the ratio of the first order moment to the zeroth order moment. This method was used in early, wet-film PIV as the peaks tended to be rather broad, so many values were involved in the moment calculation. However, it often proved difficult distinguishing the edge of correlation peak from background noise.

CCD cameras have a much lower resolution than wet-film, so to make efficient use of their pixels, the image of a tracer particle tends to be fairly small, around

a couple of pixels across. This reduces the width of the peaks in the correlation plane, so the centroid calculation became unreliable. The peak is now calculated using a *three point estimator*. If the highest point in the correlation plane is $R_{i,j}$, its nearest neighbours are $R_{i-1,j}$, $R_{i,j-1}$, $R_{i+1,j}$ and $R_{i,j+1}$. A curve is fitted to the three points in the x direction, and the maximum value of this curve is assumed to be located at the x coordinate of the correlation peak. This process is then repeated for the y coordinate. Generally, the function fitted to the correlation values is a Gaussian; the formula is shown in equation 4.8.

$$\begin{aligned} x_0 &= i + \frac{lnR_{(i-1,j)} - lnR_{(i+1,j)}}{2lnR_{(i-1,j)} - 4lnR_{(i,j)} + 2lnR_{(i+1,j)}} \\ y_0 &= j + \frac{lnR_{(i,j-1)} - lnR_{(i,j+1)}}{2lnR_{(i,j-1)} - 4lnR_{(i,j)} + 2lnR_{(i,j+1)}} \end{aligned} \tag{4.8}$$

The use of a gaussian function can be justified since the correlation of two gaussians is also gaussian. Thus the assumption that the correlation peak is a gaussian implies that the original particle images are gaussians. As discussed in section 4.2, this is a good approximation if the particle images are diffraction limited.

The size of the tracer particle image, like so many parameters in PIV, is a compromise. If the diameter is too large, the changes in the correlation values near the peak are too small for the three point estimator to provide an accurate value for the peak. But if the diameter is too small, the neighbouring values will

be dominated by noise. Trying to fit a gaussian or other three point estimator to the peak biases the displacements towards integer values, an effect is known as *peak locking*. The optimum particle image diameter for digital PIV is just over 2.0 pixels for auto-correlation (single image, double exposure), or around 1.5 pixels for cross-correlation (double image, single exposure). The cause of this discrepancy is unknown [36].

If peak detection is used and all of the experimental parameters are appropriately chosen, the uncertainty in the displacement measurement can be less than 0.1 pixels.

4.8 Advanced Correlation Techniques

The RMS uncertainty in the displacement measurement rises dramatically for displacements above around 0.5 pixels. In addition, a significant mean displacement will reduce the quantity of particle-pairs, since a number of particles will either enter or leave the interrogation area between exposures. This will decrease the S/N ratio of the correlation plane. Using *re-interrogation* in the analysis of PIV images minimises the particle displacement, and hence the measurement error. Initially, the two interrogation areas are cross-correlated, as before. Once the mean displacement has been obtained from the principal peak, the first interrogation area is shifted by this displacement (to the nearest integer). The

shifted interrogation area is next cross-correlated with the second interrogation area. The principal peak should then be located near the centre of the correlation plane.

The analysis of PIV images can be improved further by reducing the size of the interrogation area in successive passes of the correlation routine. In this way, interrogation areas smaller than the mean particle displacement can be used. This has the effect of increasing the spatial resolution of the flow measurement, allowing smaller structures and higher wavenumbers to be resolved.

Work on optimising PIV analysis is ongoing. This includes combining PIV and PTV by using the statistical displacements obtained from correlations [45], and fuzzy logic analysis of the correlation plane [46], to track individual particles, thereby increasing the spatial resolution of the flow measurements. Wernet [47] has also used fuzzy logic data validation of the correlation peaks to reduce the number of outliers and hence improve the statistical independence of the velocity vectors.

In addition, algorithms are being developed to allow the interrogation area to have an arbitrary shape [48]. This free shape is padded with zeros until its size is a power of two, then correlated. By incorporating free shaped interrogation areas, it is possible to increase the resolution of PIV measurements near obstacles such as aeroplane wings.

These developments, together with the fact that camera and computer technology are continuing to improve dramatically, means that PIV is likely to become an increasingly effective technique for flow measurement.

4.9 PIV in more than 2 Dimensions

The method described so far is capable of yielding two velocity components in a two dimensional plane. If the light sheet is situated in the xy plane, therefore, it is not possible to obtain information about the z component of the fluid velocity. Ultimately, however, it would be useful to obtain all three velocity components throughout the volume of interest, as a function of time. The efforts to increase the dimensional size of the data have been reviewed by Hinsch [49].

The most commonly used three-dimensional method is *stereo PIV*, which is based upon 3d vision in animals i.e. two cameras record the same object from separate locations; the differences in the two images yield depth information. This technique is more difficult to perform than 2d PIV because of factors such as perspective distortion. The error in the out-of-plane velocity depends on the angle between the cameras and is typically at least twice that of the in-plane velocity [50].

To measure the 3d velocities of the breaking water waves, the technique of *Dual-Plane PIV* was implemented. This method is described in the following section.

4.10 Dual-Plane PIV

Out-of-plane motion shifts particles outwith the light sheet, reducing the S/N ratio of the correlation plane and increasing the likelihood of outliers. Also, the light sheet is of finite width, so particle pairs can exist at different positions of z. This results in perspective errors which increase the uncertainty in the in-plane velocities. Dual-plane PIV uses this loss in correlation to estimate the out-of-plane velocity [51].

The technique involves taking 3 images of the flow, I_0, I_1 and I_2, two of which are taken with the light sheet at one z position, while the third is taken with the light sheet displaced in the z direction. This displacement is less than the thickness of the laser beam such that the two light sheets overlap. Let the images be captured at times $t = t_0$, $t = t_0 + \Delta t$ and $t = t_0 + 2\Delta t$. The in-plane velocities can be obtained as before, by cross-correlating interrogation areas within images 0 and 1, or 1 and 2, and locating the centre of the principal peak in the correlation plane. As mentioned in section 4.5, the height of the principal peak depends on the number of particle pairs. This number is proportional to the number of particles within the interrogation area at time t_0, less those that have moved in-plane but outwith the interrogation area by time $t_0 + \Delta t$, less those that have moved out of the light sheet plane altogether.

If the out-of-plane motion is in the direction of the light sheet displacement,

there will be more particle pairs than if the light sheet displacement is zero (as in 2d PIV) or in the opposite direction. By comparing the heights of the principal peaks obtained by cross-correlating images 0 and 1, and 1 and 2, the magnitude and direction of the out-of-plane velocity can be estimated. The mathematics of Dual-Plane PIV will be outlined in the following section.

4.10.1 Dual Plane Correlation

Let the three lightsheet positions be Z_0, Z_1 and Z_2. Assume that the displacement $\mathbf{D}$ of the tracer particles has components D_x, D_y and D_z.

The correlation coefficient at a point (i, j) between images 0 and 1, $R_{01}(i, j)$, and images 1 and 2, $R_{12}(i, j)$, can be written as [52]:

$$\begin{aligned} R_{01}(i,j) &= R_{00}(i - MD_x, j - MD_y)F_0(D_z - Z_1 + Z_0) \\ R_{12}(i,j) &= R_{11}(i - MD_x, j - MD_y)F_0(D_z - Z_2 + Z_1) \end{aligned} \tag{4.9}$$

where M is the magnification of the image, $R_{00}(i, j)$ is the self-correlation of image 0, $R_{11}(i, j)$ is the self-correlation of image 1, and $F_0(Z)$ is the loss of correlation due to out-of-plane motion. Mathematically,

$$F_0(D_z) = f(z) \otimes f(z) = \frac{\int_{-\infty}^{+\infty} f(\alpha) f^*(\alpha - z) d\alpha}{\int_{-\infty}^{+\infty} f(z)^2 dz} \tag{4.10}$$

where $f(z)$ is the intensity profile of the laser beam. In practice, the normalised correlation coefficient at a point is obtained by cross-correlating over a finite spatial average, the interrogation area, as defined in equation 4.6. The expectation value of this correlation is

$$\begin{aligned} E\left\{R_{01}(i,j)\right\} &= C_R R_{00}(i - MD_x, j - MD_y) F_0(D_z - Z_1 + Z) F_I(i,j) \\ E\left\{R_{12}(i,j)\right\} &= C_R R_{11}(i - MD_x, j - MD_y) F_0(D_z - Z_2 + Z_1) F_I(i,j) \end{aligned} \tag{4.11}$$

where C_R is a constant and $F_I(i,j)$ represents the loss of correlation due to in-plane motion. At the tip of the principal peak, $i = MD_x$ and $j = MD_y$, and equation 4.11 becomes

$$\begin{aligned} E\left\{R_{01}(MD_x, MD_y)\right\} &= C_R R_{00}(0) F_0(D_z - Z_1 + Z_0) F_I(MD_X, MD_Y) \\ E\left\{R_{12}(MD_x, MD_y)\right\} &= C_R R_{11}(0) F_0(D_z - Z_2 + Z_1) F_I(MD_X, MD_Y) \end{aligned} \tag{4.12}$$

If the loss of correlation due to in-plane motion, $F_I(D_x, D_y)$, is assumed to be the same for R_{01} and R_{12}, the out-of-plane motion can be calculated by taking the ratio of the normalised correlation coefficients:

$$\frac{R_{01}}{R_{12}} = \frac{F_0(D_z - Z_1 + Z_0)}{F_0(D_z - Z_2 + Z_1)} \tag{4.13}$$

In order to determine the out-of-plane displacement, therefore, it is necessary

to know the intensity profile of the light sheet, $f(z)$. For a continuous wave laser, $f(z)$ is approximately gaussian, i.e.

$$f(z) = I_0 e^{-\left(\frac{2z}{\Delta z}\right)^2} = I_0 e^{-\frac{4z^2}{\Delta z^2}} \tag{4.14}$$

where I_0 is the intensity at the centre of the light sheet and Δz is its width, measured from the $\frac{1}{e}$ intensity points. The correlation of two gaussians, each of width Δz, is also a gaussian, of width $\sqrt{2}\Delta z$:

$$F_0(D_z) = \frac{\int_{-\infty}^{+\infty} I_0 e^{-\left(\frac{2z}{\Delta z}\right)^2} I_0 e^{\left(\frac{2(\alpha - z)}{\Delta z}\right)^2} d\alpha}{\int_{-\infty}^{+\infty} \left\{ I_0 e^{-\left(\frac{2z}{\Delta z}\right)^2} \right\}^2 dz} = I_0 e^{-\left(\frac{\sqrt{2}z}{\Delta z}\right)^2} = e^{-\frac{2z^2}{\Delta z^2}} \tag{4.15}$$

In these dual-plane experiments, the middle exposure consists of images of tracer particles illuminated in the displaced light sheet, in order to measure out-of-plane motion in both z directions. Thus, in the equations above, $Z_0 = Z_2$. Using this, substituting for F_0 using equation 4.10, and rearranging for D_z yields:

$$D_z = \frac{\Delta z^2 (\ln R_{01} - \ln R_{12})}{8(Z_1 - Z_0)} \tag{4.16}$$

The out-of-plane velocity can be obtained by dividing D_z by the time separation between the images, Δt.

4.10.2 Accuracy of Dual-Plane PIV

The uncertainty in the out-of-plane velocities, neglecting errors in the light-sheet width, profile and shift is inversely proportional to the number of particles within the interrogation area [53]. For this reason, the seeding density is usually higher in dual-plane experiments than in 2d PIV. Because the calculation of the out-of-plane velocity involves more variables than the in-plane velocity, such as lightsheet parameters, its associated uncertainty is larger.

4.10.3 Variations on dual-plane PIV

The assumption that the reduction in particle pairs due to in-plane motion is the same for both correlations is only an approximation. The need for this assumption can be avoided by capturing the 2nd and 3rd images simultaneously. Since two images must then be captured in distinct light sheet planes at the same time, image separation is required. One method is to use a direct vision prism, which disperses an incident beam into separate beams, parallel with the original, by an amount dependent on the wavelength. The beam from an Argon-Ion laser, for instance, could be split into two beams of wavelengths 514nm and 488nm which could then be used to produce light sheets of different colours at different z values. By using appropriate, narrow band-pass filters, the images of tracer particles illuminated by two light sheets can be captured on separate cameras at the same time. The mathematics of this approach is slightly different, and can

be found in [54].

The errors involved in dual-plane PIV are larger than in stereo PIV. Nevertheless, dual-plane PIV is easier to implement for low-speed flows, and can be carried out using a single camera; it is often difficult or impossible to perform stereo PIV due to limits in the optical access of the fluid. A detailed description of stereo PIV can be found in [36].

4.11 Final Remarks

In this chapter, the technique of 2d and dual-plane PIV have been reviewed. The in-plane flow velocities are obtained by locating the peak of the correlation plane, obtained by cross-correlating interrogation areas from two images. Out-of-plane motion reduces the height of the correlation peak; dual-plane PIV uses this reduction to estimate the out-of-plane velocities.

Software was written, mainly by the author, to perform the 2d and dual-plane PIV analysis described in this chapter. The program contained source code written by Will Hossack to perform the FFT algorithm, Tim Dewhirst's code for drawing the 3d correlation plane graphics and a modified version of David Hann's Vector structure.

The dual-plane PIV experimental apparatus and the results obtained are presented in chapter 8.

Chapter 5

4-camera System

5.1 Introduction

As stated in chapter 4, it is possible to perform dual-plane PIV with a single camera. However, the frame rate of a CCD camera is inversely related to its array size, resulting in a compromise between spatial and temporal resolution. One way of overcoming this problem is to use more than one camera. The way in which this can be done is the subject of this chapter.

5.2 Multiple Camera Systems

The first multiple camera system was designed by Eadweard Muybridge in the 1870s, who arranged a row of cameras with trip wires to prove for the first time that a galloping horse did in fact lift all four hooves from the ground at some stage of its stride. This idea of triggering separate cameras in quick succession to record motion can be used for PIV experiments if the cameras can be arranged to view the same object.

5.2.1 Multiple Images

To produce multiple, identical images of a single object, the light refracted by the lens must be divided before it reaches the image plane. This can be done by reflection. Dewhirst [37] built both 2- and 4-camera systems, with one and three beam splitters respectively, positioned behind the lens. Each beamsplitter allows 50% of the light to be transmitted while the other half is reflected by 90 degrees. For the 2-camera system, this division results in the formation of two image planes; the additional beamsplitters in the 4-camera system further divide the light either transmitted or reflected by the first beamsplitter, thereby creating four image planes.

Thus Dewhirst's 4-camera system would be suitable for performing dual-plane PIV. By triggering three cameras in turn, when the lightsheet is in its appropri-

ate position (original, displaced, original), the images required for obtaining 3d velocity measurements can be obtained. Such a camera system can also be used for measuring fluid accelerations and high-speed events.

Because the light is split two (or four) ways, the brightness of each image is half (or a quarter) that of the image that would be formed were there no beamsplitters present. Another feature of these multiple camera systems is that half of these images are inverted, as in a single camera, and half are the orientation of the original object. This can easily be corrected using software. But introducing a medium with a refractive index different from air into the region between the lens and the image plane affects the image quality as well as orientation and brightness. Equation 8.1 specifies the displacement caused by a beam passing through a piece of transparent material. Since the refracted light intercepts the air-glass boundary at different angles, the amount of displacement varies from beam to beam. This reduces the back focal length and introduces spherical aberration into the image.

However this is not a serious drawback, due to the size of the CCD array. Dewhirst's camera systems use a standard SLR camera lens which is designed for use with film of dimension $36 \times 24mm$. But the cameras used in his system are Pulnix TM-9701s which have CCD arrays approximately $10mm$ by $8mm$. This corresponds to merely the central 9% of the acceptable imaging area, where any aberrations are small.

To make full use of the pixel resolution, any misalignment between the individual arrays must be as small as possible. A slight misalignment, less than 10 pixels, can be corrected using software. This means that the arrays should be aligned to better than $0.1mm$. In order to align the 4-camera system, it was necessary to disconnect the power to the individual cameras, remove the 18 pin CCD array from its chip, position the array until it appeared to overlap each of the others, then reconnect the chip, power up the cameras and test the alignment. This process was difficult, time-consuming and resulted in damage to all four cameras. For this reason, a new design for a 4-camera system was built, where the alignment could be performed with the cameras running.

5.3 4-Camera System

The design was based on an ultra high-speed video camera system developed at the German Aerospace Research Establishment [55]. The geometry of its image formation is described in this section to demonstrate how four cameras can view the same object, and in order to justify aspects of the design criteria concerning the image alignment.

Consider a rectangular object of width $2W$ and height $2H$ located in the xy plane and centred at the point $(0, 0, L + (M - bfl))$, where L is the distance from the object plane to the image plane and bfl is the back focal length of the lens

(figure 5.1).

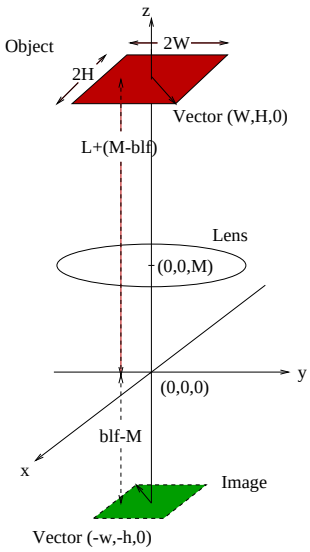

Figure 5.1: Diagram showing object, image and vector joining centre to corner

Let us define a vector **v** pointing from the centre of the object to the corner in the $+x, +y$ quadrant, (W, H, O). If the optical centre of the back principal plane of the lens is situated at $(0, 0, M)$, a focused image will be formed in the xy plane, centred at $(0, 0, M-bfl)$. The corner $(W, H, L+(M-bfl))$ of the object is mapped to a point $\mathbf{P} = (W \times mag, H \times mag, M - bfl)$, where mag is the magnification. Since mag is negative, $\mathbf{P}$ can be written as $(-W \times |mag|, -H \times |mag|, M-bfl)$. If $w = W \times |mag|$, $h = H \times |mag|$ and $z = bfl - M$, point $\mathbf{P}$ becomes $(-w, -h, -z)$.

5.3.1 Pyramid Mirror

Consider the effect of inserting a square pyramid mirror behind the lens. Assume that the tip of the mirror is located at $(0, 0, 0)$, the angle between vertices

and the base is 45^0 and the base lies in the xy plane.

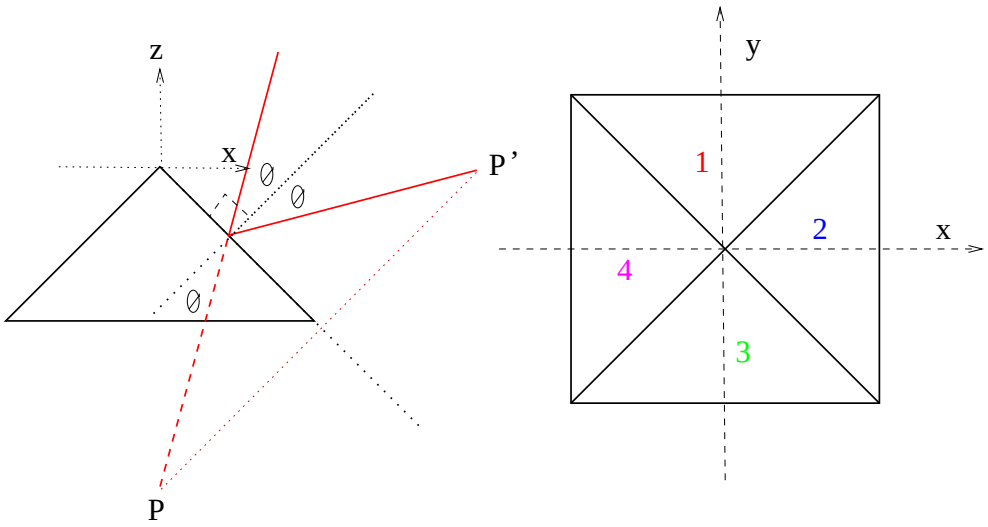

Figure 5.2: Pyramid mirror from side (left) and above (right)

Each refracted ray that was travelling to form the image in the xy plane at $-z$ is now reflected about the normal of whichever face it intercepts. Rays that were heading towards point **P** are thus reflected in four different directions, and now focus at four different points. The location of these points is the reflection of **P** in the four mirror faces. One such reflection is shown in figure 5.2 (left).

Faces $1-4$ of the mirror are defined by the planes $z=-y$, $z=-x$, $z=y$ and $z=x$. Reflections in these planes can be represented mathematically by transformation matrices; these matrices and the points to which the centre and **P** are mapped, **Centre**$'$ and **P**$'$, are shown below.

Mirror Face	Transformation Matrix	**Centre′**	**P′**
1	$\begin{pmatrix} x \\ -z \\ -y \end{pmatrix}$	$(0, z, 0)$	$(-w, z, h)$
2	$\begin{pmatrix} -z \\ y \\ x \end{pmatrix}$	$(z, 0, 0)$	$(z, -h, w)$
3	$\begin{pmatrix} x \\ z \\ y \end{pmatrix}$	$(0, -z, 0)$	$(-w, -z, -h)$
4	$\begin{pmatrix} z \\ y \\ x \end{pmatrix}$	$(-z, 0, 0)$	$(-z, -h, -w)$

The vectors joining **Centre′** and **P′**, as seen when facing the origin, are shown in figure 5.3.

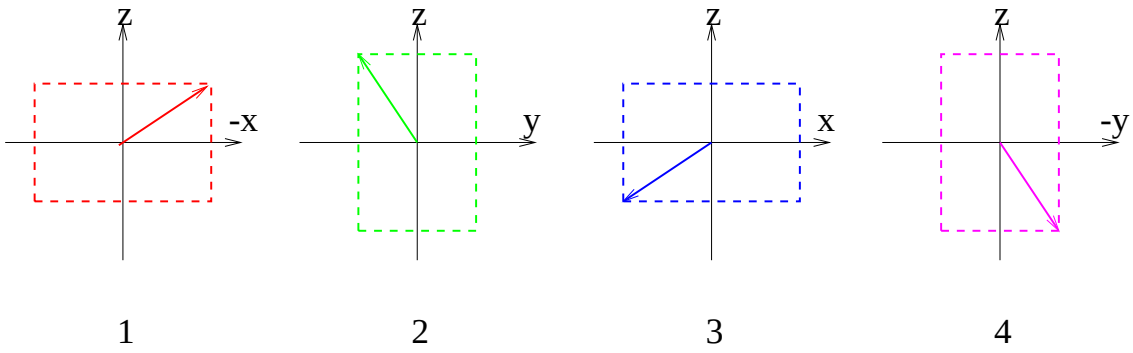

Figure 5.3: Vectors showing position and orientation of new images

Each of the four faces of the mirror reflects light rays that were heading for the same point in the original image. Therefore, the addition of the pyramid mirror results in the formation of four complete images. Two of these images are in the xz plane centred on $y = 0$ (vectors 1 and 3), and two lie in the yz

plane centred on $x = 0$ (2 and 4). Like the original image, the new images are a distance $z = blf - M$ from the mirror tip. The orientation of the vectors reveals the orientation of the resulting images. Most noticeably, each vector is rotated by 90^0 relative to its previous number. Since the arrays are not square, it is necessary to rotate the arrays for recording the image by 90^0 also, or the arrays will not be imaging the same object.

In addition to the rotation, each image is inverted and reflected in either the $x = 0$ plane (images 1 and 3) or $y = 0$ (images 2 and 4). The inversion can be compensated for by simply rotating the whole arrangement by 180^0 about the z axis. The 'left-right' image inversion due to reflection in the $x = 0$ or $y = 0$ planes can be removed using software if required.

In summary, inserting a pyramid mirror behind the camera lens results in the formation of four images. Four separate CCD arrays, appropriately positioned and rotated, will thus record exactly the same object.

5.3.2 Misalignments

The pyramid mirror, like any solid body, has six degrees of freedom which determine its position: x, y, z specifying location in space, and θ, ϕ and ψ determining the orientation relative to the x, y and z axes respectively. The above description of image formation relies on the mirror tip being located at the origin

($x = y = z = 0$), the mirror base lying in the xy plane ($\theta = \phi = 0$), and the mirror's vertices being in the $y = x$ or $y = -x$ planes ($\psi = 0$).

If these conditions are violated, the images will form at different positions to those described above. Equivalently, arrays centred on the x and y axes, a distance z from the origin will not be aligned. Since the images are formed in different planes, it is difficult to make a direct comparison between their coordinates. To quantify the misalignment, it is useful to consider the apparent array position as seen by looking down upon the mirror tip. Each array is then reflected in the corresponding mirror face. If the mirror and arrays are correctly positioned, the arrays will be superimposed upon the original image plane. If not, the arrays will not completely overlap, as seen in figure 5.4.

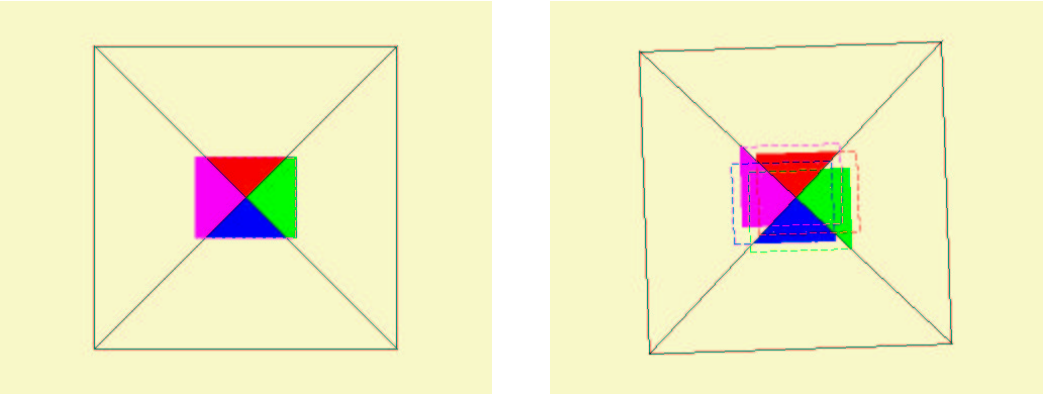

(a) Mirror Correctly Positioned

(b) Mirror wrong height and orientation

Figure 5.4: Aligned and Misaligned arrays

Let us term a non-zero z value as an *height error*, a non-zero x and/or y value

as an *mirror offset* and a non-zero value of ψ and/or θ and/or ϕ as a *rotation error*. These errors will be investigated in turn.

Height Error

If the tip of the mirror is at $(0, 0, \Delta z)$, the four images will be formed centred at a distance $M + \Delta z$ from the tip and a height Δz above the x and y axes.

The arrays, centred on the x and y axes a distance z from the origin, are reflected in the planes $z = -y + \Delta z$, $z = -x + \Delta z$, $z = y + \Delta z$ and $z = y + \Delta z$ respectively. The transformations are then as follows:

Array Number	Transformation Matrix	Array Centre	Apparent Centre
1	$\begin{pmatrix} x \\ -z + \Delta z \\ -y + \Delta z \end{pmatrix}$	$(0, z, 0)$	$(0, \Delta z, -z + \Delta z)$
2	$\begin{pmatrix} -z + \Delta z \\ y \\ -x + \Delta z \end{pmatrix}$	$(z, 0, 0)$	$(\Delta z, 0, -z + \Delta z)$
3	$\begin{pmatrix} x \\ z - \Delta z \\ y + \Delta z \end{pmatrix}$	$(0, -z, 0)$	$(0, -\Delta z, -z + \Delta z)$
4	$\begin{pmatrix} z - \Delta z \\ y \\ x + \Delta z \end{pmatrix}$	$(-z, 0, 0)$	$(-\Delta z, 0, -z + \Delta z)$

Two problems arise from the mirror tip being located at $(0, 0, \Delta z)$: firstly, the images formed may be blurred since the arrays are a finite distance Δz from

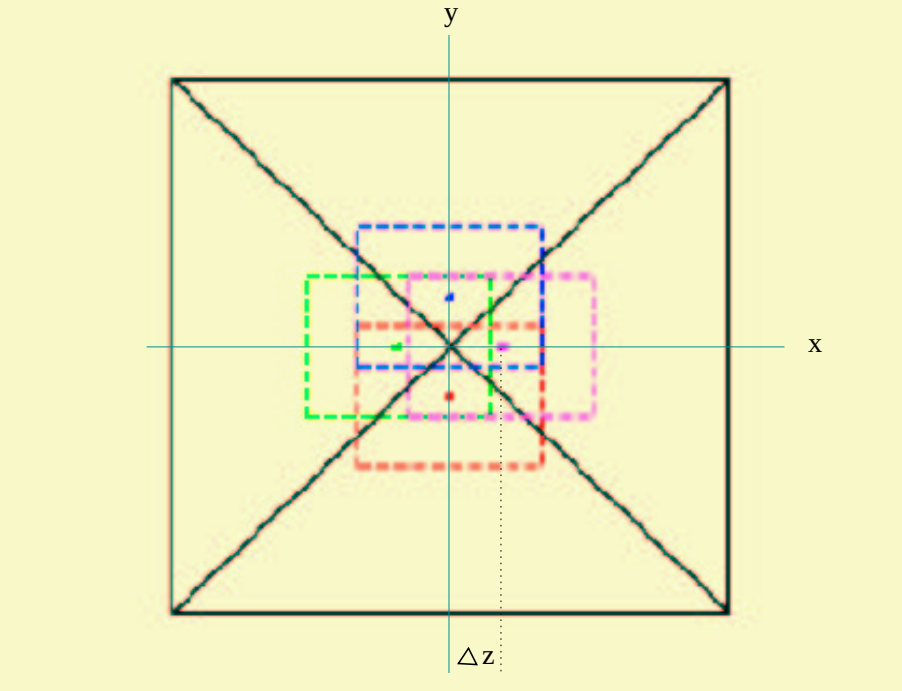

Figure 5.5: Array Misalignment due to Mirror Height Error

the image plane; secondly, and more seriously, the change in height z moves the centre of each image towards four different edges of the four arrays, due to their 90^0 rotation. The amount of misalignment is $2\Delta z$ for opposite arrays and $\sqrt{2}\Delta z$ for adjacent arrays (figure 5.5).

Mirror Offset

Now let the mirror tip be located at the point $(\Delta x, \Delta y, 0)$. The base is still assumed to be in the xy plane. The centres of the arrays and their reflections as seen from above are as follows:

Array Number	Actual Centre	Apparent Centre
1	$(0, z, 0)$	$(0, \Delta y, \Delta y - z)$
2	$(z, 0, 0)$	$(\Delta x, 0, \Delta x - z)$
3	$(0, -z, 0)$	$(0, \Delta y, -\Delta y - z)$
4	$(-z, 0, 0)$	$(\Delta x, 0, -\Delta x - z)$

The arrays are located a distance Δy (for 1 and 3) or Δx (for 2 and 4) from the image planes. Unless these distances are both less than the depth of field of the lens, focusing difficulties will occur. A misalignment between the odd-numbered and even-numbered arrays occurs because their centres are at different values of x and y. But there is an additional misalignment between all the arrays due to the fact that the arrays are different distances from the image plane, so will view objects of different sizes.

Rotation Error

Now assume that the mirror has been rotated by an angle ψ about the z axis. To simplify the analysis, let the coordinate system rotate by the same amount. In this new coordinate system, the arrays have effectively been rotated by $-\psi$ about the z axis. When reflected in the mirror's surfaces, which remain $z = \pm y$ and $z = \pm x$ in the new coordinates, the centres and vectors of these rotated arrays are transformed as follows:

ActualCentre	ApparentCentre	ActualVector	ReflectedVector
$(z\sin\psi, z\cos\psi, 0)$	$(z\sin\psi, 0, -z\cos\psi)$	$(-w\cos\psi, w\sin\psi, h)$	$(-w\cos\psi, -h, -w\sin\psi)$
$(z\cos\psi, -z\sin\psi, 0)$	$(0, -z\sin\psi, -z\cos\psi)$	$(-h\sin\psi, -h\cos\psi, w)$	$(-w, -h\cos\psi, h\sin\psi)$
$(-z\sin\psi, -z\cos\psi, 0)$	$(-z\sin\psi, 0, -z\cos\psi)$	$(-w\cos\psi, w\sin\psi, -h)$	$(-w\cos\psi, -h, w\sin\psi)$
$(-z\cos\psi, z\sin\psi, 0)$	$(0, z\sin\psi, -z\cos\psi)$	$(-h\sin\psi, -h\cos\psi, -w)$	$(-w, -h\cos\psi, -h\sin\psi)$

If ψ is small, the vectors joining the centre of the reflected array to its corner can be approximated by $(-w, -h, -w\psi)$, $(-w, -h, h\psi)$, $(-w, -h, w\psi)$ and $(-w, -h, -h\psi)$. The corresponding vector in the original image (formed without the mirror) was $(-w, -h, 0)$. The vectors above are defined in the rotated coordinate system; the fact that the x and y components of these vectors are the same as the original vector suggests that the reflections of the arrays are rotated with the mirror. In addition, the z components are finite for a non-zero value of ψ so the reflections of the arrays do not exist in the xy plane. This means that different parts of the array are different distances to the image plane, so the focus of the image will change across the array.

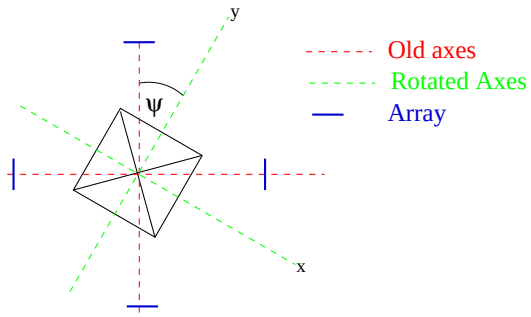

Figure 5.6: Orientation Error

The distance between the centres of opposite arrays is $2z\sin\psi$; for adjacent arrays this distance is $\sqrt{2}z\sin\psi$. Both the misalignment and the focusing problem

mentioned above increase with increasing ψ.

Non-zero values of θ and/or ϕ, corresponding to a rotation about the x or y axis, is mathematically similar to the rotation error. Once again there is a misalignment between the arrays and focusing difficulties due to an angle between the image plane and the array plane.

5.3.3 Removal of misalignments

Misalignments are undesirable as they diminish the area of array overlap, reducing the area over which measurements can be performed. A rotation of the mirror also reduces the quality of the images recorded, since it is not possible to focus the image across the entire array.

The removal of array misalignment will be discussed in the following section, where the practicalities of building such a camera system are considered. Here it is noted that a translational error in the mirror position can be corrected by a translational shift of the arrays, while a rotational error will require the arrays themselves to be tilted.

5.4 Design of 4-Camera System

In order to build a camera based on the multiple image formation described above, it was necessary to obtain a pyramid mirror. The mirror was chosen to have a base side of length 30mm, sufficiently large to avoid restricting the angular field of view. The error in the internal angle 45^0 was specified to be less than $\pm 20''$, ensuring that any deviation from the image position quoted in section 5.3.1 is less than a single pixel. The mirror surface is flat to within $\frac{\lambda}{10}$, where $\lambda = 633nm$, so any distortions in the image due to variations in flatness are minimal. The mirror was coated with silver, which is highly reflective throughout the visible spectrum, and was custom made by Fleige Optik in Germany.

Due to the physical size of the CCD chip in the Pulnix cameras, it was not possible to use a standard SLR lens in this design. A Hasselblad lens was used instead because its $80mm$ back focal length is nearly twice that of the SLR. The size of the camera body housing the CCD array also limited the value of M, the distance from the mirror tip to the back of the lens. M must be large enough that the camera bodies clear the lens and small enough that they do not touch the mirror. It was decided to set $M = bfl/2$, such that the mirror tip is equidistant from the lens mount and the arrays.

The Hasselblad lens is designed to produce an image $60 \times 60mm$, so the Pulnix array occupies just over 2% of the centre of the imaging area. Since the

light travels through air alone between the lens and the image plane, the image quality will not be compromised.

The focal length of the Hasselblad lens is $80mm$. This is long compared to a standard SLR lens, and this fact, combined with the small size of the CCD array, means that the angular field of view is less than 10^0. However, the magnification condition that the tracer particle image diameter should be of the order two pixels means that the maximum image width suitable for PIV analysis is around $30cm$ (from experience, or around 10 times the theoretical value from equation 4.3 which is a severe underestimate). This corresponds to a magnification of around 0.03, which can be obtained by setting $L = 2.5m$. In other words, although the field of view of an $80mm$ lens is small, the maximum region of flow that can be measured is also small, so the camera does not have to be located an impractically large distance from the motion of interest.

A photograph of the camera system during development is presented in figure 5.7[1]. Because of the space restrictions, it was impractical to construct mechanisms for adjusting all six degrees of freedom of the mirror and arrays. Instead, the mirror was centred and held in place on a platform by an O-ring. This platform could be moved up and down the z axis by rotating **A** in figure 5.7, and the mirror could be rotated using two positioning bolts (**B**). That is, the mirror can be shifted up and down, and rotated about the z axis, or moved in three of its

[1]Photograph by Peter Tuffy

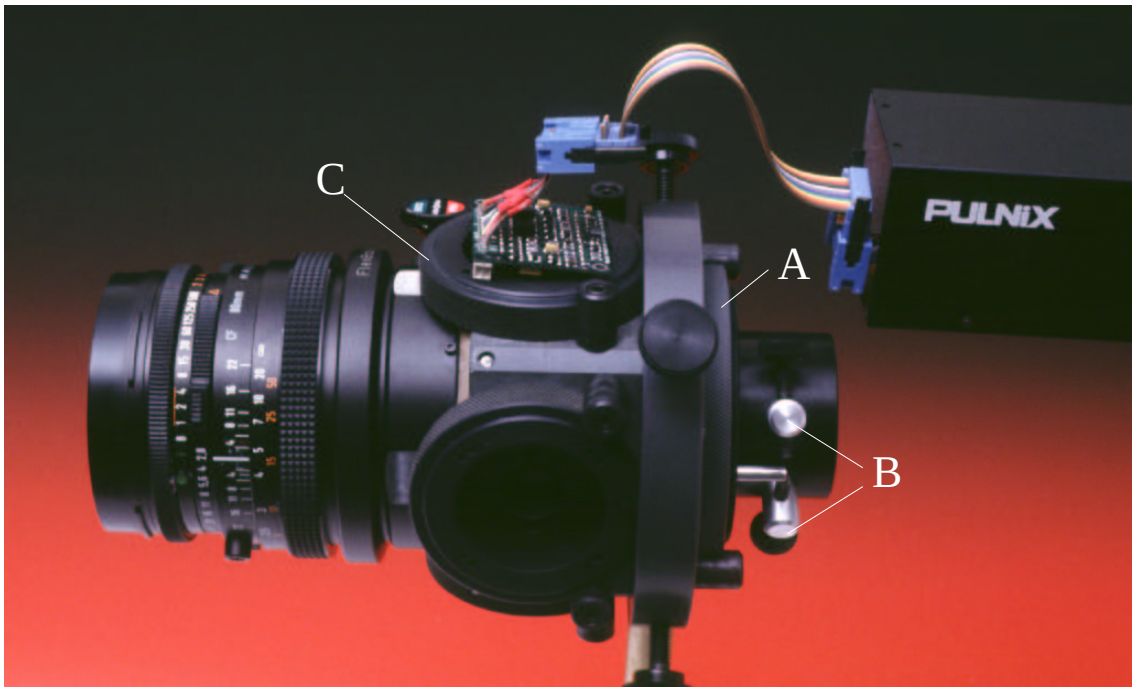

Figure 5.7: Four Camera System

degrees of freedom.

The CCD chips have holes of diameter 3mm in two diagonally opposite corners. Screws of diameter 2.5mm were used to hold the arrays in place, allowing $\pm 0.5mm$ displacement. Each array could also be moved by up to $1mm$ towards or away from the mirror, to allow individual focusing of the images and to correct for any mirror offset, by rotating **C**.

With these adjustment mechanisms, it was possible to align the individual CCD arrays to within approximately $25\mu m$, or two pixels. The residual mis-

alignment was measured by recording an image of some tracer particles, and performing a PIV cross-correlation between the images obtained by the different cameras. By performing a least-squares-fit on the resulting vector maps, coefficients for removing the misalignments could be obtained [37].

5.5 Drawbacks of Design

The Pulnix cameras used in the 4-camera system were those from Dewhirst's camera system, which had the ribbon cable connecting the CCD array to the camera body extended. In order to make a more compact camera, these cables were extended an additional $5cm$. With hindsight, it would have been desirable to *reduce* the length of the extended cables such that the CCD arrays could be housed in the camera body. While resulting in a bulkier camera system, this approach would have reduced two problems inherent in the design.

Firstly, because the CCD arrays are exposed, they are more subject to noise than if shielded by the camera body. In particular, bands of lighter and darker regions were superimposed on the images, which was believed to be a beating effect due to fractional differences in the clock frequencies of the separate cameras. The appearance of these bands was lessened by shielding the cables with grounded foil. Secondly, the extension of the cables seemed to decrease the reliability of the cameras significantly. Each of the cameras had to be sent off for repair at least

once. This did not happen to the same extent to the TM-9701 cameras which were left intact.

An artefact of the incorporation of the pyramid mirror is that the brightness of the images from different cameras are not identical. Light rays which were heading towards a single point in the original image (figure 5.1) are divided by the mirror. However, other than at the centre of the image, the flux of rays impinging on each of the mirror faces is not equal. The result of this is that each of the images has a spatial variation in its brightness.

It is not possible to quantify this variation analytically [56], although it could be modelled using a suitable ray tracing package such as Zemax. The effect of a spatial variation in intensity was investigated by adding an artificial intensity gradient to some test PIV images from the PivNET website [2]. It was found that the effect on the velocity vectors obtained was negligible for gradients comparable to that from the 4-camera system. Thus it is not anticipated that the variation in brightness across the different images will affect the dual-plane results significantly.

A final disadvantage of this particular camera design is that it is not possible to use a standard SLR lens. This is due solely to the size of the TM-9701. SLR lenses are significantly cheaper than Hassleblads, and widely available with a range of focal lengths. The camera system would therefore be cheaper and more

[2]PivNET website - http://pivnet.sm.go.dlr.de/

versatile. Furthermore, the shorter back focal length of the SLR would result in the CCD arrays intercepting more of the light refracted by the lens. As CCD cameras get smaller, it would eventually be possible to shrink the design described above to produce a 4-camera system compatible with SLR lenses.

5.6 Conclusions

A 4-camera system capable of taking up to 120 frames per second was built. While designed to perform dual-plane PIV, the camera system could also be used as a high-speed camera by triggering the separate cameras in quick succession, or to measure accelerations in flows. The design also included space for filters, so it would be possible to use the camera for simultaneous PIV and LIF, by removing the fluorescent and laser light respectively.

Chapter 6

Extracting Information from LIF Images

6.1 Introduction

Chapter 3 contained a method for obtaining 'widescreen' LIF images whose grey levels correspond to known concentrations of a dispersing film. Each LIF experiment conducted produced approximately 2000 such images, so an automated analysis system is required. Software was written to extract various data from these images, in order to quantify and classify the dispersion. The parameters used to quantify the dispersion are discussed in this chapter.

6.2 Dispersion Parameters and Moments

Before this, the concept of the *moment* of a function, f, is reviewed. The moment is the expectation value of a specified power of the deviations from zero of all the values of a function. The power of these deviations is the *order* of the moment. Mathematically, the i^{th} order moment, m_i, of a one-dimensional function $f(x)$ is given by

$$m_i = \int x^i f(x) dx \tag{6.1}$$

More generally, f is a function of x, y, z and t, and the moments are written as

$$m_{i,j,k} = \int\int\int x^i y^j z^k f(x, y, z, t) dx dy dz \tag{6.2}$$

As an example, if f is the density distribution of a three-dimensional body, the $zero^{th}$ order moment is then the body's mass. For the purposes of the LIF analysis, f is a function representing the concentration distribution of the film with time. The $zero^{th}$ order moment is just the 2d "mass" of the rhodamine, while the 1^{st} and 2^{nd} order moments are used to calculate the mean and variance of the distribution. These moments will be used in the calculation of several dispersion parameters.

6.3 Depth Reached by Film

An obvious feature of the dispersion to investigate is the depth reached by the film material as a function of both time and concentration. The depth is considered to be relative to the mean water level (MWL) rather than the undulating surface, which reduces the computational time considerably. Starting from the MWL, each row in the image is scanned in turn for pixels of grey levels corresponding to a particular concentration. To avoid errors due to camera noise and residual background rhodamine, a row of three consecutive pixels of the appropriate brightness is required before the analysis software recognises that the film has indeed reached that particular row. The maximum depth for each concentration is stored for each image. This information can also be used to calculate a rate of descent for the film.

6.4 Area of Film

Calculation of the area of the film involves counting the number of pixels within each image which correspond to each of the twelve rhodamine concentrations. This provides information about the rate at which the patch is expanding, and about the transition from higher to lower concentrations.

6.5 Centre of Mass

The centre of mass of a three dimensional body is the point at which all first-order moments are at equilibrium. It moves as though the total mass and resultant external force were applied at its location. The position of the centre of mass is (x_0, y_0, z_0) where

$$x_0 = \frac{m_{1,0,0}}{m_{0,0,0}}, \qquad y_0 = \frac{m_{0,1,0}}{m_{0,0,0}}, \qquad z_0 = \frac{m_{0,0,1}}{m_{0,0,0}} \tag{6.3}$$

The $m_{i,j,k}$ terms are the moments of the distribution, defined in equation 6.2.

The lightsheet illuminates a cross-section of the tank defined as the xy plane, so the 2d centre of mass of the film is calculated. Although out-of-plane motion is significant after breaking, the net out-of-plane motion should be small, since any resultant force in the z direction is due to asymmetries in the tank or wave paddle, which were designed to be minimal. The centre of mass of the film will therefore be located near to the plane of the middle of the tank, where the light-sheet is situated. Another approximation in the calculation of the centre of mass location is due to the inability to distinguish any concentrations above 0.02%. This biases the position of the centre of mass towards lower concentrations, but is only significant around the breaking event, and not for long term dispersion.

6.6 Fractal Dimension

Prior to breaking, the thickness of the surface film is several orders of magnitude smaller than its length or breadth, and is therefore essentially two-dimensional. After the surface is broken, however, the film mixes downwards and begins to disperse into the third dimension. The camera records a cross-section of the tank, so the film appears to be one-dimensional until breaking when it moves to occupy the two-dimensional plane illuminated by the lightsheet. This transition can be quantified by considering the *fractal dimension* of the film.

The concept of dimension is rather complicated: there are at least 10 distinct definitions of dimension [57], all related yet subtly different. Of these, the topological dimension, D_t is perhaps the most familiar. Defined in terms of homeomorphisms (permitted topological transformations), D_t is the integral measure such that all arcs have $D_t = 1$, all surfaces have $D_t = 2$, and all solid bodies have $D_t = 3$. Many of the other dimensions, and much of Mandlebrot's work on fractals, are based on the *Hausdorff* dimension, D_H, first proposed in 1919. A complete definition of this Hausdorff dimension can be found in *Chaos and Fractals* [57]; an overview is provided in the following section.

The definition of fractal has changed over the years. Mandlebrot, who coined the term, has retracted and replaced his original definition [58]. Now it is generally accepted to refer to a shape whose parts are in some way similar to the whole. It

was observed that the dispersing film patch contained similar features at all visible scales, with smaller vortices developing from larger ones due to the turbulent energy cascade. A fractal analysis was therefore deemed appropriate [59].

Mathematical fractals such as the Koch Curve (see figure 6.2) are exactly self-similar over an infinite range of scales. Many natural phenomena are statistically self-similar over a large but finite range of scales and are better suited to a fractal rather than a Euclidean description. Turbulence itself is statistically self-similar in both the final stage of viscous decay and the large eddy scales [60], and attempts have been made to describe it in terms of fractals [61]. Fractal geometry has also been applied to natural objects such as clouds [62], coastlines [63], the distribution of breaking waves on the ocean surface [64], dispersion of pollution [65], the cracking of concrete [66] and price fluctuations on the stock exchange [67].

6.6.1 Hausdorff Measure and Dimension

The dimension of an object describes the way in which it occupies space, and thus how its size might be quantified.

The size of an object can be measured by counting the number of rulers required to cover it. Consider a 'ruler' of dimension d, and characteristic size r. Its size is then

$$h(r) = \gamma(d) r^d \tag{6.4}$$

where $\gamma(d)$ is defined in terms of the Gamma function:

$$\gamma(d) = \frac{\Gamma(\frac{1}{2})^d}{\Gamma(1 + \frac{d}{2})} \tag{6.5}$$

Using the recursion property of the gamma function, $\Gamma(x+1) = x\Gamma(x)$, and the result that

$$\Gamma(\tfrac{1}{2}) = \sqrt{\pi}$$

$h(r)$ can be calculated for Euclidean values of d:

d	$\gamma(d)$	$h(r)$
0	1	1
1	2	$2r$
2	π	πr^2
3	$\frac{4}{3}\pi$	$\frac{4}{3}\pi r^3$

Table 6.1: Euclidean Rulers

$\gamma(d)$ is thus the measure of a d-dimensional unit ball, and rulers of $d = 1, 2, 3$ have units of length, area and volume respectively.

Hausdorff used this result to define the d-dimensional measure of a set F, $H_d(F)$ in metric space (of which physical objects in real space are a subset):

$$H_d(F) = \lim_{\epsilon \to 0} \inf_{r<\epsilon} \left\{ \sum h(r) : C(r) \right\} \tag{6.6}$$

The $C(r)$ term represents any finite cover of F by rulers of size $r < \epsilon$, and the sum of the ruler measures is simply the total measure of a particular cover. Thus the term in brackets is the set of all measures which cover F. The infimum[1] of this set is the most efficient covering possible. Since the accuracy of measurement increases with decreasing ruler size, the limit as ϵ tends to zero is taken.

As an example, consider the measure of a rectangle of length x and width y. The appropriate measure is clearly the area, xy. The minimum number of circles of radius r required to cover such a rectangle is $\frac{xy}{\pi r^2}$. The 2-dimensional Hausdorff measure is then simply this area:

$$\begin{aligned} H_2(\Box) &= \lim_{r \to 0} \left(\frac{xy}{\pi r^2} \times \pi r^2 \right) \\ &= xy \end{aligned} \tag{6.7}$$

The 1-dimensional Hausdorff measure of the same rectangle can be obtained by replacing the gamma term and changing the exponent of r:

$$H_1(\Box) = \lim_{r \to 0} \left(\frac{xy}{\pi r^2} \times 2r^1 \right)$$

[1] The *infimum* is the unique largest member of the set of lower bounds for some given set e.g. The set $\frac{1}{2}, \frac{1}{4}, \frac{1}{8}...$ has no minimum value but its infimum is zero

$$= \infty \tag{6.8}$$

The 1-dimensional measure, or length, of the rectangle is thus infinite.

Now consider the 3-dimensional Hausdorff measure:

$$\begin{aligned} H_3(\square) &= \lim_{r\to 0}\left(\frac{xy}{\pi r^2}\times\frac{4}{3}\pi r^3\right) \\ &= 0 \end{aligned} \tag{6.9}$$

The 3-dimensional measure, or volume of the rectangle is zero. Using the wrong value of d therefore results in a meaningless value for the measure.

Hausdorff showed that for any given set F, there is a unique value of D_H such that

$$H_d(F) = \begin{cases} \infty & \text{if} \quad d < D_H \\ 0 & \text{if} \quad d > D_H \end{cases} \tag{6.10}$$

D_H is known as the Hausdorff dimension, and provides a measure of an object that is independent of the resolution of the measurement, ϵ. The d-dimensional Hausdorff measure of an object is only useful if d is equal to the Hausdorff dimension of that object. Significantly, there is no restriction that D_H must be an

integer. A set is termed *fractal* if its Hausdorff dimension is not an integer.

6.6.2 Box Counting Dimension

Though elegant, the Hausdorff measure and dimension are difficult to calculate in practice. Furthermore, the boundary between film and water is recorded in a two dimensional image made up of finite pixels. Since the Hausdorff dimension requires taking the limit of ruler size to zero, any curve or shape in an image will have a Hausdorff dimension of 2. This is not particularly informative, so an alternative definition of fractal dimension is used.

Firstly, it is computationally easier to use a square ruler rather than a circular one. This distinction is not significant in the limit of small rulers. By using a square ruler, $\gamma(d)$ can be removed from equation 6.4 since a square whose side is of unit length also has unit area. Secondly, the smallest practical ruler size is a single pixel because, as mentioned above, the use of smaller rulers will lead to a dimension of 2. Thus the limit to zero in equation 6.6 is being neglected. Finally, determining the optimal arrangement of rulers is extremely complex. For this reason, a single arrangement of rulers is used to measure the coverage, and this measure is assumed to be satisfactory. We are therefore ignoring the infimum in equation 6.6. Together, these two assumptions are equivalent to replacing the Hausdorff measure of an object by a simplified measure H, defined as

$$H = Nr^d \tag{6.11}$$

As before, N is the number of rulers of size r which intersect the object.

Taking the logarithm of both sides of equation 6.11 and rearranging leads to

$$\log N = d \log \left(\frac{1}{r}\right) + \log H \tag{6.12}$$

This is the equation of a straight line of gradient d and intercept $\log H$, and provides a way of calculating both the fractal dimension and the measure.

Equation 6.12 suggests that if a graph of $\log N$ versus $\log \left(\frac{1}{r}\right)$ is plotted, the gradient is equal to the fractal dimension. In other words, it is necessary to measure the size of the object as a function of ruler size.

This can be done using the technique of *box counting*. A grid of squares of spacing r is superimposed onto the object, and the number of squares, $N(r)$, overlapping a portion of the object is counted. This step is repeated for different sizes of r.

Figure 6.1 demonstrates how the box counting technique can be used to calculate the dimension of a shape. For the point, the size of the box is irrelevant: one box is always sufficient to cover the point. The power law relating ruler size to number required is $Nr^0 = 1 = H$, so the dimension of a point is zero.

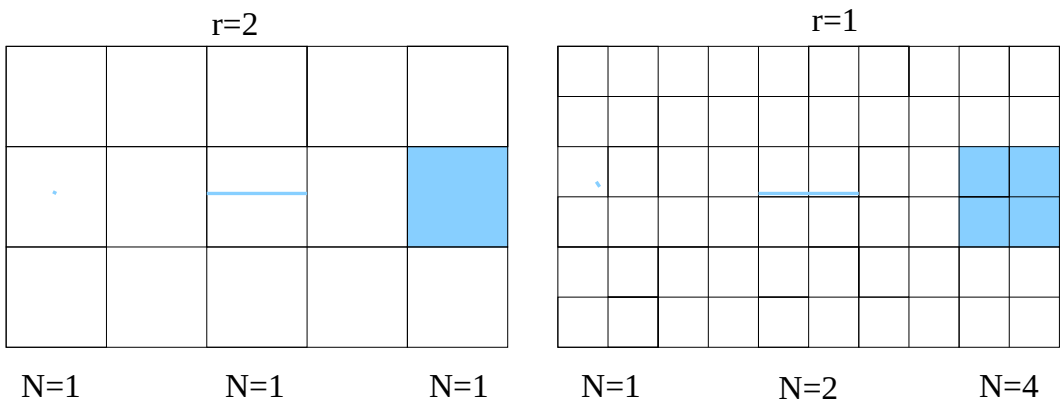

Figure 6.1: Box Counting Method

Halving the grid size doubles the number of boxes required to cover the line, so the power law becomes $Nr^1 = 2 = H$. The dimension of the line is therefore one.

While a single box of size $r = 2$ is sufficient to cover the square, four boxes of size $r = 1$ are necessary. The power law for the square is $Nr^2 = 4 = H$, and its dimension is two.

The above examples are somewhat contrived since the grid spaces are optimally lined up with the objects to be measured i.e. this is the infimum of all possible grid superpositions. If the grids above were simply laid at random over the shapes, as many as 6 $r = 2$ boxes or 12 $r = 1$ boxes could be required to cover the square, which would lead to an unrealistic value for the dimension. The effect of ruler size on N was investigated further by measuring a Koch curve.

The Koch curve is generated by replacing every line by the Koch line segment; the original segment and first five iterations are shown in figure 6.2.

The length of the Koch curve after n iterations is $\frac{4}{3}$ greater than its length after $n-1$ iterations. If the ruler length r used to measure the curve is reduced by a factor of 3, the number required to cover it increases by a factor of 4. The fractal dimension of the Koch curve is therefore $\frac{\log 4}{\log 3} \approx 1.26$. The length of the Koch curve is infinite, while its area is zero. Thus the fractal dimension is a more useful measure of the Koch curve, and fractal objects in general, than length and area.

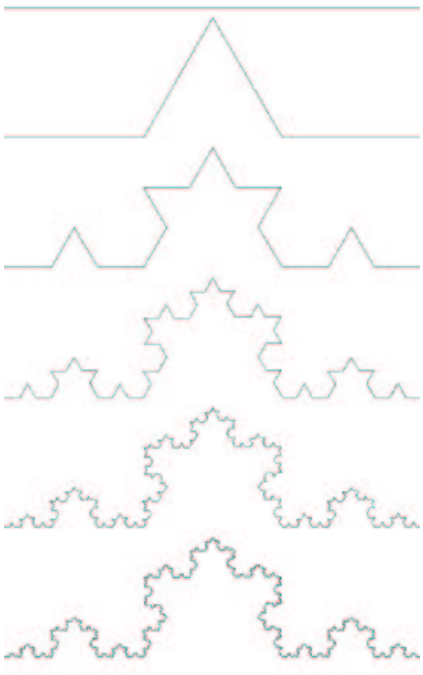

Figure 6.2: First Five Iterations of the Koch Curve

A graph of $\log N$ against $\log \frac{1}{r}$ is shown in figure 6.3, for 5th iteration Koch curves with an original segment length of 2500 pixels, and line widths of 1,5,10 and 20. Ruler sizes from 1 to 5000 were used. For small ruler size, the gradient of the graph is approximately unity for the Koch curve with a line width of one; this gradient increases with increasing line width, tending towards two. At very large ruler sizes, the Koch curve is effectively a point, and the gradient of the graph is zero. As the ruler size approaches the height of the

Koch curve ($\frac{\sqrt{3}}{2} \times \frac{width}{4}$, or approximately 540 pixels), sudden jumps begin to appear in the graph. These correspond to the effects of using a fixed grid of rulers, rather than searching for the infimum. To calculate the fractal dimension of the Koch curve accurately, the portion of the graph where the gradient is approximately constant should be measured.

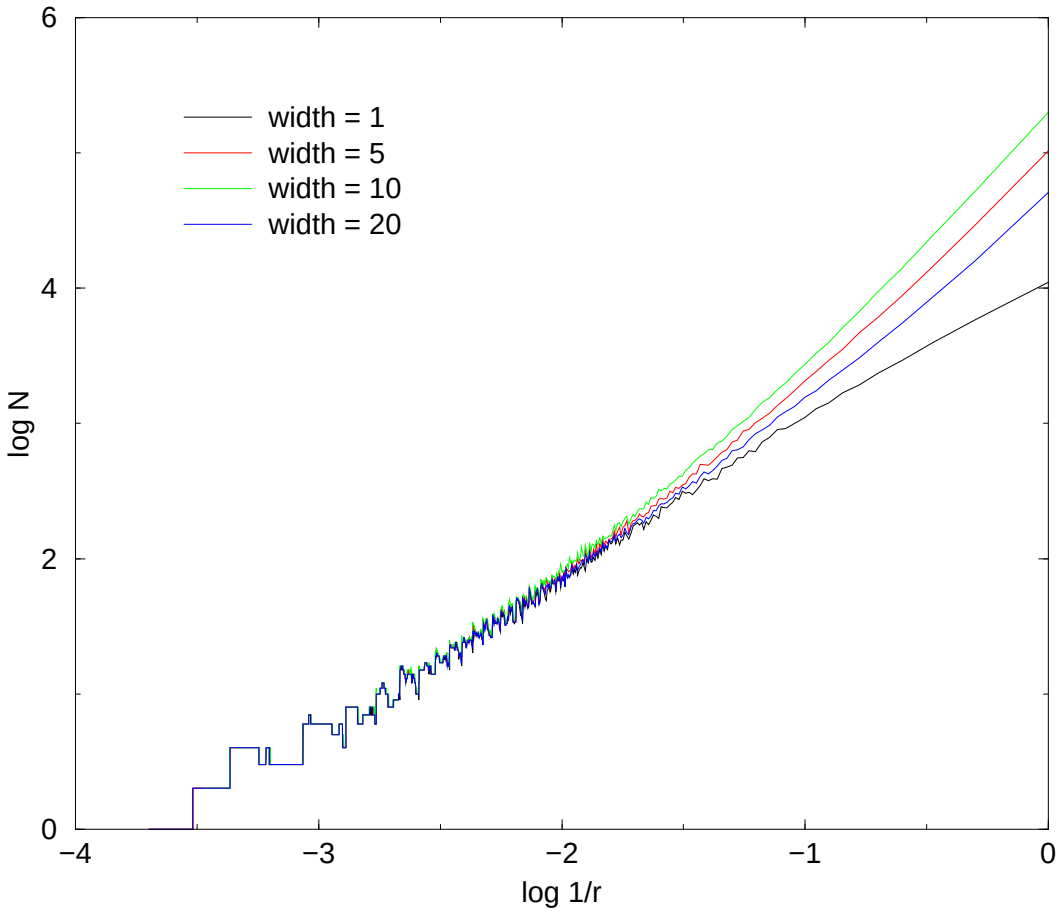

Figure 6.3: Graph to determine Fractal Dimension of Koch curve

From inspection, the graph is approximately uniform between $x = -2.5$ and $x = -1$, corresponding to a range of ruler size from 10 to 320. The gradient of

the graph was obtained using linear regression, which involves fitting a line of the form $y = mx + c$ to the data. If there are N points and the method of least squares is used [68], the coefficients m and c are

$$m = \frac{\sum_i^N (x_i - \bar{x})(y_i - \bar{y})}{\sum_i^N (x_i - \bar{x})^2} \pm \sqrt{\frac{\sum_i^N (y_i - \bar{y})^2 - m \sum_i^N (x_i - \bar{x})(y_i - \bar{y})}{(n-2) \sum_i^N (x_i - \bar{x})^2}} \quad (6.13)$$

$$c = \bar{y} - m\bar{x} \pm \frac{\sum_i^N (y_i - (mx_i + c))^2 \sum_i^N x_i^2}{n(n-1) \sum_i^N (x_i - \bar{x})^2} \quad (6.14)$$

The gradient of the Koch curve of unit line width in the region specified above is then 1.226 ± 0.007, slightly less than the Hausdorff dimension of the infinite Koch curve. This might be expected, since it is only the fifth iteration Koch curve which is being measured.

To emphasise again, the Hausdorff dimension of the Koch curve obtained after a finite number of iterations is unity, and equal to 1.26 for the infinite Koch curve. The infinite Koch curve is topologically equivalent to a line, so its topological dimension, D_t, is also 1. The box-counting dimension can exceed one for a finite iteration Koch curve, but is never greater than the dimension of the space in which the shape is embedded, in this case a 2d plane.

The relationship between the topological, Hausdorff and box-counting dimensions is:

$$D_t \leq D_H \leq D_{bc} \tag{6.15}$$

For accurate values of d, the maximum ruler size should be smaller than the overall size of the object, so the effect of neglecting the infimum is less significant. The minimum ruler size should be comparable with the smallest-scale detail in the image. The accuracy is also improved by using a number of ruler sizes, rather than just two.

6.7 Dispersion

All of the quantitative analysis of the film mixing described in this thesis is Eulerian, meaning that the flow features are measured with respect to a fixed frame of reference, namely the field of view of the cameras. The actual trajectory of an individual fluid element, however, is best described in terms of a Lagrangian frame of reference, that is relative to another fluid element. In practice it is not easy to relate Lagrangian motion to the Eulerian velocity field [69].

Dispersion occurs because the Lagrangian paths followed by different fluid elements, initially close together, will tend to diverge in a spatially and/or temporally varying velocity field.

This section describes some of the mechanisms which contribute to the dis-

persion of the surface film after breaking.

6.7.1 Molecular Diffusion

The transfer of heat from hot to cold bodies can be explained either macroscopically, by a flow of energy down a temperature gradient, or microscopically, in terms of collisions which transfer kinetic energy from fast-moving to slow-moving molecules. Thermal processes are also responsible for the spreading of one mobile material within another; such spreading is termed *diffusion* and can be described mathematically using either concentration gradients or the random walks of fluid particles.

Fick's equation [70] states that the mass flux $\mathbf{q}$ of a diffusing material is proportional to the concentration gradient in that direction. Mathematically,

$$\mathbf{q} = -\mathbf{D}\nabla\mathbf{C} \tag{6.16}$$

where D is the diffusion coefficient and C is the concentration. Combining this result with the conservation of mass leads to the diffusion equation

$$\frac{\partial C}{\partial t} = -D\nabla^2 C \tag{6.17}$$

The solution of this differential equation in one dimension is

$$C(x,t) = \frac{M}{\sqrt{4\pi Dt}} e^{\frac{-x^2}{4Dt}} \tag{6.18}$$

where M is the total mass of the diffusing solute. Equation 6.18 can also be derived by combining a random walk motion with the central limit theorem and considering the probability distribution of a large number of particles.

If the edge of a diffusing patch is defined as the point at which the concentration falls below to $\frac{1}{e^2}$, its size, expressed in terms of the standard deviation, σ, as a function of time t is given by

$$\sigma = \sqrt{2Dt} \tag{6.19}$$

This result applies to Brownian motion, where the movement of each particle is random and not dependent on its previous motion.

6.7.2 Advection

If there is a steady mean flow, u, the diffusion described above is accompanied by a net transport of the pollutant in a process known as *advection*. The mass transport equation (6.16) now contains an additional advection term:

$$\mathbf{q} = \mathbf{uC} - \mathbf{D}\nabla\mathbf{C} \tag{6.20}$$

and the diffusion equation becomes

$$\frac{\partial C}{\partial t} + \mathbf{u}.\nabla\mathbf{C} = -\mathbf{D}\nabla^{\mathbf{2}}\mathbf{C} \tag{6.21}$$

If there is a velocity gradient, or shear, present in the flow, the differential advection causes an enhanced rate of spreading called *dispersion*. In many cases, u is a function of both space and time and equation 6.21 becomes impossible to solve analytically. Numerical models are then required to predict the resulting dispersion. The rate of mixing in a changing velocity field is considerably faster than the spreading caused by molecular diffusion. Indeed, in many practical situations, molecular diffusion can essentially be neglected and the dispersion is then due to fluid motion rather than thermal effects.

6.7.3 Turbulent Diffusion

Turbulence is a very effective mechanism for increasing the rate of mixing. Due to the complexity involved in quantifying turbulence, most mathematical descriptions of *turbulent diffusion*, as it is known, assume that the turbulence is homogeneous and isotropic, with no mean flow.

Taylor [71] showed that in such turbulence, the mean square displacement of a fluid particle from its original position at time $t = 0$, is proportional to t^2 for small t, and to t for large times. If it is assumed that diffusion is an additive

process, a patch can be thought of as a series of particles, and the variance of the patch increases as t. Equivalently, the standard deviation of the patch increases as $\sqrt{t}$. This is the same result as obtained when considering molecular diffusion, but the constant of proportionality, the diffusion coefficient, is considerably larger in turbulence. Thus the spreading of one fluid within another in homogeneous, isotropic turbulence can be described as if its motion were governed by a random walk for large t.

At intermediate time scales, the expansion of cloud is governed by Richardson diffusion [70]. Richardson considered the separation of particle pairs and his law states that the diffusion coefficient D varies as the size of the cloud, σ, as [72]

$$D \propto \sigma^{\frac{4}{3}} \tag{6.22}$$

That is, the diffusion coefficient is not a constant in this region, and a cloud of pollutant expands increasingly rapidly as it grows.

6.7.4 Fractional Brownian Motion

Measurements of fluid markers at sea have indicated that the drifter trajectories are fractal curves over a range of scales. Osborne et al. [33] measured the fractal dimension of drifters to be 1.27 ± 0.06 for scales between $20km$ to $150km$ in the Kuroshio extension, while Sanderson et al. [32] found trajecto-

ries of dimension 1.3 ± 0.1 for scales between $10m$ and $4000m$ in the NorthEast Atlantic. Addison [65] has modelled such dispersion using *fractional Brownian Motion*. This generalises Brownian motion by introducing the *Hurst Exponent*, H:

$$\sigma = (2Dt)^H \tag{6.23}$$

Equation 6.23 reduces to normal Brownian motion if the Hurst exponent equals $\frac{1}{2}$. Brownian motion corresponds to random walk motion, so each step is independent of all others. For values of H other than 0.5, however, there is effectively a correlation between where the particle moves next to where it has moved already. The range where $0 < H < 0.5$ is termed subdiffusive, or antipersistent, and the correlation is negative i.e. movement in one direction tends to be followed by movement in the *opposite* direction. If $0.5 < H < 1$, the process is called superdiffusive, or persistent and the correlation is positive: movement in one direction tends to be followed by movement in the *same* direction.

The Hurst exponent is related to the fractal dimension of the particle's motion. When $H < 0.5$, a fluid particle will tend to turn back on itself and its trajectory will densely fill the plane in which it is embedded; thus its fractal dimension will be large. On the other hand, if $H > 0.5$, the particle's trajectory will tend to continue in its original direction, and will therefore resemble a $1D$ line.

Mathematically, the spatial trajectory of a fluid particle has a fractal dimension $\delta_{spatial}$ of

$$\delta_{spatial} = \min\left[\frac{1}{H}, 2\right] \tag{6.24}$$

where *min* denotes the minimum of the two terms within brackets. H is also related to the fractal dimension of the particle's trace (displacement from origin), δ_{trace}, as a function of time

$$\delta_{trace} = 2 - H \tag{6.25}$$

The simplified representation of the diffusion of a polluting particle for three different values of H, 0.25, 0.5 and 0.75, is simulated in figure 6.4. The correlation coefficient which determines whether the particle is more likely to continue in the direction it is already moving or change direction is proportional to $H - 0.5$. Both the time trace (distance from starting point as a function of time) and the trajectory (x and y positions) are shown.

When $H = 0.25$, the time trace and trajectory are more jagged than the normal random walk example ($H = 0.5$). The corresponding fractal dimensions are therefore relatively high, but the area over which the diffusion occurs is rather small. Conversely, when $H = 0.75$, the trace and trajectory are smoother than

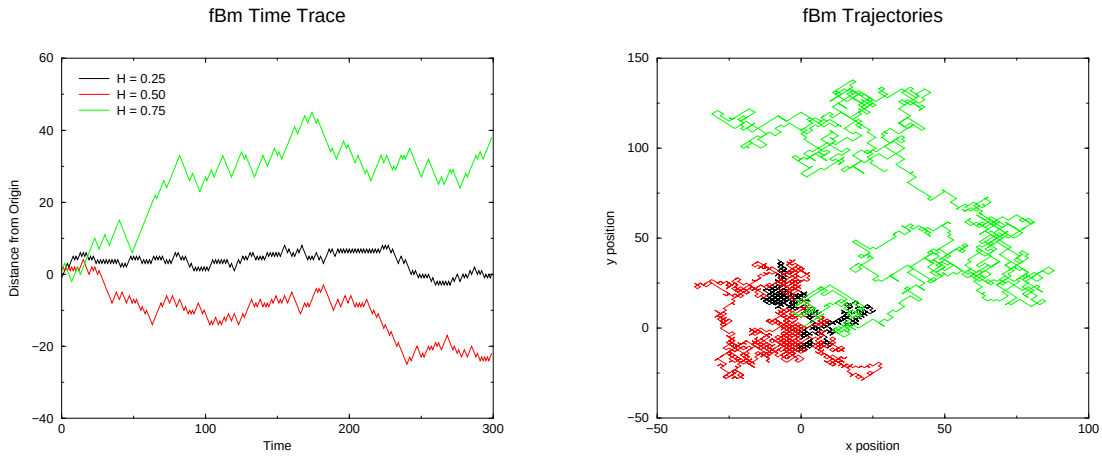

Figure 6.4: Trace and Trajectory of Fractional Brownian Motion

when $H = 0.5$ so fractal dimensions are smaller. In general, if $H > 0.5$, the diffusing particle tends to travel further from its starting point than a random walk. Osborne et al. [33] and Sanderson et al. [32] found values of 0.79 ± 0.04 and 0.77 ± 0.06 respectively for the Hurst Exponent in the diffusion of drifters in their experiments. This indicates that horizontal diffusion is persistent in the ocean.

6.7.5 Quantifying the Dispersion

There are a number of mechanisms responsible for the mixing of a contaminant within a moving body of water, such as molecular and turbulent diffusion, advection and shear flow dispersion. In practice, it is extremely difficult to separate the effect of each flow feature [29]. Sometimes, the overall dispersion can be

modelled using fractional Brownian motion.

For the purposes of quantifying the film mixing in these experiments, a dispersion exponent H and coefficient D were calculated. Taking the logarithm of each side of equation 6.23 leads to

$$\log \sigma = H \log t + H \log(2D) \tag{6.26}$$

H and D can be thus be determined by plotting $\log \sigma$ against $\log t$. The gradient of the slope is then H, and D is equal to $\frac{10^{\frac{c}{H}}}{2}$, where c is the intercept.

The variance of a concentration distribution is defined as the ratio of the 2^{nd} order moment to the $zero^{th}$ order moment and can therefore be calculated using equations 6.1 and 6.2.

It should be noted that H is a dispersion exponent rather than the Hurst exponent, since it is not clear that the film dispersion can be represented by fractional Brownian motion.

Dispersion coefficients and exponents were also calculated to quantify the increasing depth reached and area covered by the film. This allowed a direct comparison with some similar experiments to be carried out, as will be discussed in section 7.6.

6.8 Velocity Distribution

The images of the film dispersion can be cross-correlated as though they were PIV images. Instead of tracer particles, the mean displacement is determined by matching the boundaries between concentration bands.

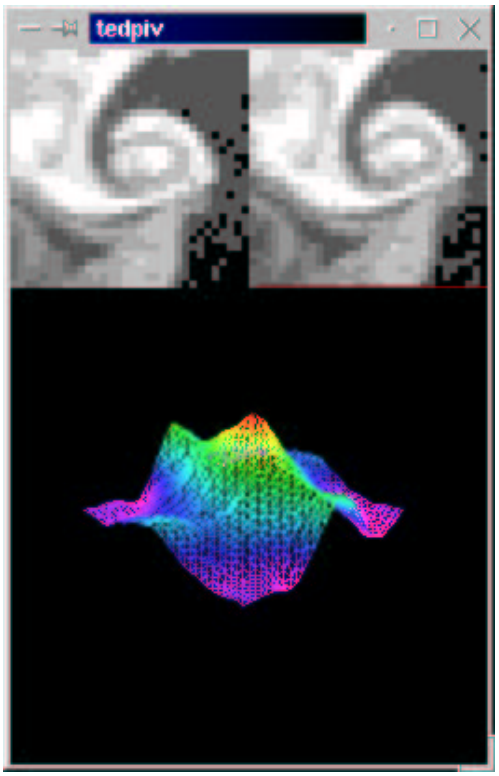

Figure 6.5: LIF Interrogation Areas and Correlation Plane

Because the interrogation areas consist of regions of a particular grey level rather than individual particles, the correlation plane contains ridges rather than sharp peaks; see figure 6.5. The peak detection algorithm, which assumes the peaks are gaussian, is therefore less reliable, so it is not anticipated that the accuracy of optimised PIV, where the error in the displacement can be as low as 0.05 pixels, will be matched.

Nevertheless, the vectors obtained from the analysis appeared reasonable, and permit the calculation of flow properties such as vorticity and kinetic energy.

Chapter 7

LIF Results

7.1 Introduction

In the top right corner of each page in this thesis, there is a picture of the mixing of a surface film after breaking, taken at $0.15s$ intervals. The images are colour-coded such that red corresponds to low concentration, and purple to high concentrations. In this chapter, the parameters described in the previous chapter are quantified for this experiment, which involved a wave with a non-dimensional amplitude of $ak = 0.324$. The repeatability of mixing and the effect of wave amplitude on dispersion are also considered, in sections 7.4 and 7.5 respectively. Finally, the results obtained from these experiments are compared to similar work in section 7.6. These experiments were carried out in conjunction with Alistair Arnott.

Before the information extracted from experiments is presented, a qualitative description of post-breaking dispersion is provided.

7.2 Qualitative Description of Mixing

The film remains on the surface prior to breaking, despite the passing of waves of significant amplitude. In the case of plunging breakers, dispersion begins when the overturning tip breaks the surface, which forces the film downwards into the main body of the water. The subsequent passing of wave crests and troughs stretches the film horizontally and pushes it downwards. The shearing impact of the plunging tip creates a large scale eddy which carries the film downwards and forwards, rotating as it moves. It also produces a significant splash-up, which creates a secondary patch of film downstream from the first. Both patches continue mixing downwards, carried by the evolving turbulence, and becoming increasingly contorted as energy cascades from large to small vortices. After a few seconds, isolated patches appear in the images which correspond to portions of the dispersing film being carried into the lightsheet by the out-of-plane motion created by the breaking event.

For spilling breakers, the dispersion is caused by water tumbling down the front face of the wave and disturbing the surface. Spilling is less violent than plunging, and occurs over longer time periods, so the dispersion patch does not

reach as deep as in plunging. Because the splash-up is less, the formation of distinct patches is less obvious than after plunging.

7.3 Analysis of $ak = 0.324$ breaker

Here, a quantitative description of the dispersion following a breaking wave of non-dimensional amplitude $ak = 0.324$ is given. The central frequency of the wave packet is $f_c = 0.88$Hz and the frequency spread is $\Delta f = 0.6424$Hz.

7.3.1 Maximum Depth Reached by Film

The maximum depth reached by the film was calculated for each image and each concentration. A graph of non-dimensionalised depth against time for 4 different concentrations is shown in figure 7.1. Time is counted from the instant at which the wavemaker was programmed to produce a breaking event and non-dimensionalised by multiplication with the angular frequency. Because the cameras were not positioned to view actual breaking (since no dispersion occurs directly below the break point), nothing significant occurs in the graph until around $0.3s$ after breaking. Distance is measured from the mean water level, and non-dimensionalised with respect to the central wavenumber.

There are a number of points to note about the graph in figure 7.1. The apparently large separation between the different concentrations around breaking is

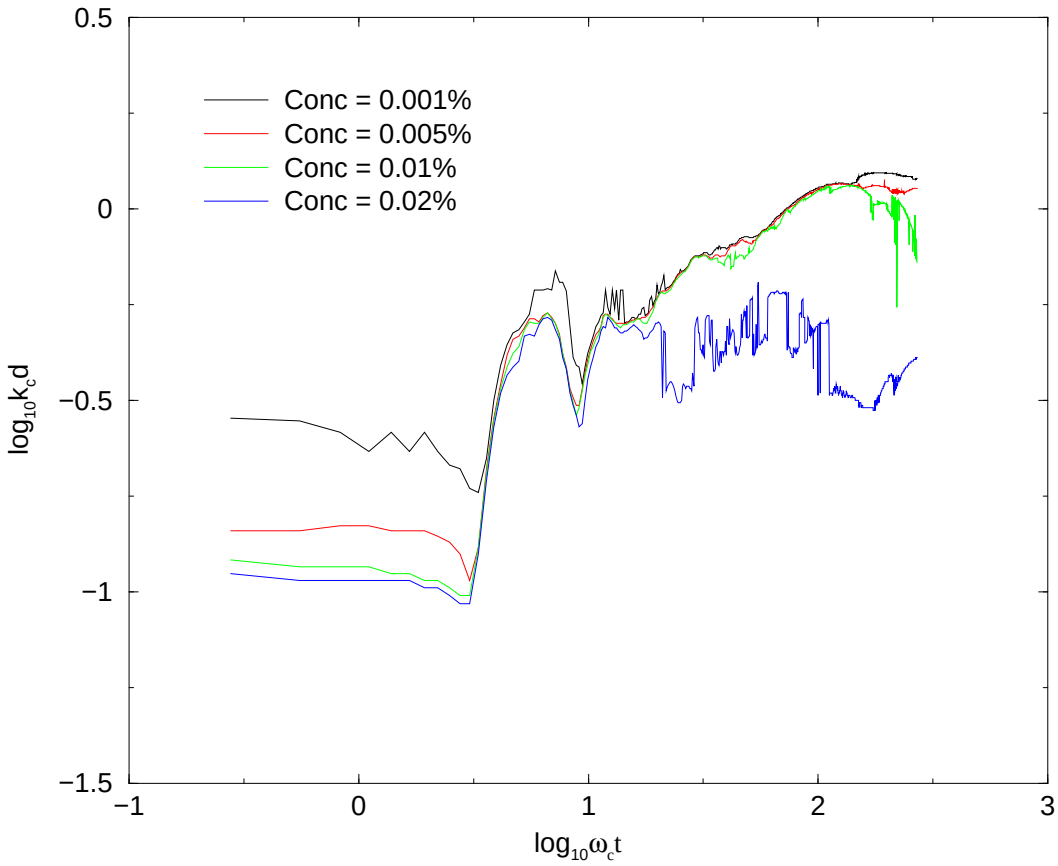

Figure 7.1: Graph of Depth Reached against Time

somewhat misleading, and is mainly due to an artefact of the logarithm function[1]. As the first trough passes in front of the cameras, the film is carried downwards relative to the MWL, and the subsequent crests and troughs, of rapidly diminishing amplitude, cause a degree of oscillation in the depth recorded. A few seconds after breaking, however, the surface disturbance has died away, and the mixing is then primarily due to eddy motion and the evolving turbulence.

[1]The derivative of the function $y = \log x$ is $\frac{dy}{dx} = \frac{1}{x}$, so the logarithms of two similar but small ($<< 1$) quantities are significantly different.

Lower concentrations reach a greater depth than higher concentrations. This is to be expected since, in addition to eddy diffusivity, the film concentration will naturally approach a dilute equilibrium due to molecular diffusion. Indeed, while the lowest concentrations continue to mix downwards for the duration of the experiment, the highest concentrations barely exceed one wave amplitude below the surface.

The sudden steps in the different graphs correspond to patches of rhodamine entering or leaving the lightsheet. That the higher concentrations have larger and more frequent jumps suggests that the out-of-plane motion is stronger at the surface. This can be seen by inspecting a graph of the x position (the distance downstream from the breaking point) at which the maximum depth occurs, as a function of time (figure 7.2).

The value $x = 0$ corresponds to the left hand side of the image. Both curves are tending upwards, corresponding to the film dispersing downstream. It is clear that there are more abrupt changes in the higher concentration band, due to its proximity to the surface. An interesting feature of figure 7.2 is that the lower band jumps up suddenly, then slowly decreases. This is thought to be due to the anti-clockwise rotation of the large scale eddies responsible for mixing the film.

In the region $1.15 < \log_{10} \omega_c t < 2.15$, corresponding to a time of 2.5 to 25 seconds after breaking, the graph of $\log k_c d$ against $\log \omega_c t$ increases approximately linearly. The gradient of this line is approximately 0.36, and the intercept

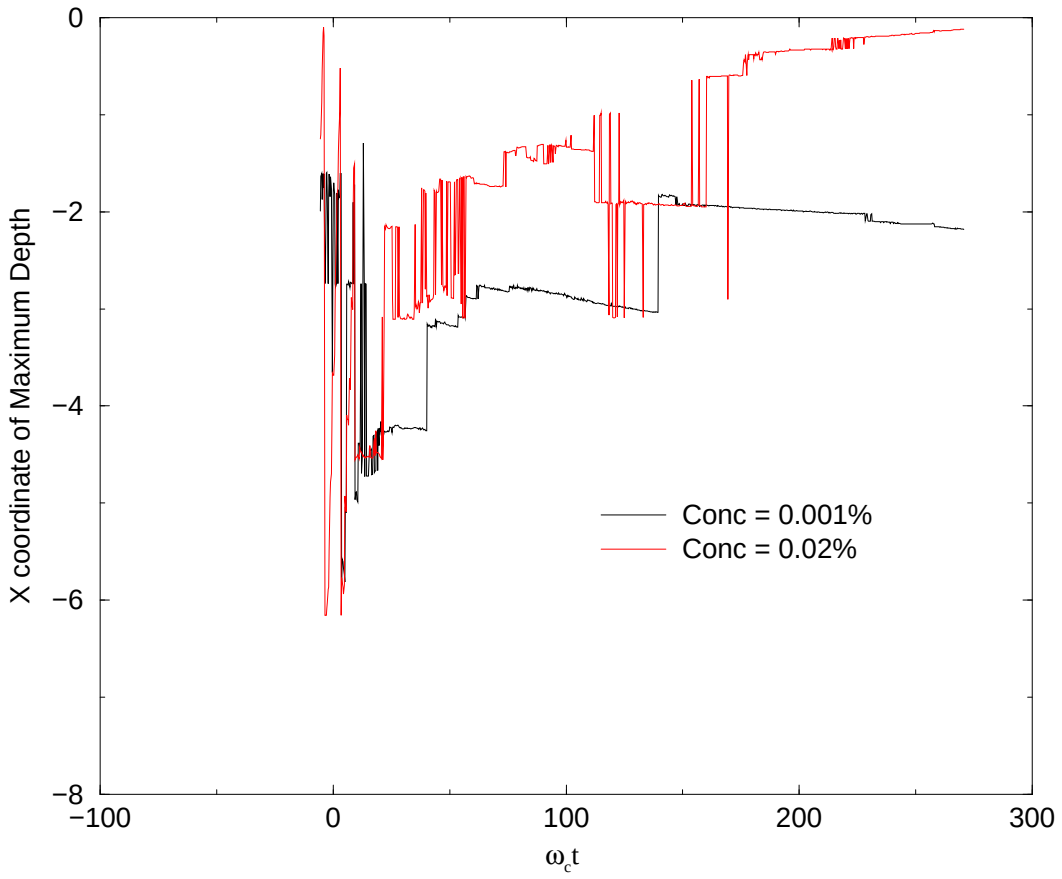

Figure 7.2: Graph of 'X' Coordinate of Deepest Position against Time

is -0.68, leading to a dispersion coefficient D equal to 0.0065. In this region, therefore, the depth reached by the film, d is related to the time since breaking by

$$k_c d = (2 \times 0.0065 \times \omega_c t)^{0.36} \tag{7.1}$$

After this generally steady increase in depth, the film has largely moved out-with the lightsheet, and has reached a depth of around 4 wave amplitudes.

7.3.2 Area Covered by Film

For each concentration band and image, the area covered by the film material was measured by counting the number of pixels above the appropriate grey level. The area for four different concentrations is shown in figure 7.3.

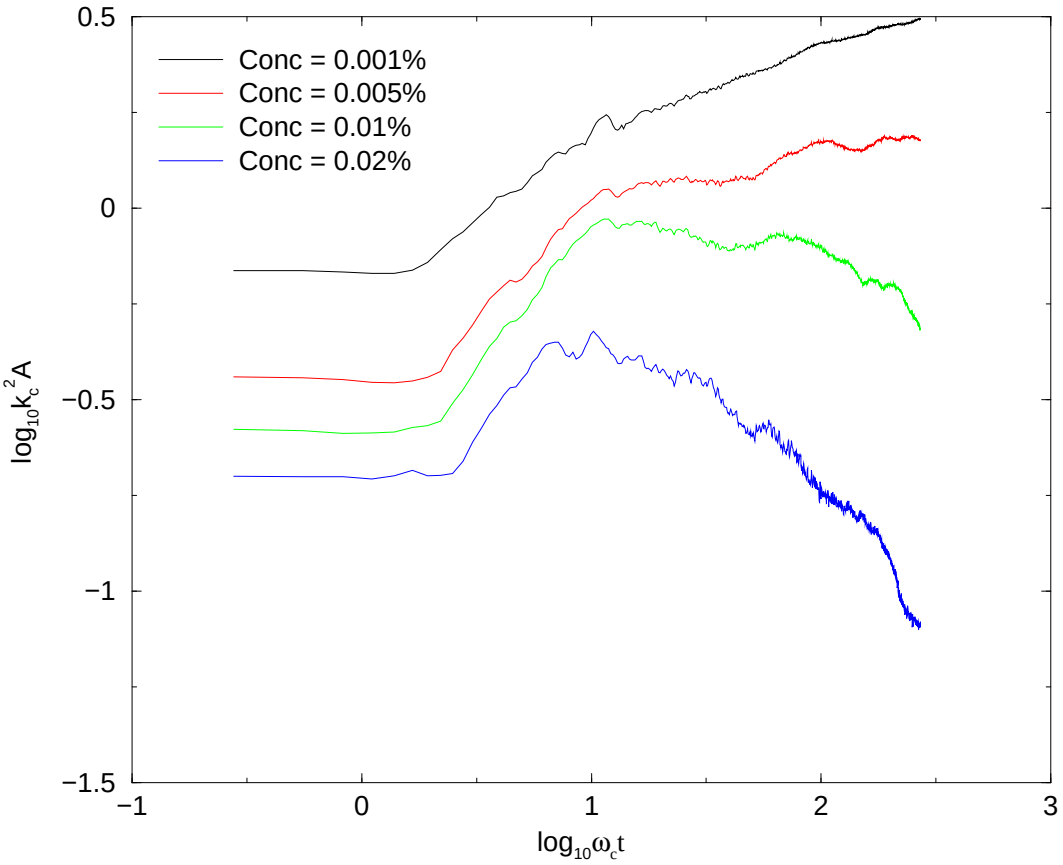

Figure 7.3: Graph of Area against Time

The curves representing each of the four stock concentrations rise immediately after breaking. Around $1s$ later, the area of the highest concentration begins to drop as the film dilutes. As in the graph of depth reached against time,

the graph of the lowest concentration increases approximately linearly between $\log_{10}\omega t = 1.15$ and $\log_{10}\omega t = 2.15$. Using linear regression, the gradient of the curve in this region is 0.23, and the dispersion coefficient is 0.34. That is, the area of the patch A is growing with time as

$$k_c^2 A = (2 \times 0.34 \times \omega_c t)^{0.23} \tag{7.2}$$

7.3.3 Centre of Mass Motion

The location of the centre of mass of the film in each image was calculated using equation 6.3 and is represented in figure 7.4. The black rectangle in the upper image corresponds to the field of view of the camera combination. The coloured points represent the location of the centre of mass; red corresponds to times soon after breaking, and increasing time is represented by a transition through the colour spectrum towards purple. The lower image is enlarged, and is labelled with specific times relative to breaking.

Initially, the centre-of-mass of the film is approximately in the middle of the widescreen image, at the water surface. About 0.3 seconds after breaking, the splash-up appears at the right hand side of the image and the centre-of-mass moves towards the right. The motion of the centre-of-mass is then dominated by passing crests and troughs until about $4s$ after breaking. At this time, the non-

Figure 7.4: Motion of Centre of Mass

dimensional velocity, $\frac{vk}{\omega}$, where v is the actual velocity, is approximately 0.04. A graph of velocity against time is shown in figure 7.5.

Over the next $30s$, this mean velocity slowly decreases, at an average non-dimensional gradient of -0.0001. At the end of the experiment, the velocity of the centre-of-mass is 0.01, or 1% of the wave velocity prior before breaking. The direction of motion of the centre-of-mass is 8.5^o below the horizontal.

7.3.4 Dispersion of the Film

The vertical and horizontal components of the dispersion were considered separately, which involved calculating the vertical and horizontal standard deviations

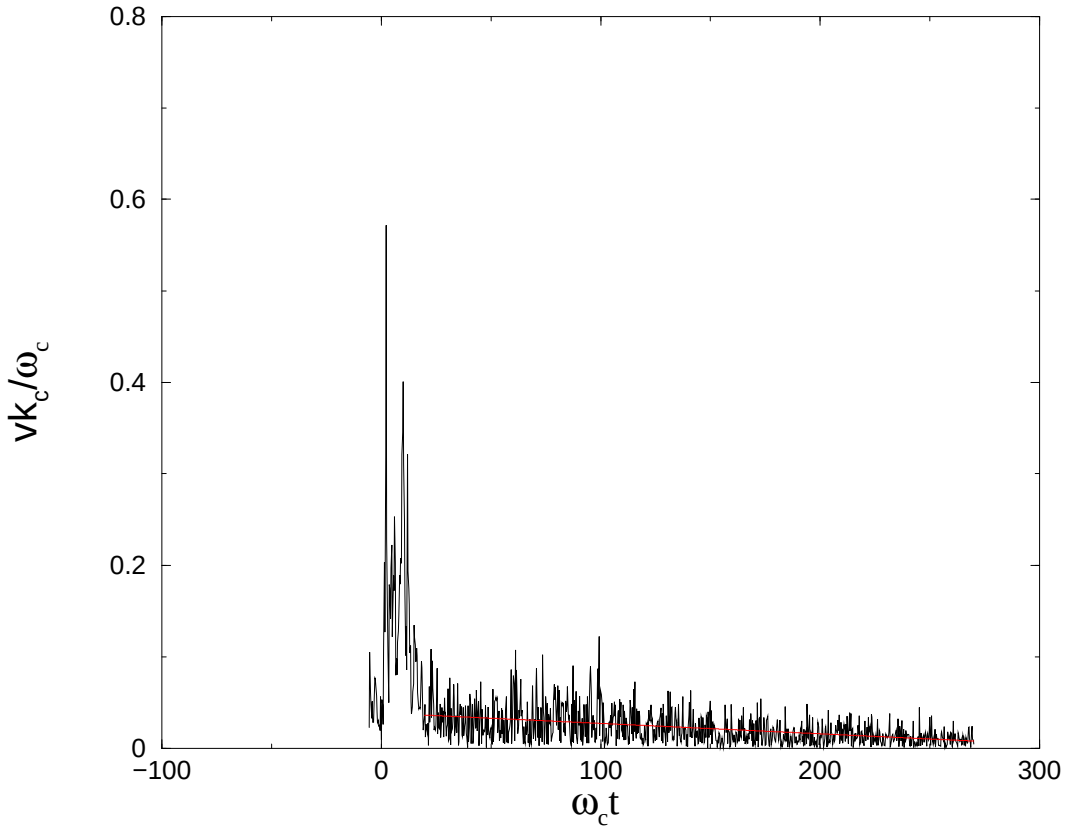

Figure 7.5: Graph of Velocity against Time

of the patch distribution. This was done by taking the square root of the variance (2^{nd} order moment), calculated using equation 6.2. The logarithm of the non-dimensionalised standard deviation for each image was then plotted against the logarithm of the non-dimensionalised time, as shown in figure 7.6.

The graph at the left of figure 7.6 represents the vertical growth of the film patch with time, while the right graph shows its horizontal growth. The graphs are quite different: initially the vertical standard deviation, σ_y, is small since the film is confined to the surface, while the horizontal standard deviation, σ_x, is large

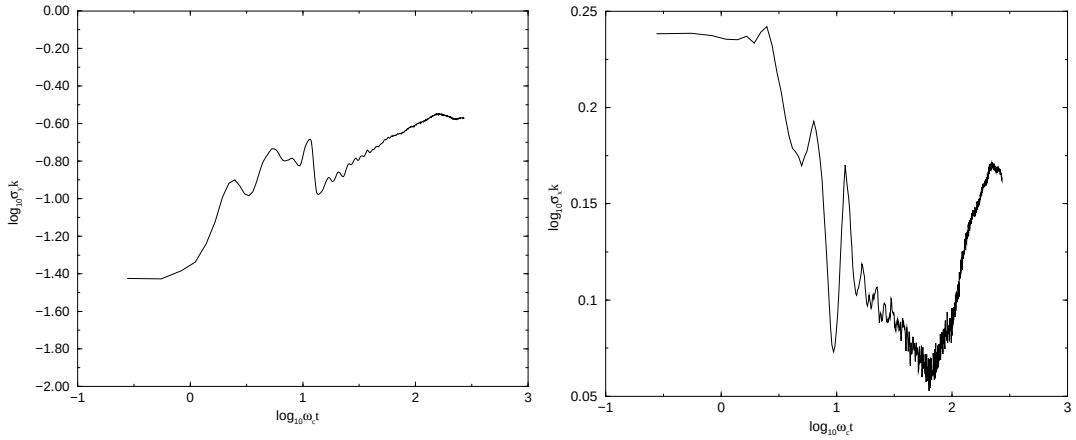

Figure 7.6: Graph of Vertical (left) and Horizontal (right) Standard Deviation against Time

because the film extends along the full width of the field of view of the cameras. After breaking, σ_x reduces as more contaminant is concentrated near the centre of the image. The horizontal size of the patch reaches a minimum around $10s$ after breaking and then begins to increase linearly for the next $30s$. After this point, σ_x decreases once again, as the film disperses outwith the lightsheet. The gradient of the line in the linear region is 0.22.

As might be expected, the vertical size of the patch is initially influenced by the passing crests and troughs. As in the case of the graphs of depth and area against time, however, the graph is approximately linear between $\log_{10}\omega t = 1.15$ and $\log_{10}\omega t = 2.15$. The gradient of this line is 0.37. By measuring the intercept of the straight lines in these graphs, expressions for horizontal and vertical diffusion coefficients can be calculated to relate the increase of each standard deviation to time:

$$k_c\sigma_x = (2 \times (1.3 \times 10^{-2}) \times \omega t)^{0.22} \qquad (10s < t < 30s)$$
$$k_c\sigma_y = (2 \times (1.1 \times 10^{-4}) \times \omega t)^{0.37} \qquad (2.5s < t < 25s) \tag{7.3}$$

The horizontal diffusion coefficient is therefore approximately 100 times the vertical diffusion coefficient, but the horizontal dispersion exponent is less than its vertical counterpart.

7.3.5 Fractal Dimension of Film-Water Boundary

The fractal dimension of the boundary between the rhodamine patch and the water was calculated. First the image was thresholded to remove any background light. All grey levels below the cut-off were set to black; all grey levels above the cut-off were set to white. This image was then edge-detected to obtain the outline of the patch. These procedures are illustrated in the images shown in figure 7.7.

All integer ruler sizes between unity and the vertical variance were used to calculate the fractal dimension. For images some time after breaking, this often involved using over 50 different ruler sizes. By using a large number of ruler sizes, the effects of offsets, caused by neglecting to obtain the optimum coverage, and of finite pixel size, which results in a slight overturning in the curve at the smallest ruler sizes, do not significantly affect the best-fit gradient and hence the value obtained for the fractal dimension. A graph of the logarithm of the number

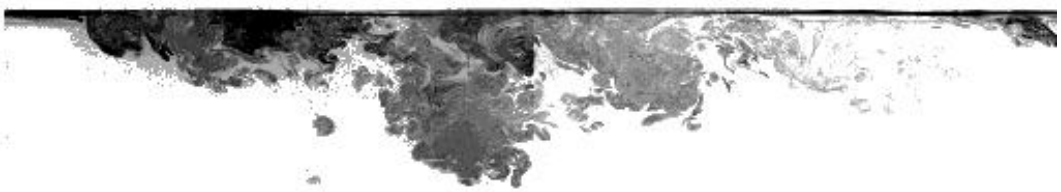

Original Image

Thresholded Image

Edge Detected Image

Figure 7.7: Image Processing prior to Fractal Dimension Calculation

of rulers of size r required to cover the film outline from figure 7.7 against the logarithm of $\frac{1}{r}$ is shown in figure 7.8.

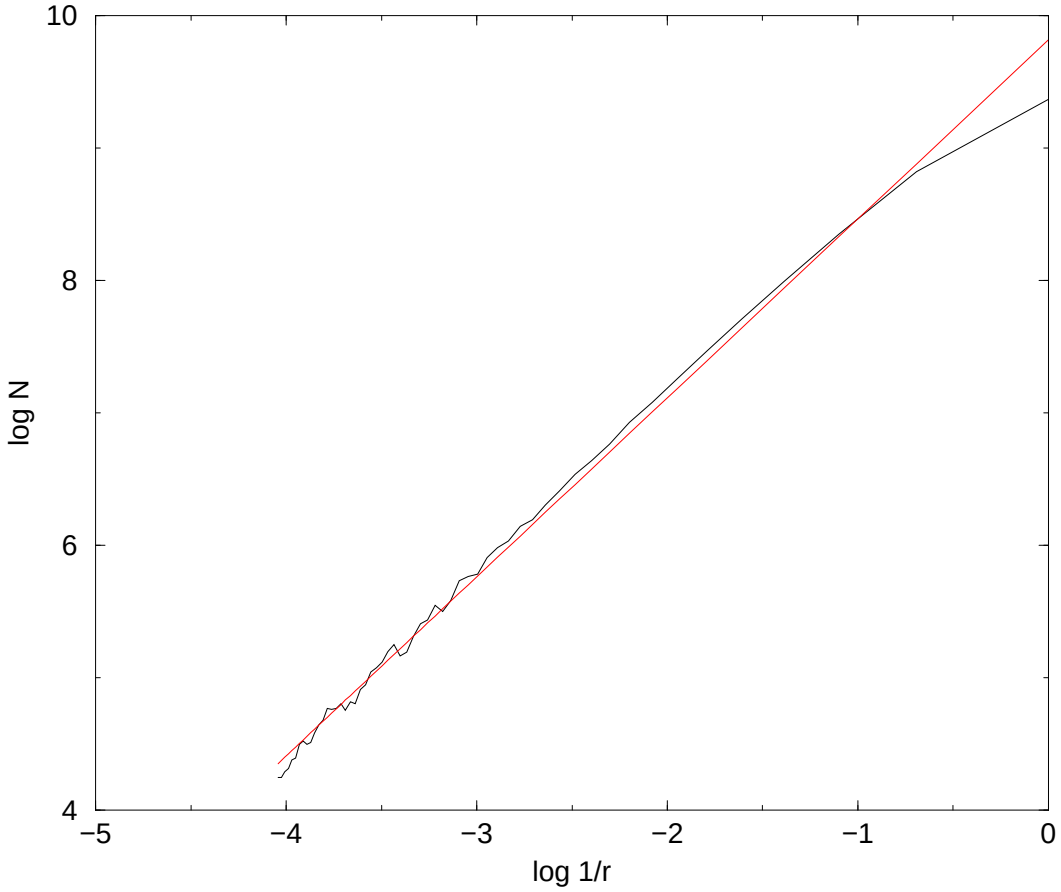

Figure 7.8: Graph of N against $\frac{1}{r}$

The correlation coefficient[2] of the graph is 0.998, showing the graph to be linear to a very close approximation. This suggests that the fractal dimension for the image is well defined. The ruler size ranges from 1 to 57 in this particular

[2]The correlation coefficient is defined as $\frac{\sum_i^N (x_i - \bar{x})(y_i - \bar{y})}{\sum_i^N (x_i - \bar{x})^2 \sum_i^N (y_i - \bar{y})^2}$ [68]

case, resulting in a dimension of 1.340 ± 0.013.

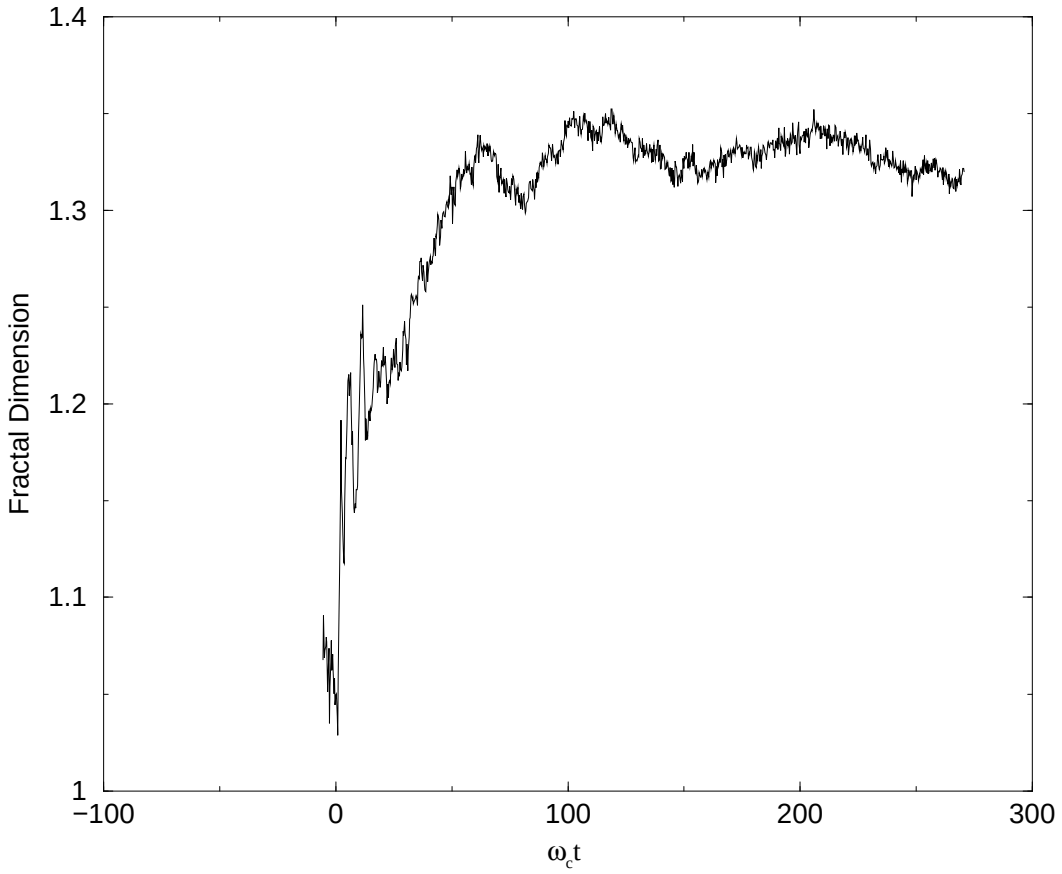

Figure 7.9: Graph of Fractal Dimension of Film Outline against Time

A graph of fractal dimension against time is shown in figure 7.9. As in all the graphs in this chapter, time is non-dimensionalised by multiplying time in seconds by the angular frequency of the central wavenumber of the wave.

Prior to breaking, the fractal dimension of the film's outline is approximately unity. In fact, it is slightly higher than one due to the formation of wisps of rhodamine beneath the surface during the application of the film. Immediately

after breaking, the dimension increases rapidly and there are a couple of sharp peaks in the graph. These are due to the changing vertical variance caused by the passage of crests and troughs: the slight overturning at the top of the graph of count against ruler size has a greater effect when the ruler range is smaller.

After these peaks, the fractal dimension increases steadily until ωt is approximately 60; then the dimension settles at a value of 1.32 ± 0.02.

The fractal dimension provides a measure of the degree of contortion of the film shape. This can be demonstrated by considering the ratio of film area to film perimeter. A logarithmic graph of these parameters is shown in figure 7.10.

The area initially increases rather rapidly while the perimeter fluctuates due to surface oscillations. The graph is then approximately linear until near the end of the experiment, when edge effects, caused by the film dispersing outwith the lightsheet, begin to dominate. The gradient of the linear region is 0.63, less than unity, indicating that the perimeter is increasing faster than the area. This suggests that the film shape is becoming increasingly detailed at smaller scales. The interface between the contaminant and the water has a growing surface-to-volume ratio due to intermediate and small scale eddies [73]. Steep concentration gradients result, and molecular diffusion becomes significant [69]. Many minutes after the end of the experiment, after the residual water motion has all but died away, the distinction between the film fluid and the water is no longer clear, because of this molecular diffusion.

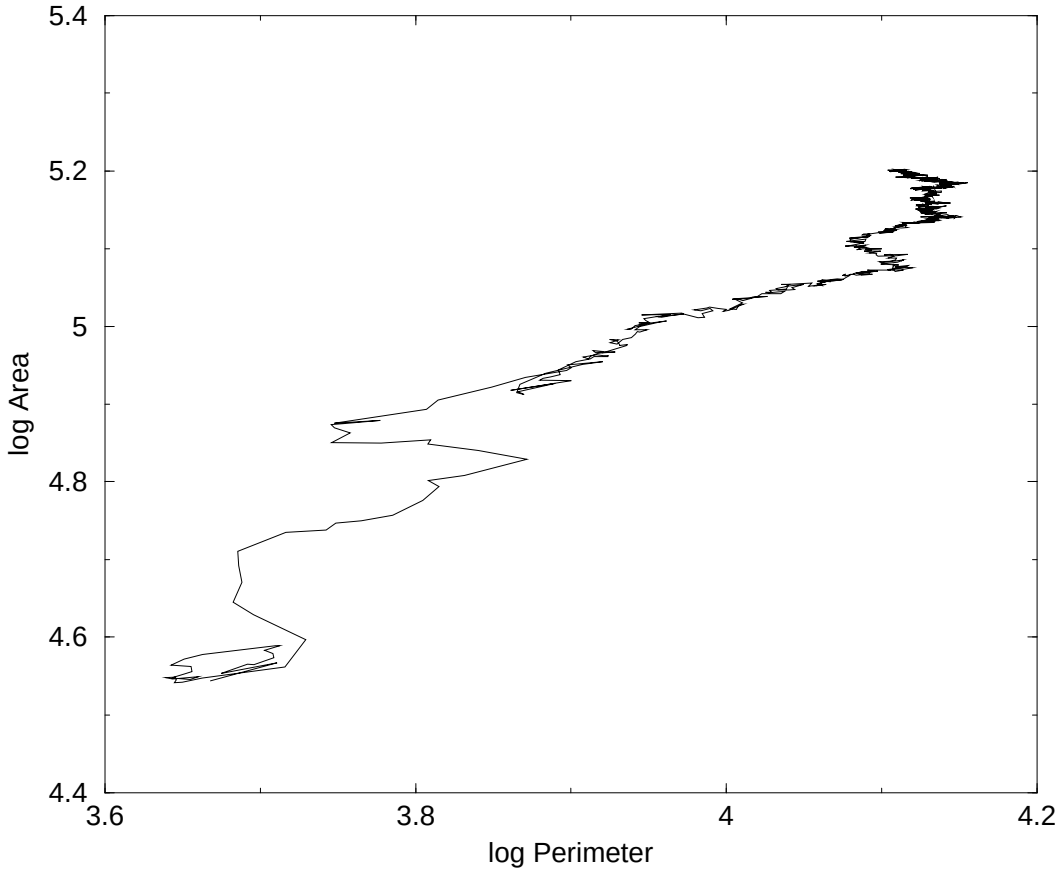

Figure 7.10: Graph of Log Area against Log Perimeter

It should perhaps be mentioned that the gradient m of a graph of $log\ Area$ against $log\ Perimeter$ is related to the box-counting fractal dimension d_B for statistically self-similar shapes by the relationship

$$m = \frac{2}{d_B} \tag{7.4}$$

[58]. This relationship, however, applies when the area and perimeter are measured as a function of ruler size for the *same* shape; in figure 7.10, the area and

perimeter of the film shape at *different* times are measured using a fixed ruler size of one pixel.

The value chosen for the threshold can have a significant effect on the fractal dimension calculation [61]. To investigate this, the threshold value in the calculation of the dimension of the LIF image in figure 7.7 was varied such that the cut-off occured at each of the concentration bands in turn. A graph of dimension against concentration band is shown in figure 7.11.

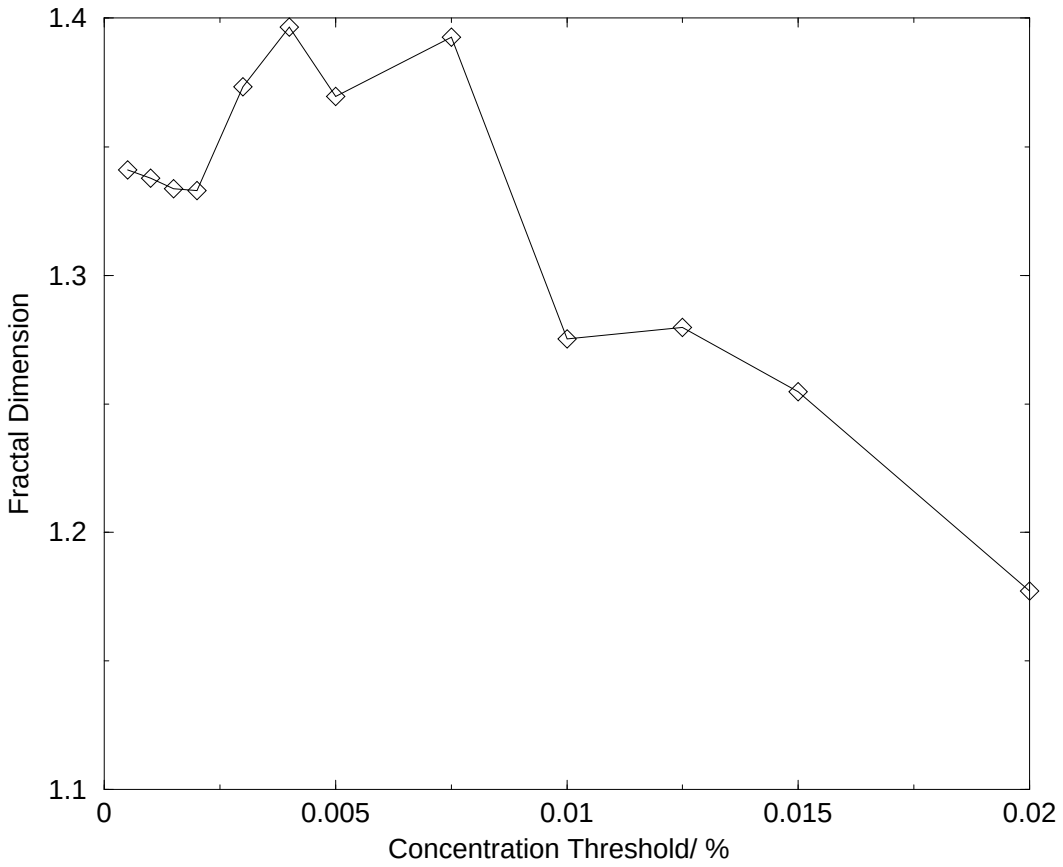

Figure 7.11: Graph of Fractal Dimension against Concentration Threshold

The dimension obtained is roughly constant for the four lowest concentration bands. Its value then increases, because the higher concentrations tend to be present near the surface where the motion is stronger and hence the outline more contorted. At the highest concentrations, most of the pixel levels are below the threshold, and the image becomes somewhat patchy. This has the effect of reducing the fractal dimension.

The background rhodamine level varied between experiments, since it was not practical to clean the tank between every experiment. It was found that a threshold level of 60 was sufficient to remove the background fluorescence in each of the experiments, equivalent to removing any concentrations below 0.0015%. This cut-off value was therefore used, so the threshold was the same in each of the fractal analyses.

7.3.6 Cross-Correlation of Images

A typical vector map obtained from cross-correlating LIF images $0.2s$ apart is shown in figure 7.12. In an attempt to demonstrate that the vectors do indeed represent the mean displacement of the film dispersion, the vectors have been superimposed onto an image whose red and blue levels correspond to the film concentration of the first and second image respectively. This image clearly shows the vertical motion due the the undulating surface.

Two modifications to the PIV analysis program were made to improve the

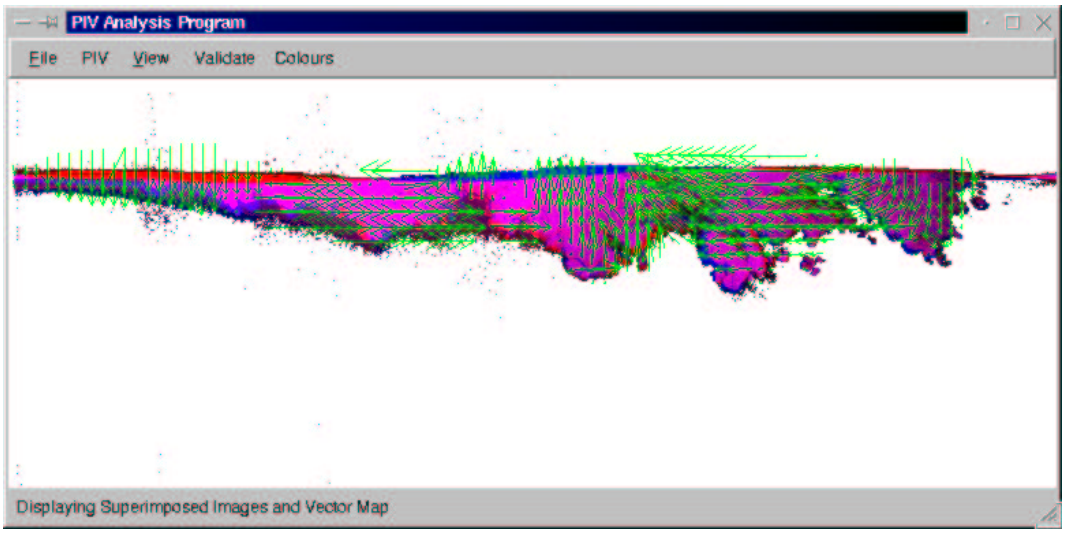

Figure 7.12: LIF image and calculated velocity vectors

quality of the vectors: firstly, correlations were only performed on interrogation areas whose mean grey level exceeded the global mean of the image. This prevented spurious vectors being calculated in regions where there was little fluorescence. Secondly, since the correlation ridges frequently extend towards the edge of the plane, it was necessary to modify the velocity bias correction to avoid vectors whose velocity components were $\frac{I}{2}$, where I is the size of the interrogation area. The correction, described in section 4.6, was applied only to points within $\frac{I}{4}$ pixels of the centre of the correlation plane. Since most of the displacements were less than this anyway, this correction was not believed to affect the vector map appreciably.

A series of vector maps is shown in figure 7.13, at 5 second intervals. These vector maps indicate the area covered by the film and the velocities of the concen-

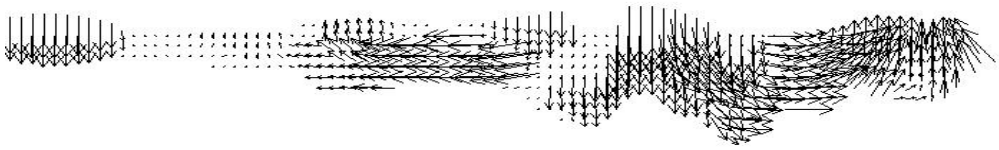

5 seconds after breaking

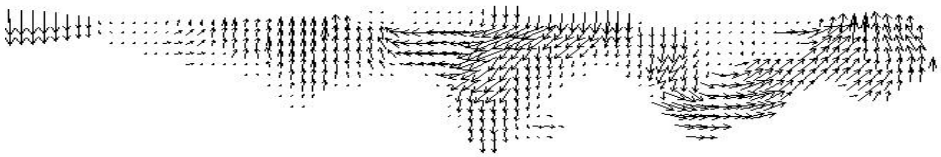

10 seconds after breaking

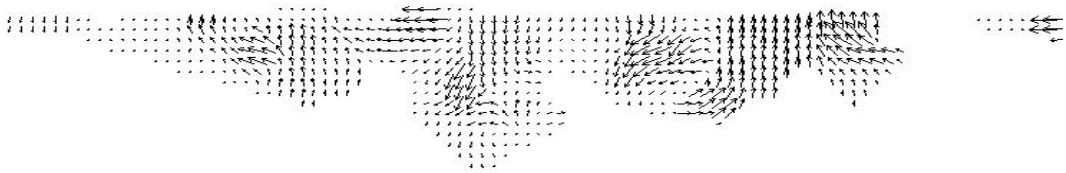

15 seconds after breaking

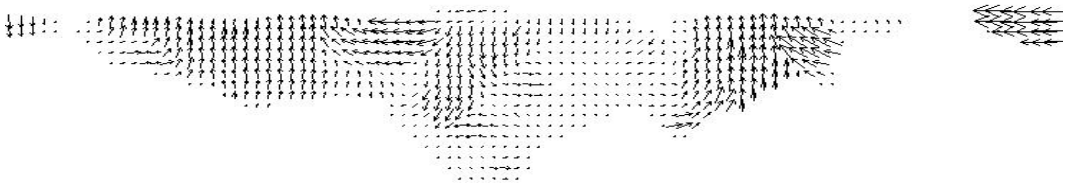

20 seconds after breaking

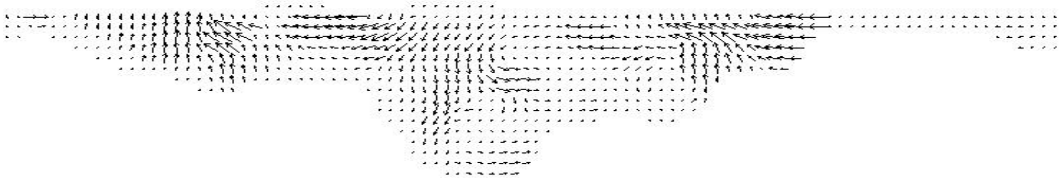

25 seconds after breaking

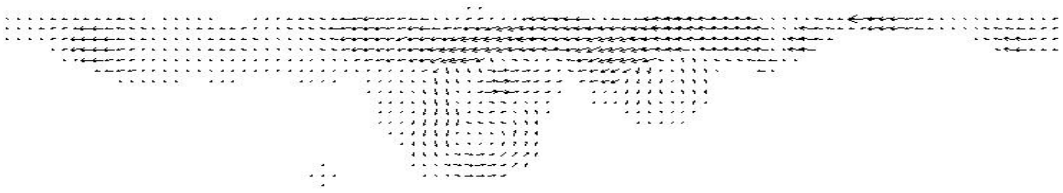

30 seconds after breaking

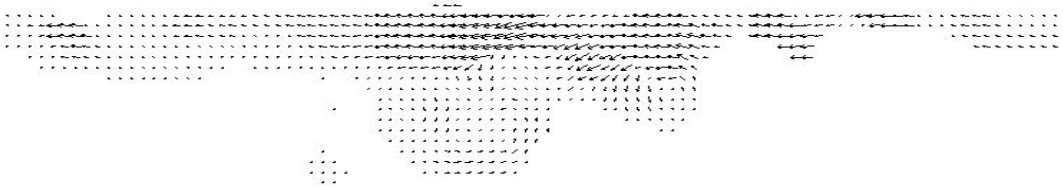

35 seconds after breaking

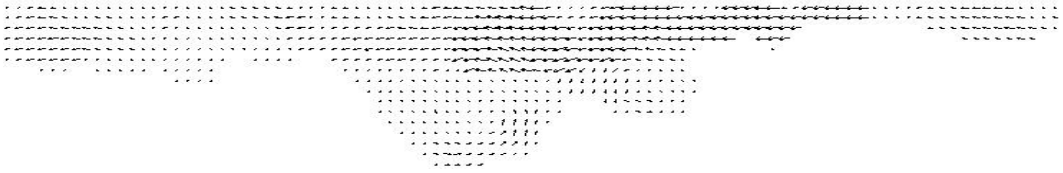

40 seconds after breaking

Figure 7.13: Sample Vector Maps

tration contours. The vector scale is the same in each image, thus revealing the decay in velocity with increasing time after breaking. The large, anti-clockwise vortices created by the plunging tip and the splash up are fairly clear in the vector map corresponding to 10 seconds after breaking. The motion of these vortices, downwards and to the left, can be seen in subsequent vector maps.

These vector maps can help to quantify features of the mixing which have been described only qualitatively so far. For example, it can be seen that the vector lengths tend to be longer near the surface, indicating that the fluid motion is more rapid there than deeper down. The mean vector velocity is in fact an order of magnitude larger at the surface than at the bottom of the deepest vortex.

In addition, the mean x velocity for all the vector maps shown in figure 7.13 is approximately -2 pixels per second, thus providing a measure of the motion of the film outwith the field of view of the cameras. The mean y velocity is only 0.1 pixels per second, indicating a very slight net downward motion.

The vector maps obtained did appear to represent the motion of the film dispersion, though there were a number of outliers, particularly in regions without contorted concentration contours. Further investigation into the performance of the correlation algorithm, and the peak detection in particular, to establish the accuracy of the velocities obtained, would be worthwhile. This is particularly important for the evaluation of flow properties involving differentials, such as vorticity.

7.4 Repeatability of Mixing

The results presented thus far were obtained from a single experiment involving one breaking wave. In an effort to determine whether they are general results or unique to that experiment, a number of repeats were performed. Because each experiment was time-consuming, it was not possible to carry out a statistically significant number of trials. Instead, the experiments were repeated five times to give an indication of the repeatability, or otherwise, of the mixing.

It was anticipated that differences between individual experiments might be greater for larger breaking events; for this reason, the repeatability of the mixing of the largest amplitude breaker, corresponding to a non-dimensional amplitude of $ak = 0.35$, was investigated.

In this section, graphs depicting the data obtained from the five repeats are colour-coded such that the same colour in different graphs refers to the same experimental run.

7.4.1 Repeatability of Depth Reached

A graph of the maximum depth reached by the lowest concentration of film as a function of time for each of the five repeats is shown at the left of figure 7.14. The average and standard deviations of these curves are plotted at the right.

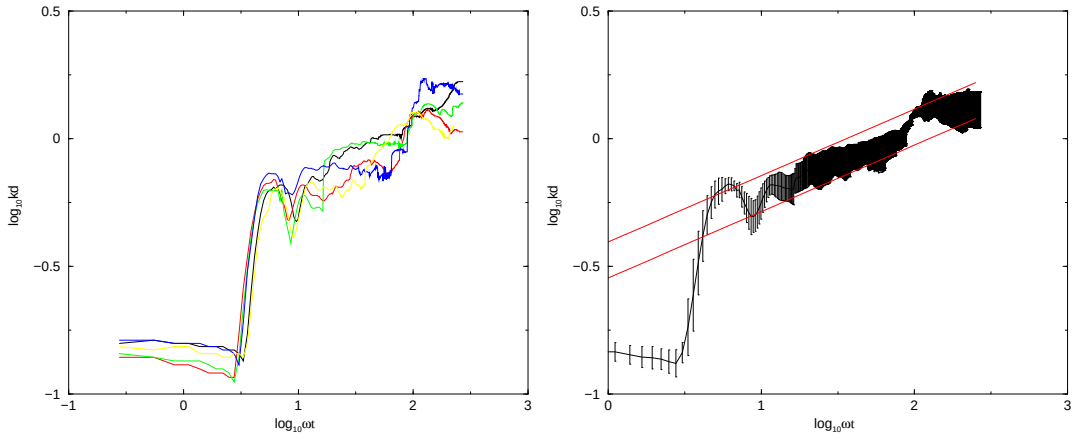

Figure 7.14: Repeatability of Depth Reached against Time

The depth reached increases at approximately the same rate in all five repeats, although there are unpredictable differences in the plotted data.

Using linear regression, the gradient of the average curve in the region $1 < \log_{10}\omega t < 2.2$ is 0.258 ± 0.005. Following the procedure of Rapp and Melville [17], the range of the dispersion coefficient was obtained by plotting two $p = 0.258$ lines to encompass the data spread. The average non-dimensionalised depth reached by the films is then

$$k_c d = (2D\omega_c t)^{0.26} \tag{7.5}$$

where $0.004 < D < 0.014$.

7.4.2 Repeatability of Area Covered

A graph of the area covered by the film as a function of time is plotted at the left of figure 7.15; the average and standard deviations of these curves are displayed at the right.

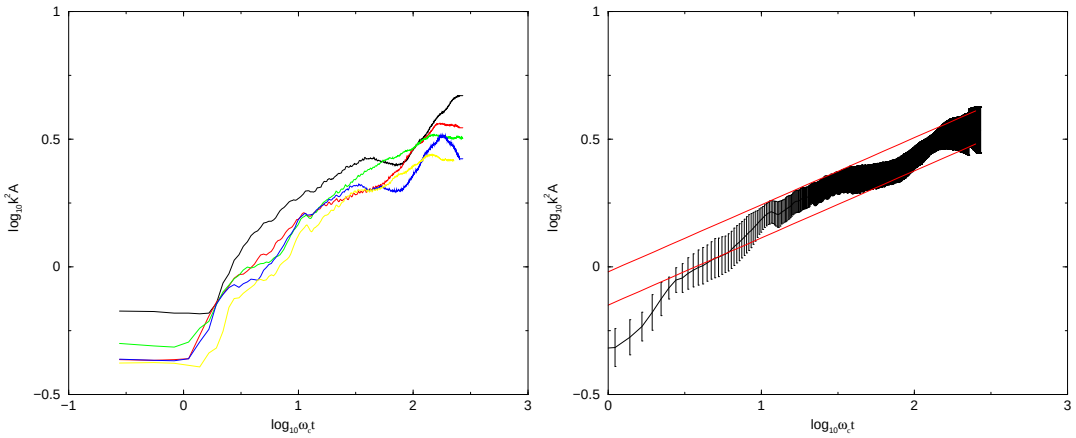

Figure 7.15: Repeatability of Area Covered against Time

The area of the film increases rapidly immediately after breaking, but the rate of increase reduces with time, as the film moves outwith the field of view of the cameras. In one repeat there is a sharp fall in area near the end of the experiment. A dispersion coefficient and exponent were calculated for the film area as a function of time, for $log_{10}\omega_c t > 1$. In this region, the non-dimensionalised area can be written as

$$k_c^2 A = (2D\omega_c t)^{0.26} \tag{7.6}$$

where $0.13 < D < 0.42$.

Like the depth reached, the area covered by the film as a function of time is essentially the same between repeats, despite the presence of small scale fluctuations.

7.4.3 Repeatability of Centre of Mass position

Figure 7.16: Centre of Mass of Film

Colour-coded plots of the position of the centre of mass of the dispersing patch are shown for each repeat in figure 7.16. For the first 3 seconds after breaking, the position of the centres of mass are dominated by the passing crests and troughs. For a period thereafter, which varies between repeats, the trajectory followed by the centres of mass is approximately linear. The non-dimensional mean velocity of the centres of mass in this steady region is 0.048 ± 0.008, while the average angle of descent is -3 ± 2^0.

7.4.4 Repeatability of Dispersion Coefficients

A graph of the vertical and horizontal standard deviations, σ_y and σ_x, of the patch size as a function of time is shown is figure 7.17. Before breaking, and for approximately $2.5s$ afterwards, the standard deviations from the separate repeats are closely matched. Thereafter, the general trend is the same between repeats, with σ_y tending to increase and σ_x initially reducing and then increasing, but there are unpredictable kinks and dips in the graphs that differ between experiments.

The experiments are essentially repeatable until shortly after breaking: the film remains on the surface before breaking, and the wave breaks at the same time and location on separate runs. But while the qualitative features of the dispersion, described in section 7.2, occur each time, the precise size and motion of the dispersion patch, and features such as the locations of the isolated patches, vary each time. Thus the dispersion of a surface film after wave breaking appears to be a chaotic process. Small deviations between experiments, such as the initial distribution of the film, or residual motion in the tank, lead to large differences in the quantitative description of the patch, just a few seconds after breaking.

Between the range of $1.15 < log_{10}\omega_c t < 2.15$, the vertical variance increases as

$$\sigma_y k_c = (2 \times D_y \times \omega_c t)^{0.41} \tag{7.7}$$

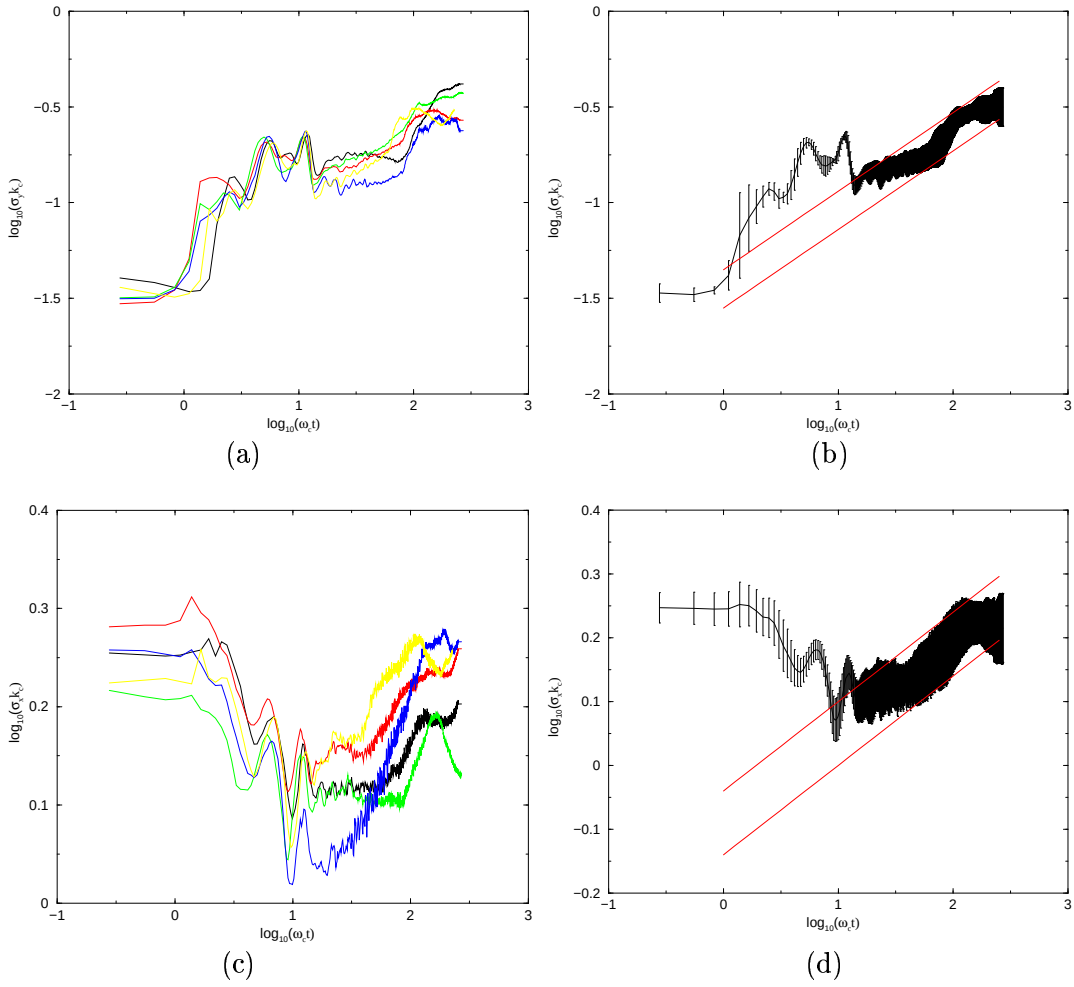

Figure 7.17: Graphs of Vertical and Horizontal Standard Deviation against Time for 5 repeats

where $2.5 \times 10^{-4} < D_y < 8.3 \times 10^{-5}$. In the same time region, the horizontal variance can be represented by

$$\sigma_x k_c = (2 \times D_x \times \omega_c t)^{0.14} \tag{7.8}$$

The horizontal dispersion coefficient, D_x, is in the range $0.05 < D_x < 0.26$. The

limits of these ranges are represented by the red lines in figure 7.17 (b) and (d).

7.4.5 Repeatability of Fractal Dimension

A graph of fractal dimension against time for each of the repeats is shown in figure 7.18.

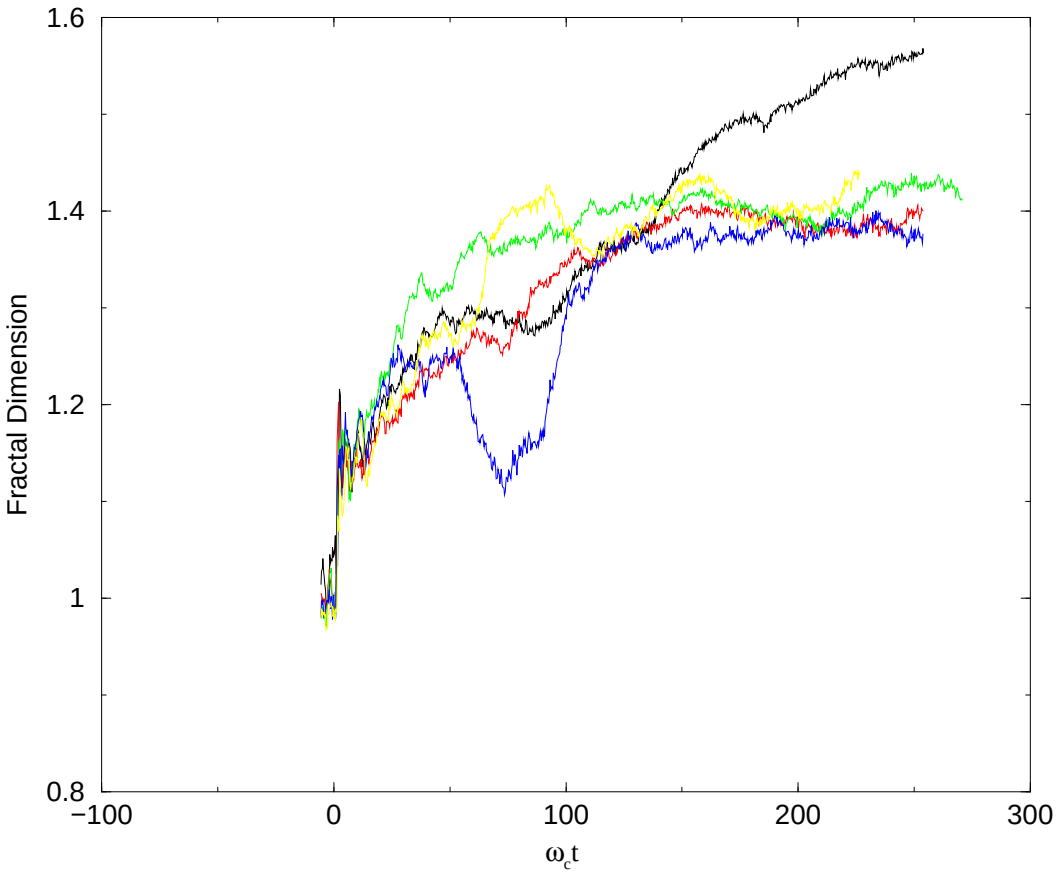

Figure 7.18: Repeatability of Fractal Dimension against Time

As before, the fractal dimension is approximately unity around breaking, and increases after breaking. The graph contains two significant deviations from the

general trend upwards to a dimension of approximately 1.4. The first such deviation is the blue curve between $50 < \omega t < 100$, where the fractal dimension drops considerably before rising again. This is believed to be due to the film distribution being somewhat patchy in the images obtained in this repeat. Fragmented sections of film tend to have a lower fractal dimension than continuous sections, since they resemble points to the larger ruler sizes.

In four out of five of the repeats, the fractal dimension levelled out at approximately 1.4. In the other repeat, represented by black, the fractal dimension almost reaches a value of 1.6. The reason for this discrepancy is not clear, though it is noted that the vertical variance of the patch is largest for this repeat, and that the graph contains a region of rapid expansion, as can be seen in figure 7.17.

7.5 Effect of Amplitude

In order to investigate the effect of amplitude on film dispersion, experiments involving five different wave amplitudes were conducted. The selected amplitudes were $0.099m$, $0.102m$, $0.105m$, $0.108m$ and $0.111m$. The central frequency and spread were kept constant. Thus the non-dimensional amplitudes were $ak = 0.314$, 0.324, 0.333, 0.342 and 0.352. The smallest ak value resulted in a spilling breaker, while the other values resulted in plunging breakers of increasing strength. The effect of ak on the dispersion characteristics are described here.

7.5.1 Effect of Amplitude on Depth Reached

The maximum depth reached by a film concentration of 0.001% for the five different waves, as a function of time, is shown in figure 7.19.

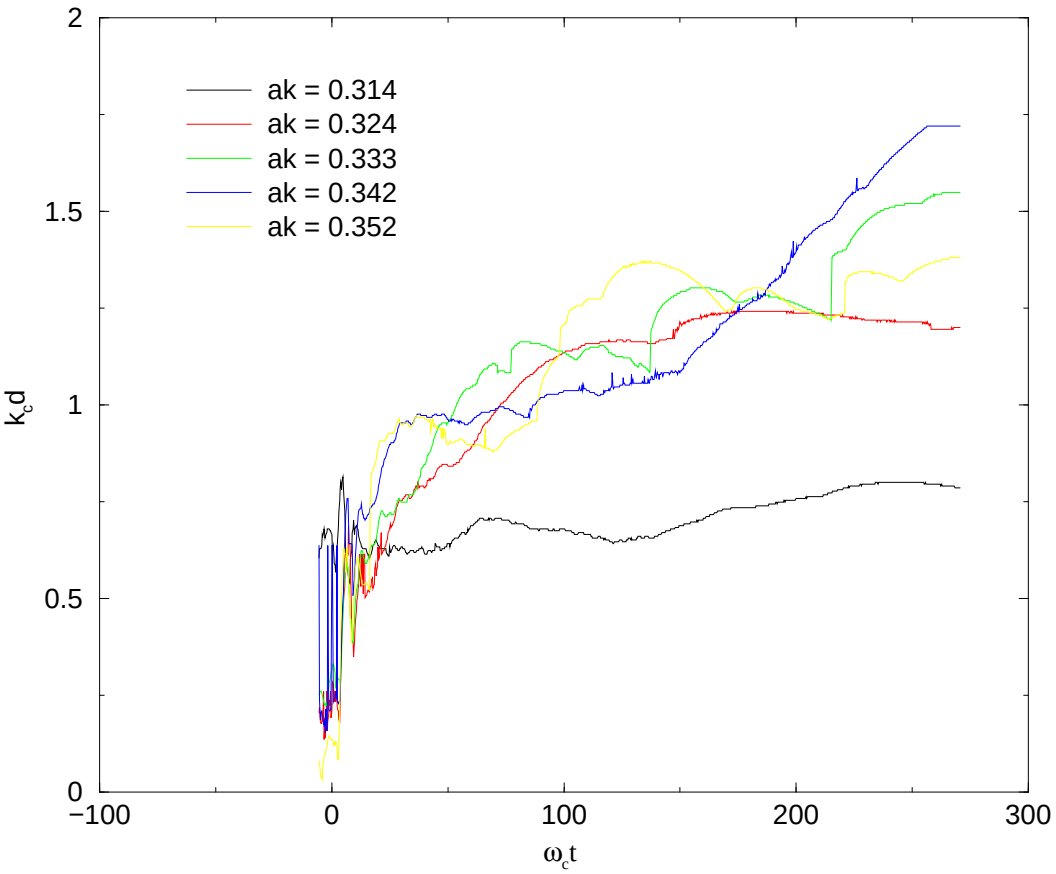

Figure 7.19: Effect of Amplitude on Depth Reached by Film

The depth reached by the spilling breaker, $ak = 0.314$, is considerably less than the depths reached by the plunging breakers. There is a suggestion that plunging waves of larger amplitudes mix the surface contaminant deeper than those of smaller amplitudes, although this trend is broken by the largest amplitude

wave in the set. Furthermore, both the surface tension and the air-entrainment tend to inhibit downward penetration [74], and have different relative importances at different scales. Thus the extrapolation of results obtained in a single tank to other flow regimes is far from trivial.

7.5.2 Effect of Amplitude on Area Covered

The area of the LIF images covered by a film concentration of at least 0.001%, for each of the five different wave amplitudes, is shown in figure 7.20.

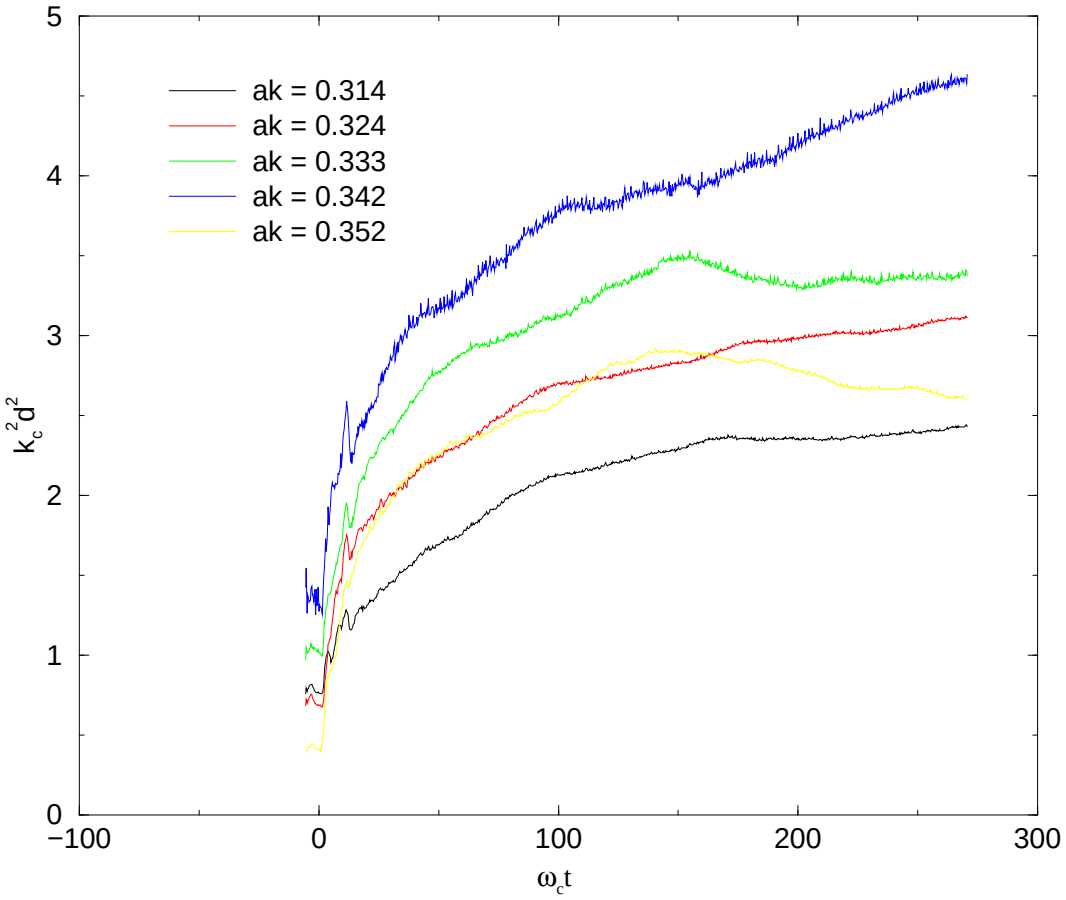

Figure 7.20: Effect of Amplitude on Area Covered by Film

As in figure 7.19, there are indications of a trend that larger waves result in a larger dispersing patch, this time in terms of area. Again, however, this trend is broken by the largest plunging breaker. In addition to the rate of expansion of the patch, the area of the film is affected by the amount of movement of rhodamine outwith the field of view of the cameras. Since this might be expected to be larger for the bigger waves, results for the largest amplitude waves may be less reliable than those from smaller amplitudes.

7.5.3 Effect of Amplitude on Centre of Mass Motion

The motion of the centre of mass of the film patch is shown in figure 7.21 for each of the five different breaking waves under investigation. Each plot is colour-coded in the way described in section 7.3.3. The initial portion of each graph, coloured red, is dominated by residual surface disturbances. The centre of mass then moves in the direction of wave propagation. The centre of mass motion from the $ak = 0.314$ experiment, corresponding to the spilling breaker, is slow

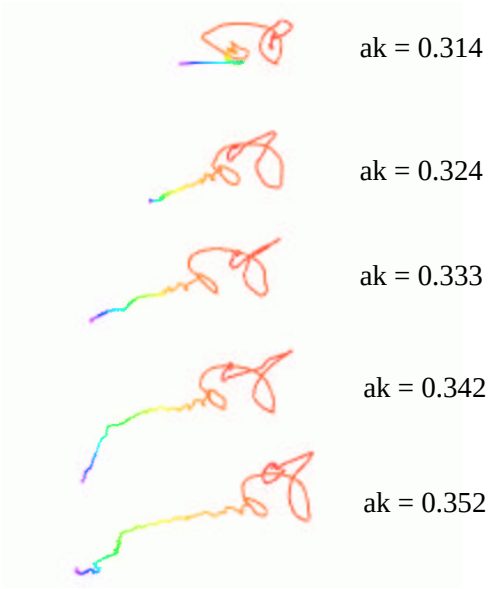

Figure 7.21: Centre of Mass of Film

and close to the horizontal compared to the others. There appears to be a trend that the film's centre-of-mass will travel faster and deeper if the wave amplitude is larger.

7.5.4 Effect of Amplitude on Dispersion Coefficients

The non-dimensionalised vertical and horizontal standard deviations are plotted against time at the left and right of figure 7.22 respectively. From the graph involving σ_y, it can be seen that the spilling breaker results in less downward mixing of the film than the plunging breakers. There is no obvious relationship between wave amplitude and dispersion coefficients or exponents, though once again, the vertical mixing seems larger for larger breakers.

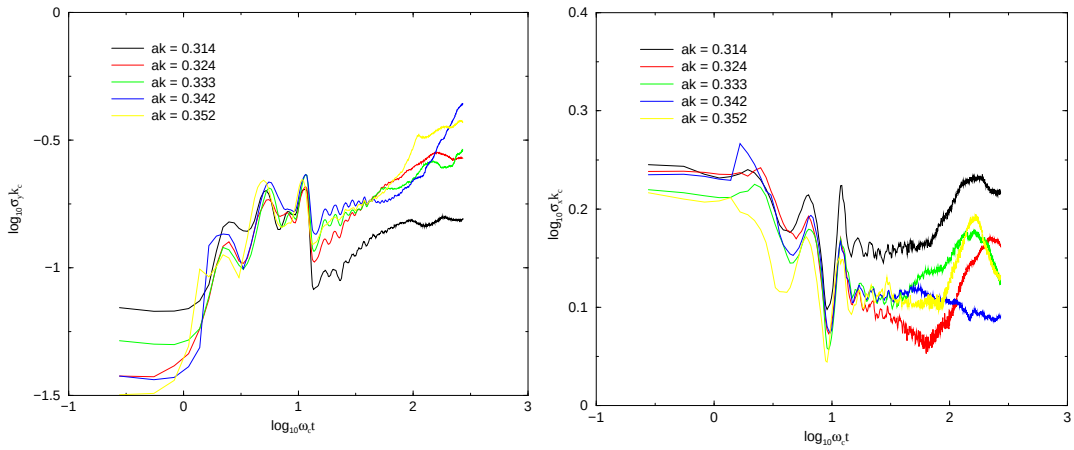

Figure 7.22: Graph of Vertical (left) and Horizontal (right) Standard Deviation against Time for 5 wave amplitudes

The horizontal variance of the patch is larger in the spilling than the plunging breaker experiments, because the spilling process occurs over a longer spatial and

temporal period than the plunging event, resulting in a wide, shallow dispersion cloud.

7.5.5 Effect of Amplitude on Fractal Dimension

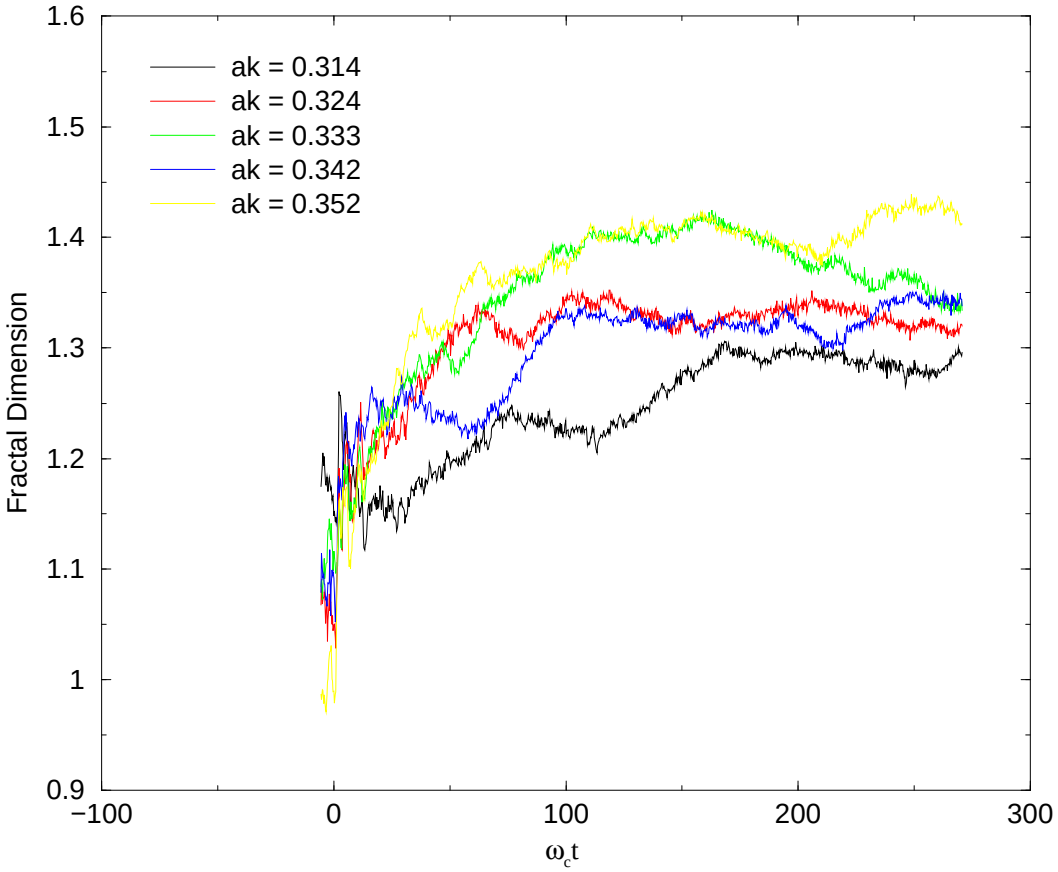

Figure 7.23: Effect of wave amplitude on Fractal Dimension

Graphs of fractal dimension against time for five different wave amplitudes are shown in figure 7.23. In each case, the tendency is for the fractal dimension to increase with time. The value of the fractal dimension at the end of each

experiment appears to be related to the amplitude of the breaking wave: the larger the amplitude, the higher the fractal dimension. Many more repeat experiments would be required before this trend could be presented as a conclusion, since the difference in dimension between the different film outlines is less than the standard deviation of the dimensions calculated from the repeat experiments.

Nevertheless, this trend does make intuitive sense. Larger amplitude waves contain more energy, which in turn leads to increased mixing and more contorted film distributions. From the experiments conducted to investigate the effect of amplitude, it appears that the fractal dimension of the film outline increases from approximately unity to around 1.3 for spilling breakers, up to around 1.4 for large plunging breakers.

7.6 Comparison with Other Work

Rapp and Melville [17] conducted experiments on the spatial evolution of the mixing of a surface film of food dye after breaking, and investigated the depth reached and area covered as a function of time.

Prasad and Sreenivasan [75] performed LIF experiments on turbulent water jets, and investigated the fractal dimension of the scalar interface.

In this section, the results presented thus far are compared to this published material.

7.6.1 Depth

Rapp and Melville [17] fitted a power law of the form

$$k_c D = \gamma \left[\omega_c t\right]^p \tag{7.9}$$

to their measurements of film dispersion, where t is the time from observed breaking. They used a fixed dispersion exponent of $p = \frac{1}{4}$ (equivalent to H in the notation used here) and varying dispersion coefficient $0.28 < \gamma < 0.57$. γ is related to the dispersion coefficient D defined in equation 6.16 via

$$\gamma = (2D)^H \tag{7.10}$$

The average depth reached from the 5 repeats yielded a value of 0.26 for H and $0.28 < \gamma < 0.39$, in good agreement with Rapp and Melville. In individual repeats, and the experiments involving breakers of different amplitudes, the dispersion did deviate significantly from 0.25 in some cases. In order to compare the dispersion, graphs of depth against time are plotted together with the logarithm of the power laws $y = 0.28x^{0.25}$ and $y = 0.57x^{0.25}$. This is shown in figure 7.24.

The limits obtained by Rapp and Melville are shown as dotted orange lines in figure 7.24. Thus despite differences in the values obtained for the dispersion exponent, the depths reached by the films in these experiments are generally

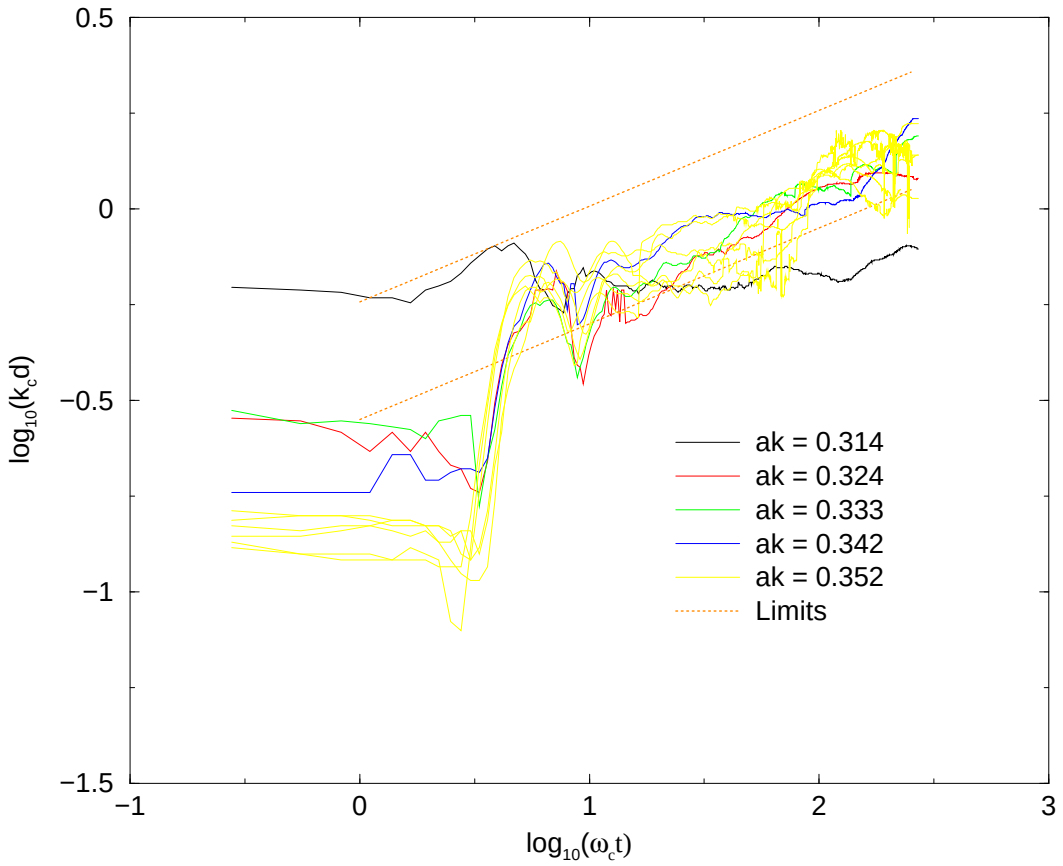

Figure 7.24: Depth against Time

consistent with the range proposed by Rapp and Melville. The one obvious exception is the spilling breaker, which does not penetrate as deep as expected.

7.6.2 Area

Rapp and Melville also obtained a power law of the form

$$k_c^2 A = \gamma \left[\omega_c t\right]^{\frac{1}{2}} \tag{7.11}$$

to quantify the area covered by the film, for $\log \omega t > 1$, where $0.32 < \gamma < 0.74$.

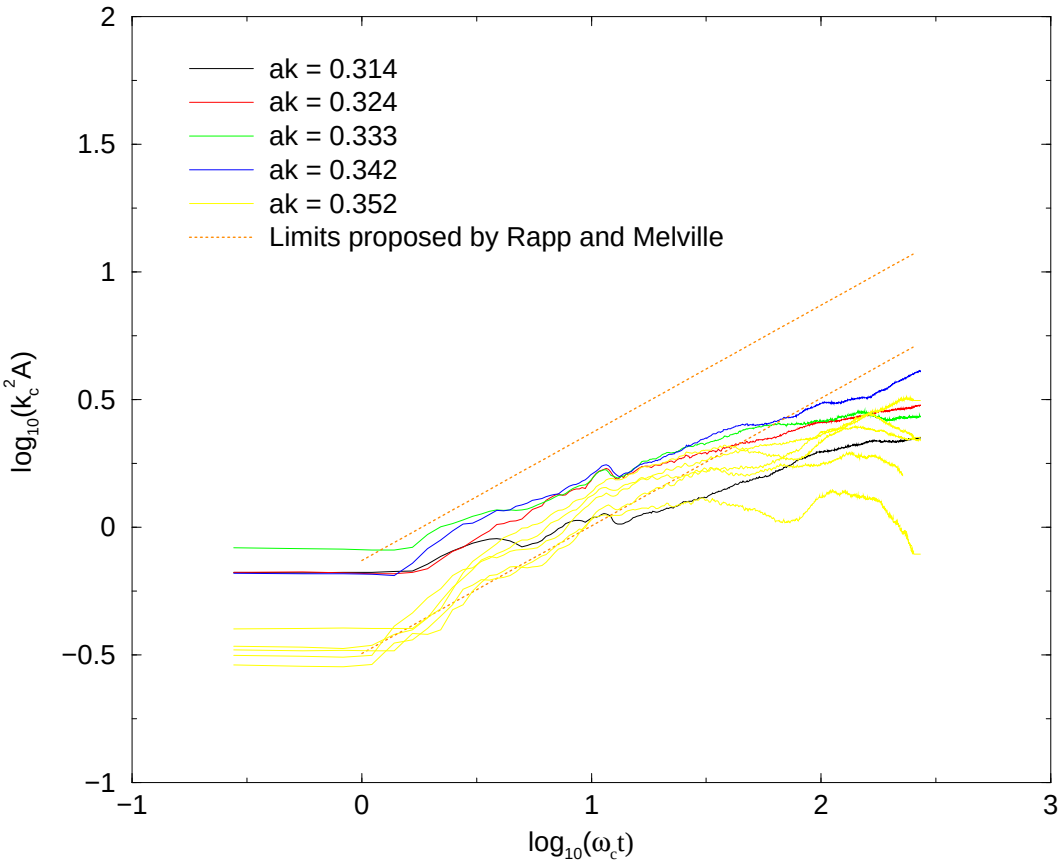

Figure 7.25: Area against Time

It was found that the dispersion exponent in these experiments was less than $\frac{1}{2}$ in this region. Thus most of the graphs of area against time in figure 7.25 fall below the lower limit proposed by Rapp and Melville. This is believed to be largely due to film moving outwith the field of view of the cameras during the experiment. Another possible reason for the discrepancy is that in these experiments the tank is illuminated by a thin lightsheet rather than the diffuse lighting in the Rapp and Melville experiments. Thus only contaminant present

at the centre of the tank will be included in the area calculations from these experiments, so a lower rate of expansion than Rapp and Melville calculated might be anticipated. This difference in methods should not affect the depth results since one would expect that the maximum depth would occur near the centre of the tank where viscous drag from the walls is minimal.

7.6.3 Fractal Dimension

The values obtained for the fractal dimension of the film outline generally ranged between 1.3 and 1.4. Viecelli [76] showed that the fractal dimension of the boundary between a diffusing contaminant and the surrounding fluid is $\frac{4}{3}$ in fully three-dimensional turbulence. Although the motion of the water is not fully turbulent after wave breaking, this indicates that the values obtained for the fractal dimension are plausible. Furthermore, LIF experiments on turbulent water jets, a fluid problem closely related to the plunging jets in breaking waves, have shown that the fractal dimension of the scalar interface between fluids is 1.36 ± 0.05 [75].

There were indications that the value obtained for the fractal dimension might increase with increasing wave amplitude. Similarly, it was found that larger breaking events tended to result in more dispersion than smaller breakers. This suggests that there may be some correlation between the fractal dimension and the dispersion coefficient/exponent. In the previous chapter, however, it was

noted that in fractional Brownian motion, the fractal dimension *decreases* as the dispersion coefficient grows. That fractal dimension referred to the trajectory of a *single* dispersing fluid element, while the dimension in this chapter is related to spatial distribution of a number of fluid elements, each of which marks the boundary between film and water. Thus there is no contradiction that different fractal dimensions might respond differently as the dispersion exponent changes.

7.7 Conclusions

LIF has been applied to the dispersion of a surface film after wave breaking. The technique provided both spatial and temporal information about the concentration distribution of the film. This information was analysed to obtain various quantitative data, which was presented in this chapter. The depth reached and area covered by the film were compared to similar research: the depth measurements agreed well with previous work; there was less good agreement between the area measurements which was due to the film dispersing outwith the field of view of the cameras during the course of the experiments. The fractal dimension of the film boundary was calculated and was found to increase from approximately 1 to 1.3-1.4 in most cases, consistent with related theoretical and experimental work.

LIF is therefore a very effective technique for obtaining quantitative informa-

tion concerning post-breaking dispersion. The lengthy preparation time required to perform each experimental runs limited the number of runs which were conducted. Those which were performed indicated that, while the precise spatial distribution of the film concentration did vary between experiments, the same gross features were observed and there was generally good agreement between derived quantities such as the depth reached and area covered by the film.

It is not possible to present strong conclusions such as the effect of wave amplitude on dispersion. There are indications, however, that the fractal dimension, depth reached, area covered and dispersion coefficient are likely to be greater for waves of larger amplitude. Many more experiments would be required to determine the true dependency.

Chapter 8

Dual-Plane PIV Experiments

8.1 Introduction

The results presented so far have related to the evolution of the concentration distribution of a surface film after wave breaking. In this chapter, the experiments conducted to investigate the water motion responsible for this mixing are described.

The results to be presented were obtained using the technique of dual-plane PIV, the principles of which were discussed in chapter 4. The practical details of the experiments are described in the following section, and the results obtained are documented in section 8.3.

The coordinate system is defined such that the lightsheet is located in the xy

plane, and the lightsheet shift and out-of-plane motion are in the z direction.

8.2 Experimental Method

The dual-plane PIV experimental apparatus is similar to the apparatus used in the LIF experiments, shown in figure 3.4, with a few minor modifications. Firstly, since PIV involves imaging small tracer particles, the field of view of the imaging lens is necessarily smaller than was adopted for the LIF experiments, so a diverging lightsheet is unnecessary. In order to maximise the intensity of the lightsheet, the smallest parabolic scanning beam box available, $0.5m$ long, was used. Secondly, the pair of cameras used to create widescreen images was replaced by the 4-camera system, or if the flow were sufficiently slow, by a single camera. Thirdly, it was necessary to introduce an additional piece of apparatus to rapidly shift the lightsheet between images. The PIV experiments were carried out in the purple tank laboratory, as the Argon Ion laser there was more powerful. This equipment is described in the following subsection.

8.2.1 Displacement of the Lightsheet

The lightsheet is displaced by a *Sheet Moving Device*, or SMD. The SMD is shown in figure 8.1; it consists of a disk containing three apertures, two of which are empty while the third has a slab of optically flat glass within. The

disk is angled with respect to the incident laser beam and rotated by a stepper motor. The *Stepper Motor Driver* is designed to rotate the SMD by a third of a revolution each time it receives a TTL pulse.

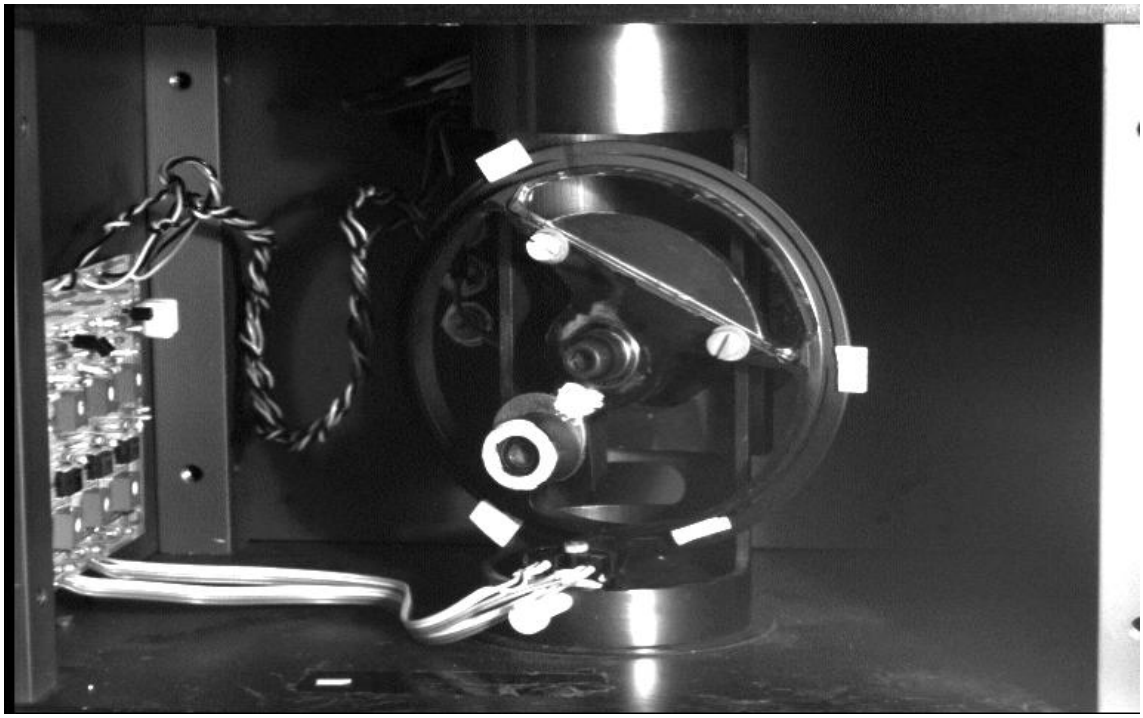

Figure 8.1: Sheet Moving Device

The laser beam is unaffected by the air apertures of the SMD, but is displaced sideways due to refraction by the glass slab as shown in figure 8.2.

The amount of displacement, x, depends on the thickness of the glass, d, the angle of incidence, θ, and the refractive indices of the air and glass, n_1 and n_2 respectively, according to the equation

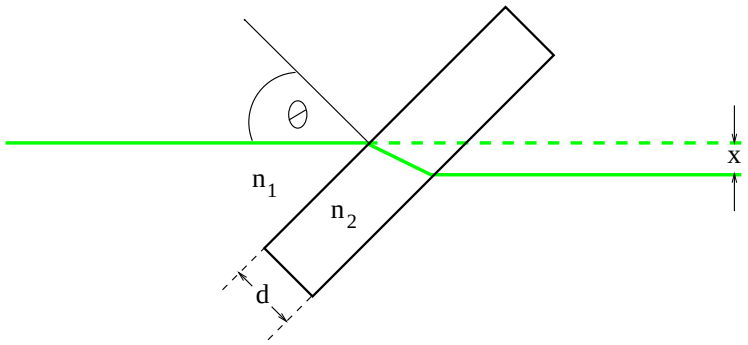

Figure 8.2: Refraction through a slab of glass

$$x = d \sin\theta \left[1 - \frac{\cos\theta}{\left(\frac{n_2}{n_1}\right)^2 - \sin^2\theta} \right] \tag{8.1}$$

The frame separation, Δt, between successive images is equal to the time taken for the SMD to rotate one third of a revolution. The SMD was capable of rotating between $25Hz$ and approximately $200Hz$, which set upper and lower bounds on the flow velocities capable of being measured.

Originally, attempts were made to synchronise the rotation rate of the SMD to the octagonal mirror in the Scanning Beam Box (SBB), as recommended by Dewhirst [37], so that an integer number of lightsheets were produced during each exposure of the camera. This was to ensure that the pseudo-lightsheet appeared uniformly bright across its width. The SBB contains a photodiode, which emits a pulse each time the laser beam sweeps along the parabolic mirror. This pulse train was used as the input into the Stepper Motor Driver, but because the minimum

rotational frequency of the octagonal mirror is $50Hz$, resulting in 400 pulses per second, it was necessary to pass the train through a divide by N circuit first.

The drawback of this approach is that the metal arms separating the apertures in the SMD block the laser beam three times per rotation. If the beam is blocked when otherwise it would be activating the photodiode, the SBB will not emit a pulse during that particular sweep. The pulse train emitted by the SBB is therefore not quite regular, because some pulses are missing. Since this pulse train is used to drive the SMD, the resulting rotation rate is not uniform. This results in chaotic feedback as the SMD interferes with the pulse train driving it.

This problem was avoided by sending a regular pulse train from a pulse generator to the Stepper Motor Driver, ignoring the pulses emitted by the SBB, thereby ensuring that the SMD rotated at a uniform rate.

The time taken for the laser beam to sweep across the parabolic mirror is $\frac{1}{8f_{SBB}}s$, where f_{SBB} is the frequency of the octagonal mirror. If f_{SBB} is large compared to the rotational frequency of the SMD, there will be a number of lightsheets formed during every pass of each aperture. Any fractional sweep of the laser beam should then have little effect on the brightness of the images.

8.2.2 Camera Triggering

Although it was not necessary to synchronise the Sheet Moving Device to the Scanning Beam Box, it was essential to sychronise it to the camera system.

There are a number of considerations to ensure that the appropriate frame is captured at the appropriate time. Firstly, the time during which each frame is exposed should correspond to one, and only one, aperture passing in front of the laser beam. Secondly, for the dual-plane algorithm described in section 4.10.1 to apply, the middle image must be taken with the lightsheet in its displaced position, that is, with the glass aperture in front of the beam. Finally, the sequence of image triplets should begin at a relevant point in the flow.

In order to trigger the camera system appropriately, three pulse trains and some electronic circuitry are required. One pulse was emitted each time a new aperture moved in front of the laser beam; this *aperture pulse* was used to begin the camera exposure. The frequency of this pulse train, $f_a = \frac{1}{\Delta t}$, where Δt is the time separation between the images, was the highest of the three.

Another pulse, known as the *synch pulse*, was used to alert the system that the next approaching aperture corresponded to the one immediately before the glass aperture. One such pulse was emitted during each rotation of the Sheet Moving Device. The frequency of this pulse train was $\frac{f_a}{3}$

The period of the final pulse train, termed the *user trigger*, determines the

separation between image triplets. The first pulse of this train effectively begins the acquisition of dual-plane PIV images.

These pulse trains, and the required trigger pulses are shown schematically in figure 8.3.

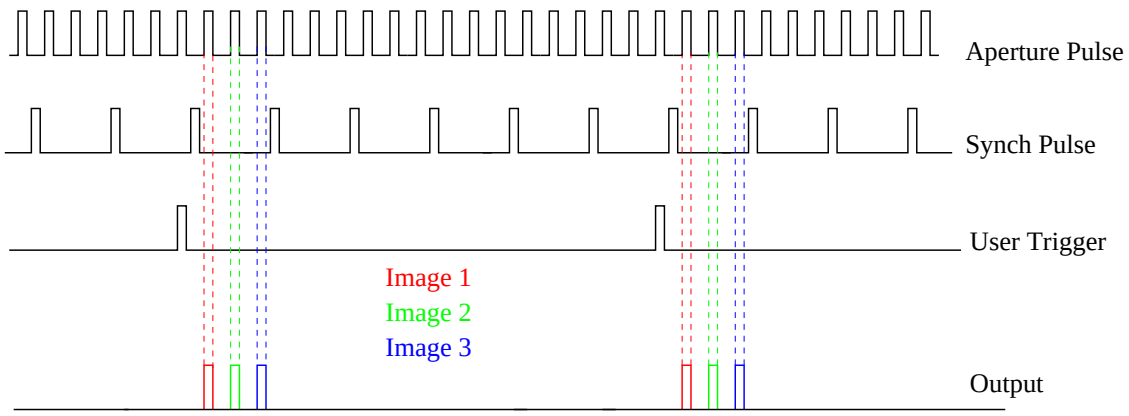

Figure 8.3: Timing Pulses

The timing logic operated as follows: a user trigger pulse signified that an image triplet was required and alerted the circuitry to respond to the other pulse trains. The synch pulse informed the system that the next pulse in the high frequency train would correspond to the aperture before the glass, and should thus be used to trigger the first camera. The following pulse in the high frequency train corresponded to the glass aperture moving in front of the laser beam, and was used to trigger the second camera image, of the particle positions within the displaced lightsheet. The next high-frequency pulse was used for triggering the third and final camera image in the sequence.

Once this was done, the circuitry reset and waited for the next user trigger, after which the above sequence was repeated.

The aperture pulse train and synch pulses were produced by the Sheet Moving Device itself. The SMD has two infra-red photodiodes positioned one above the other such that they face the outer rim of the rotating disk. These photodiodes were calibrated such that they are logically ON if the rim in front of them is black, and logically OFF if the rim is white. White sticky pads were positioned such that the lower photodiode changed state as a new aperture moved into place and the upper photodiode emitted a synch pulse as the air aperture prior to the glass was approaching.

Dewhirst [37] built a timing box which requires a user trigger and an optional synch trigger before emitting TTL pulses on separate channels as it receives a high frequency input. His circuitry logically ANDs the user and synch inputs, so the order in which they arrive at the timing box is irrelevant. For this reason, a separate latching circuit was built which is activated by a user trigger, then outputs the next synch pulse to arrive before resetting. The output of this circuit can then be input to the user-trigger of Dewhirst's timing box, which results in the required pulse train being sent to the framegrabber. The framegrabber uses these pulses to provide the appropriate signal (negative TTL pulse) for the camera to expose.

This timing box was designed for Dewhirst's 4-camera system. If, however,

the flow under investigation is sufficiently slow, it is possible to perform PIV with a single TM9701, whose frame rate is 30 frames per second. It was found that around $3s$ after the breaking wave, the fluid motion was indeed slow enough for the PIV to be conducted with just one camera. The outputs from Dewhirst's timing box corresponding to cameras 1, 2 and 3 were then logically ORed, and used to trigger the single camera.

The essence of the circuitry used in the dual-plane PIV experiments is shown in figure 8.4. The latching circuit, whose main component is a 7474 flip-flop, passes the first synch pulse to follow a user-trigger, coloured magenta in the diagram. The first four aperture pulses to reach the timing box following an output pulse from the latching circuit are output on channels 1 to 4 respectively. The OR gate required when a single camera is used is not shown.

Due to the number of electronic components, it was necessary to amplify the pulses at various points using transistors. Furthermore, it was found that there were high frequency spikes in the pulse train due to electronic noise which resulted in spurious trigger signals being detected by the frame-grabber. These impulse signals were removed using a low-pass filter with a cut-off frequency of $10kHz$.

To test that the timing electronics described above did trigger the camera channels as required, the camera was focussed to image the SMD. The resulting, slightly blurred, images are shown in figure 8.5.

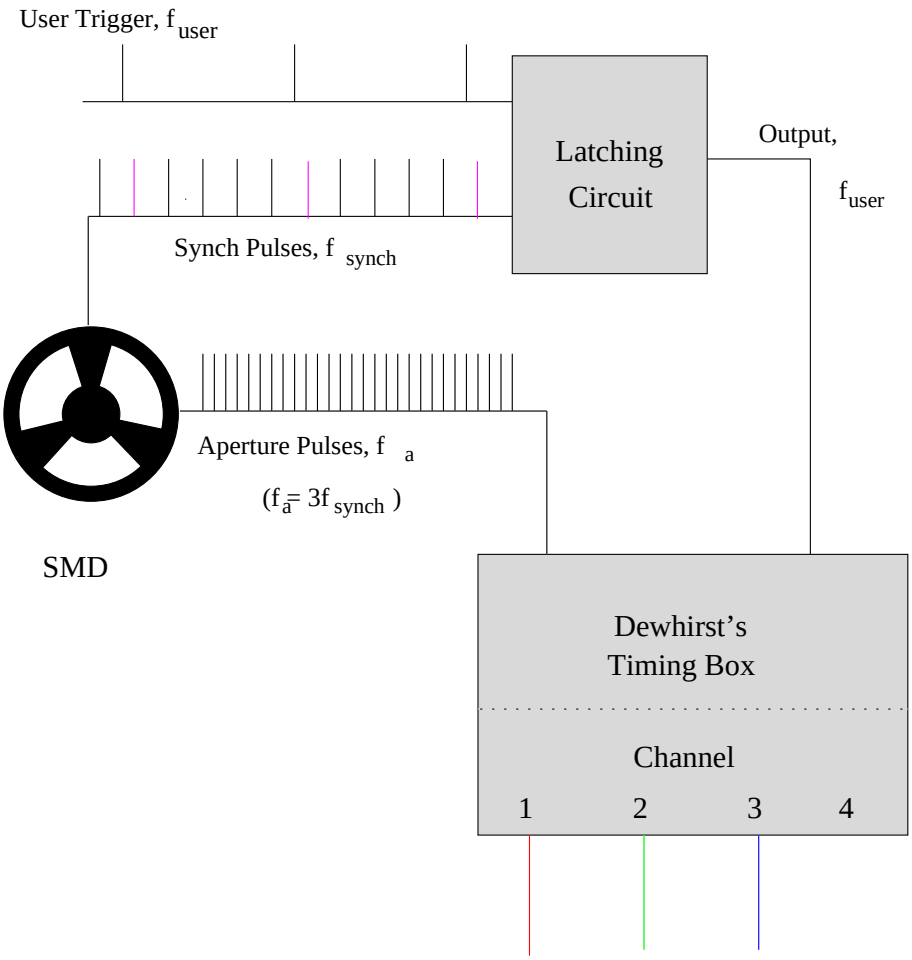

Figure 8.4: Timing Circuitry

The SMD was rotating anti-clockwise at $25Hz$. The glass aperture is opposite the white circle in the image, which corresponds to the counter-weight, coated white for clarity. The images are thus in the appropriate order. The effect of the glare in the second image, due to scattering of the laser light by the glass, will be discussed in section 8.6.

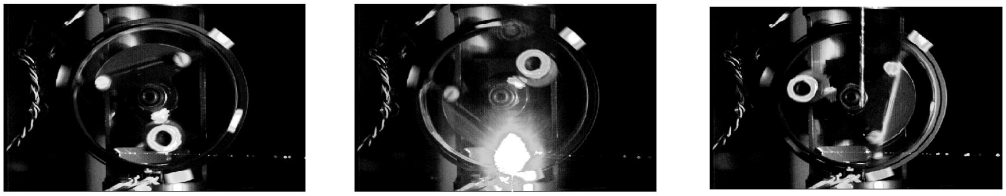

Image 1 Image 2 (Glass) Image 3

Figure 8.5: Images of rotating SMD

8.2.3 Measurement of the Beam Profile

The dual-plane software assumes that the profile of the laser beam is Gaussian in shape, and requires the $\frac{1}{e}$ width of the beam and the displacement caused by the glass to calculate the out-of-plane component.

The beam profile was measured using an Argon Ion Power Meter positioned behind a $0.1mm$ wide slit mounted on a translation stage; see figure 8.6. Starting at the edge of the beam, the slit was moved in $0.1mm$ increments and the intensity of the light which reached the power meter at each position was recorded.

A Gaussian curve of the form

$$y = 115e^{-0.6(x-2.95)^2} + 25 \tag{8.2}$$

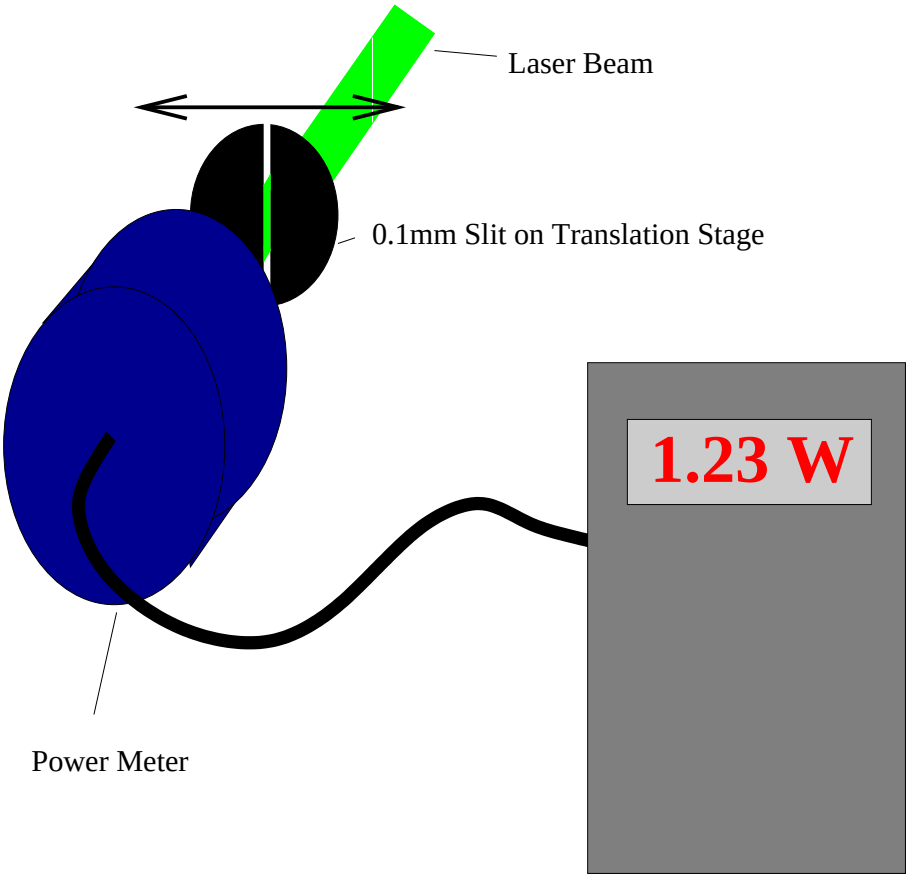

Figure 8.6: Measurement of Beam Profile

was fitted to the measured power values. The measured beam profile is Gaussian to a good approximation, especially near the centre of the beam. The intensity does not fall off to zero at the edges due to scattering off the slit holder.

Comparing equation 8.2 to the definition of the laser profile in equation 4.14 leads to

$$\frac{4}{\Delta z^2} = 0.6 \tag{8.3}$$

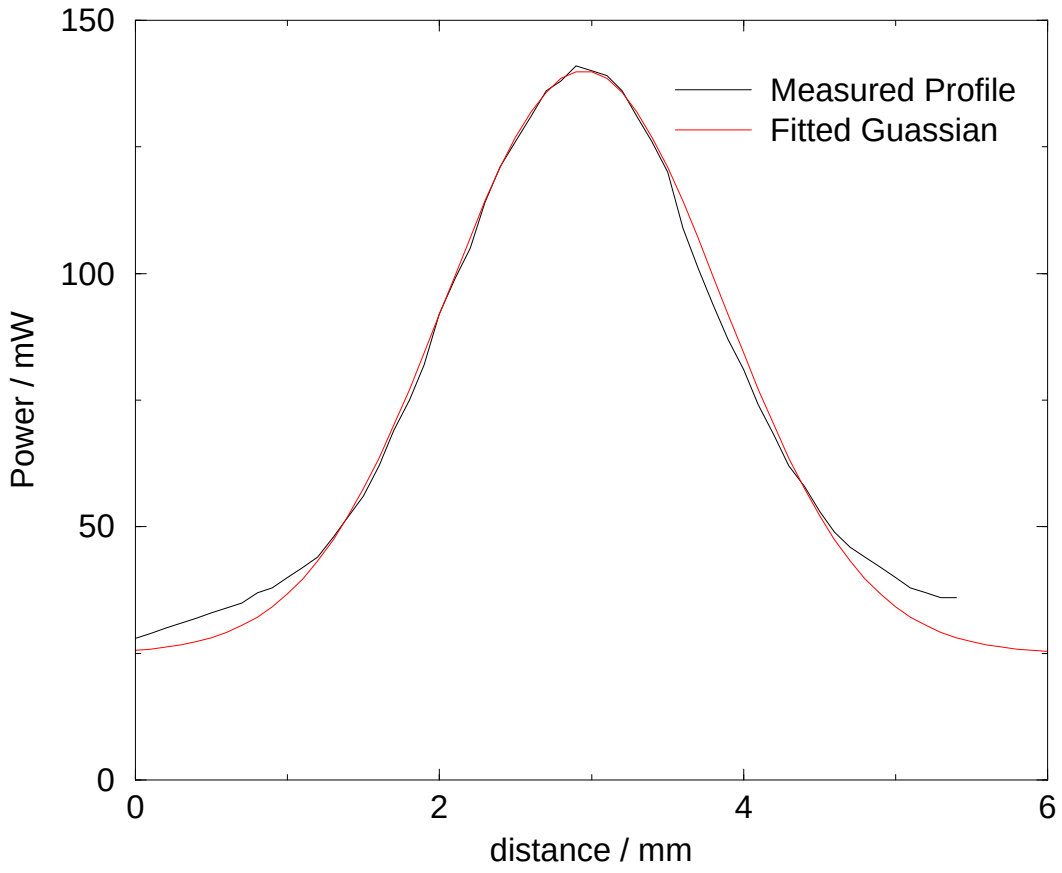

Figure 8.7: Argon Ion Laser Beam Profile

where Δz is the $\frac{1}{e}$ diameter of the laser beam. Rearranging 8.3, it can be seen that Δz is equal to approximately $2.6mm$. The lenses used to collimate the laser beam were $+200mm$ and $-50mm$, which, according to the lens equations in section 2.3 should produce a beam of diameter $1.5mm$. This discrepancy is due to diffraction of the laser beam, which was not allowed for in the lens equations.

8.3 Dual-Plane PIV Results

Much research into two-dimensional post-breaking water motion has already been conducted at Edinburgh (e.g. [14], [5], [77]), so the results presented will focus largely on the out-of-plane measurements.

The breaking wave used in these experiments had a non-dimensional amplitude of $ak = 0.352$, central frequency $0.88Hz$ and frequency spread $0.6424Hz$, that is, the same parameters as the largest amplitude breaker studied in the LIF experiments.

During of the testing of the dual-plane PIV software, it was noticed that there were occasionally obviously unrealistic out-of-plane velocities i.e. greater than the lightsheet width. On inspecting the correlation planes, it was noticed that these tended to occur when there was a good correlation between one pair of images and a poor correlation between the other pair, caused, for example, by an insufficient number of tracer particles due to a random fluctuation in the seeding density. This problem was avoided by introducing an additional criteria into the analysis algorithm: the out-of-plane velocity, determined using equation 4.16, was calculated if *both* of the correlation peaks exceeded a threshold value; otherwise the z displacement was set to zero. The threshold value used in the analysis was 0.25. Thus the z displacement, D_z was evaluated via

$$D_z = \begin{cases} \dfrac{\Delta z^2(\ln R_{01} - \ln R_{12})}{8(Z_1 - Z_0)} & \text{if} \quad \mathrm{R}_{01} > 0.25 \quad \text{and} \quad \mathrm{R}_{12} > 0.25 \\ 0 & \text{otherwise} \end{cases} \tag{8.4}$$

where $\Delta z = 2.6mm$ and $Z_1 - Z_0 = 1mm$, and R is the height of the normalised correlation peak.

Two sample vector maps are shown in figure 8.8. The raw images used to obtain these vector maps were taken with a single Pulnix camera, $40ms$ apart and with an exposure time of $5ms$. The vector maps represent the flow $5s$ and $40s$ after breaking respectively. The field of view of the camera was approximately $17.5cm$ by $13cm$.

In the first vector map, the vectors appear to be roughly equal in both direction and magnitude, corresponding to motion within a large-scale eddy. As time passes, the energy contained within this eddy cascades to smaller and smaller scales, resulting in the formation of smaller vortices. The vectors in the second vector map reveal some of these vortices.

A sample correlation is shown in figure 8.9, for the interrogation area enclosed by the white square near the bottom of the first vector map. The interrogation areas from the raw images are shown at the top of the figure, with the corresponding correlation plane drawn below.

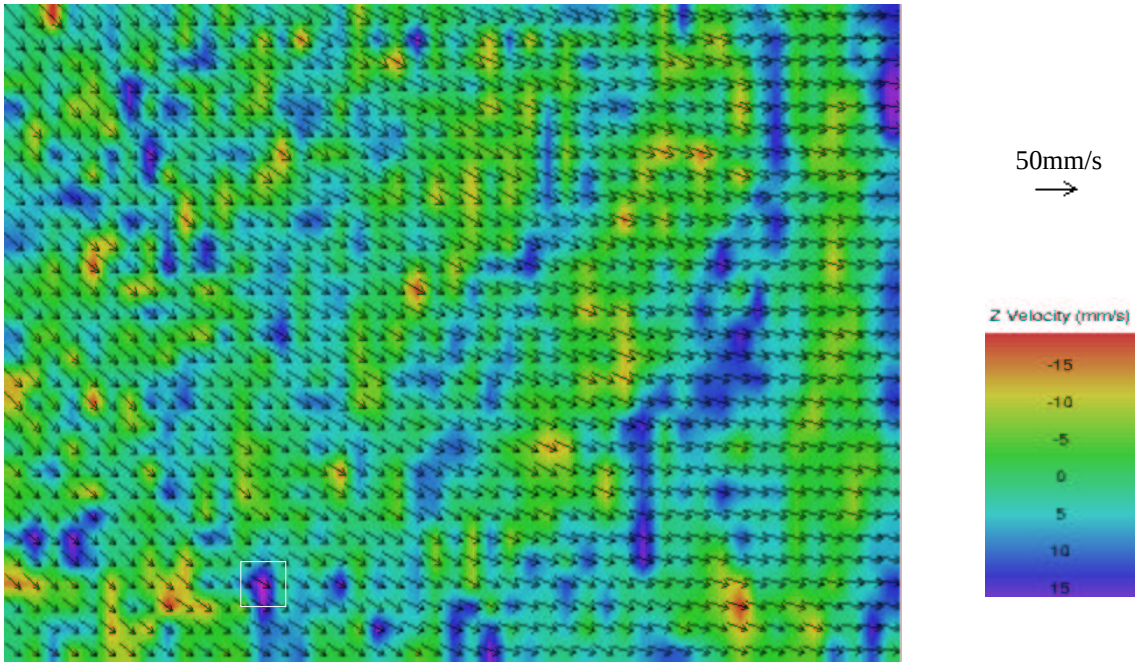

Five seconds after breaking

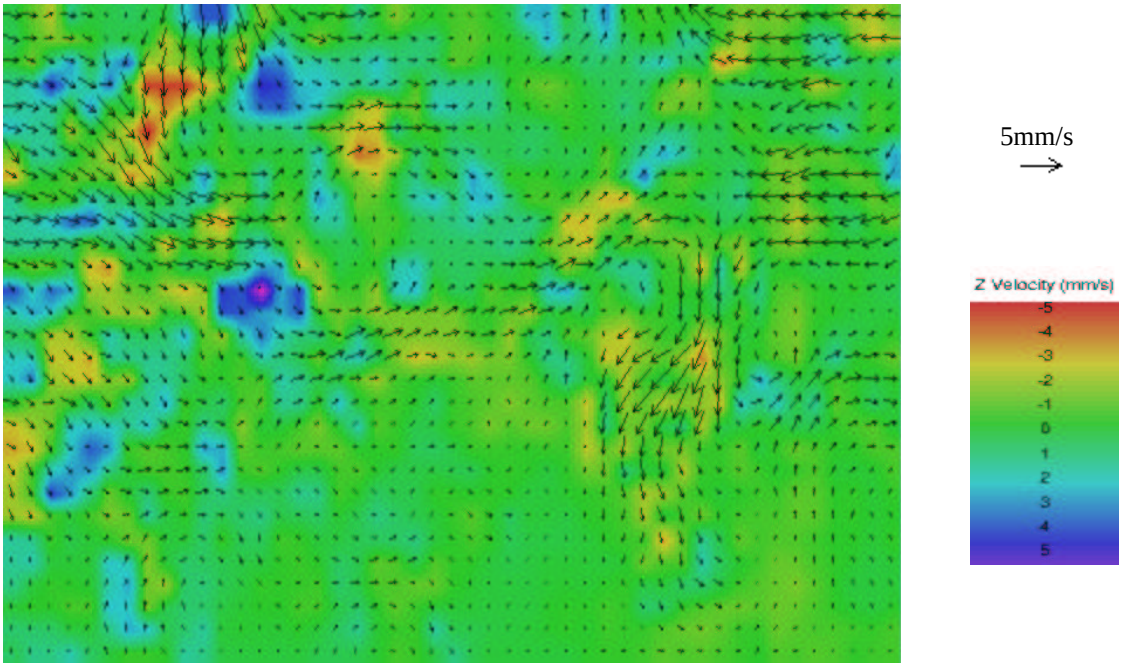

Forty seconds after breaking

Figure 8.8: Sample Dual-Plane Images

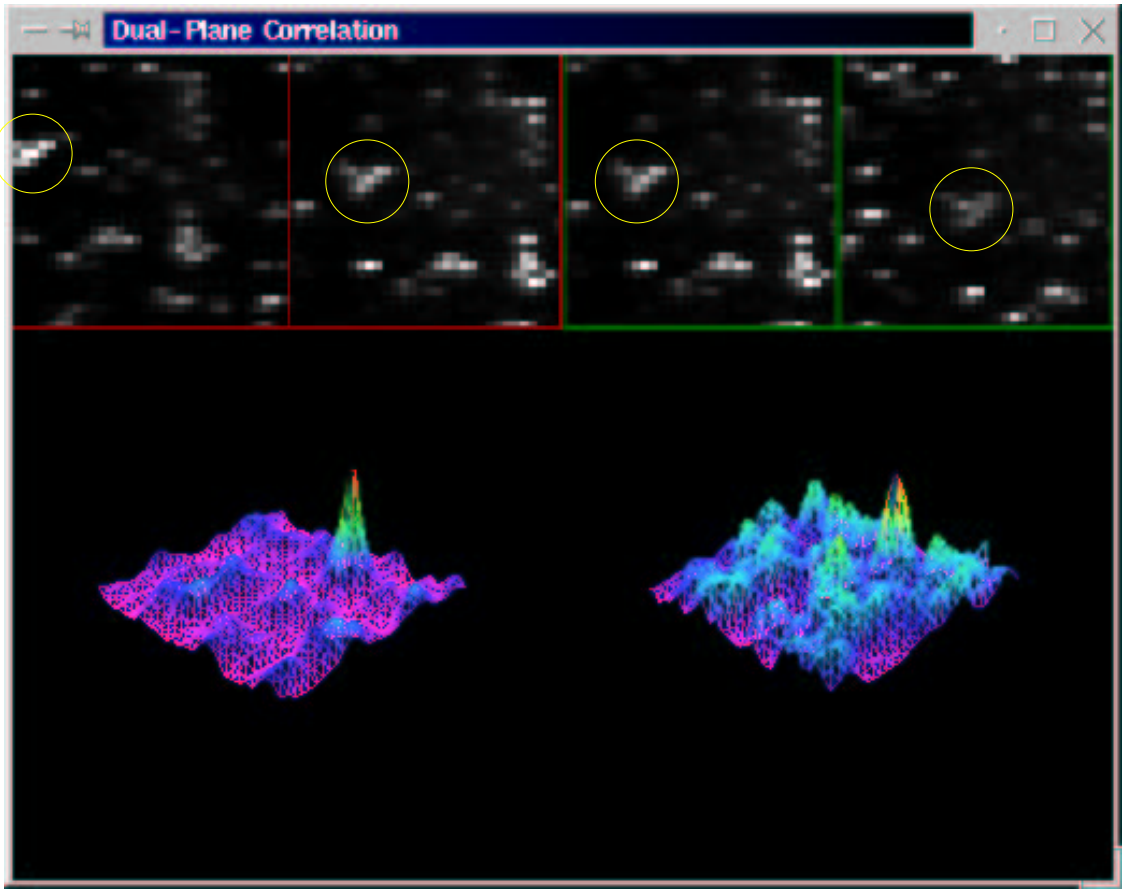

Figure 8.9: Interrogation Areas and their Correlation Planes

Consider the particle within the yellow circle. Clearly, it is moving downwards and to the right between images, as indicated by the arrow in the vector map. The particle, which was bright in the first image, is still bright in the image taken in the displaced lightsheet. However, its brightness is much less in the final image, taken in the original lightsheet. This suggests that the particle is moving in the direction in which the lightsheet was displaced, defined as the positive z direction. The peak obtained from correlating the first two images is therefore

larger than the corresponding peak from the second and third images, resulting in a positive z displacement.

Note that the vector scale in the second map is ten times smaller than the corresponding scale in the first map. The extreme values of the z velocity are approximately five times smaller in the second vector map.

It would appear, therefore, that both the in-plane and out-of-plane velocities decay after wave breaking, but that the out-of-plane velocity decays more slowly. This can be seen in figure 8.10, which shows the *rms* velocity of the three components as a function of time. As before, time is non-dimensionalised by multiplication with the central angular frequency, ω_c. The velocities are non-dimensionalised by dividing the actual velocities by the celerity of the central frequency component, $c = \frac{\omega_c}{k_c}$.

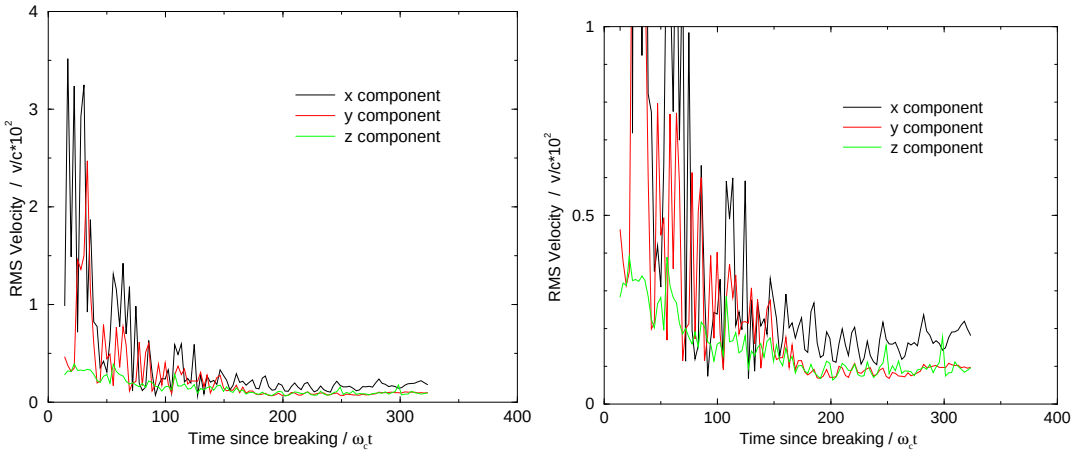

Figure 8.10: Graph of RMS Velocities, with close-up

Shortly after breaking, the x and y velocity components are large relative to the z component, The in-plane components decay rather rapidly, and around $30s$ after breaking ($\omega_c t \sim 170$), all three components are of similar magnitude.

The relative importance of the in-plane and out-of-plane velocities is of particular interest to this project. For this reason, the ratio of the root-mean-square (rms) out-of-plane velocity to the rms in-plane velocity, that is

$$\frac{\sqrt{\sum vz^2}}{\sqrt{\sum vx^2} + \sqrt{\sum vy^2}} \tag{8.5}$$

was plotted against time, where vx, vy and vz are the x, y and z velocity components respectively. This graph is shown in figure 8.11.

If the three velocity components were equal, this ratio would equal 0.5; if there were no out-of-plane motion, the ratio would equal zero. Although sharp peaks are present in the graph, the ratio does initially increase with time, indicating that the fluid velocity becomes more three-dimensional after breaking.

The graph of rms velocity against time, figure 8.10, reveals that there are rather large fluctuations in each of the component velocities. These are due to factors such as the oscillating water surface shortly after breaking, and the movement of eddies into and out of the field of view of the camera. It is believed that these fluctuations are responsible for the peaks in figure 8.11: a peak will occur if a higher out-of-plane velocity is recorded at the same time as a lower

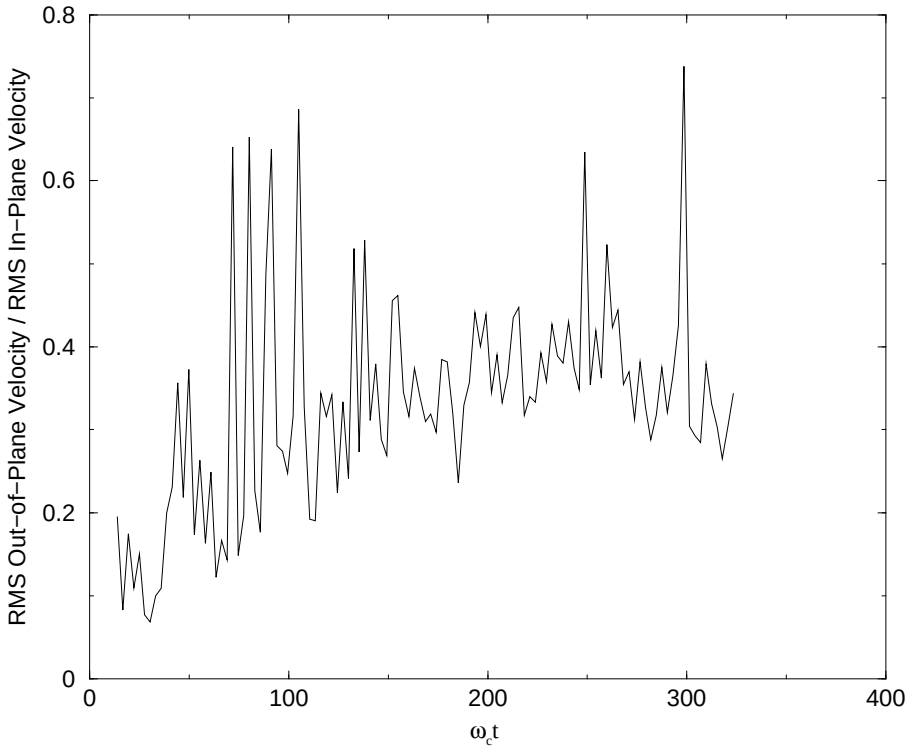

Figure 8.11: Graph of $\frac{\text{RMS Out}-\text{of}-\text{Plane Velocity}}{\text{RMS In}-\text{Plane Velocities}}$ against time

in-plane velocity.

This experiment was repeated 5 times, and the average value of the ratio of out-of-plane to in-plane motion is plotted in figure 8.12, together with the standard deviation and a best fit curve. The variance of the curve is large, despite the data files being validated with a local-median filter to remove the sharpest peaks, discussed above. Nevertheless, there is a clear upward trend from below 0.1 to approximately 0.5, indicating that the relative magnitude of the out-of-plane motion increases after wave breaking until all three components are comparable.

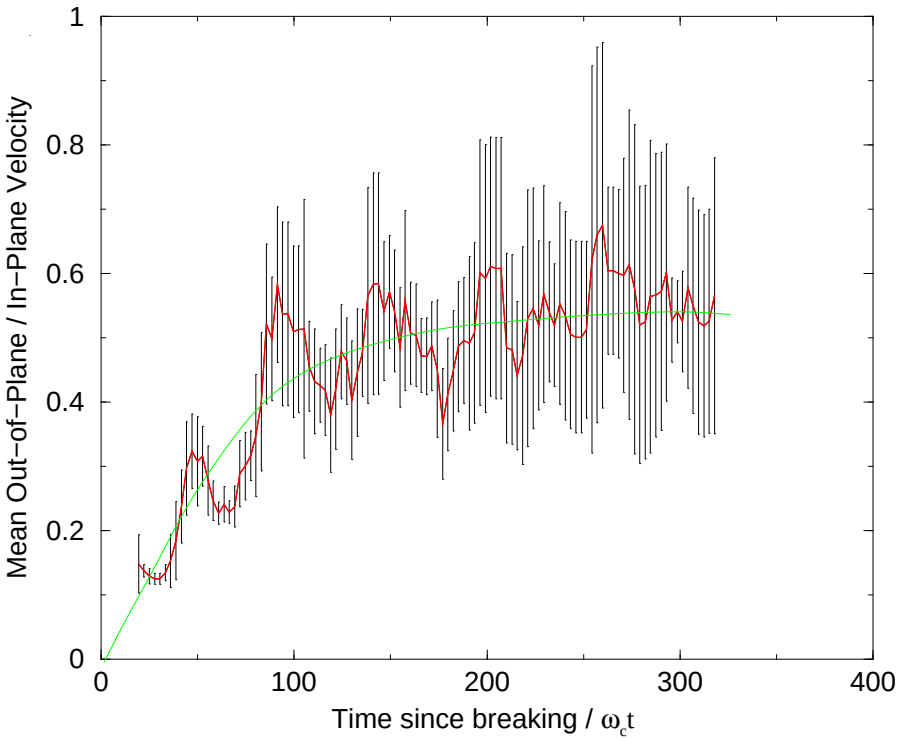

Figure 8.12: Graph of Mean $\frac{\text{RMS Out}-\text{of}-\text{Plane Velocity}}{\text{RMS In}-\text{Plane Velocities}}$ against time

8.4 Power Spectra

The transition from 2d to 3d motion after breaking has been investigated by several researchers in terms of the *power spectrum* of the turbulent velocities. The power spectrum describes the energy content of a stationary, random function as a function of frequency. Theory predicts that the spectral form depends on the nature of the turbulence [78]. In two dimensional turbulence, the energy spectrum $E(k)$ is of the form

$$E(k) \propto \epsilon^{\frac{2}{3}} K^{-3} \tag{8.6}$$

where ϵ is the energy transfer rate per unit mass and K is the wave number.

In three dimensional turbulence, however, Kolmogorov's $-\frac{5}{3}$ law applies in the inertial subrange of wavenumbers, and the spectrum is

$$E(k) \propto \epsilon^{\frac{2}{3}} K^{-\frac{5}{3}} \tag{8.7}$$

The exponent can be determined by plotting a graph of $log\ E$ against $log\ K$. Evaluating E involves squaring the modulus of the Fourier Transform of the velocity function, as described in [14].

Lemmin et al. [12] measured a transistion in the slope of the energy spectrum graph from -3 to $-\frac{5}{3}$ in velocity measurements beneath breaking waves on Lake Ontario. In particular, they found that this change occurs after the energy source is exhausted.

Battjes and Sakai [79] produced a steady breaker by submerging an angled hydrofoil in a mean flow. They measured the energy spectra as a function of position relative to the breakpoint, and found that the power law exponent was -3 near the breakpoint and $-\frac{5}{3}$ further downstream. Using the mean velocity to convert these distances to times, their results suggest that the transition in the

exponent value occurs within the first second after breaking.

More recently, Haydon [14] measured the energy spectra of horizontal velocities obtained using an auto-correlation PIV system, both as a function of time and location. He found that the gradient was steeper in regions where there were clear 2d vortex structures, and less in areas where the motion appeared more three dimensional. There was no obvious correlation between the value of the exponent and time since breaking from his results.

Using his analysis program, spectra for the 3d vector maps obtained using dual-plane PIV were calculated. As Haydon found, many of the spectra were noisy: flow features were observed to move into and out of the field of view of the camera, so the assumptions that the velocity function is stationary and random are dubious. A graph of the averaged exponent as a function of non-dimensionalised time, with rather large error bars, is shown in figure 8.13.

It can be seen that the exponent is approximately uniform throughout the experiment; if anything, the exponent decreases slightly with time. The average value for the exponent is -1.74 ± 0.04, close to the theoretical exponent for three dimensional turbulence. The earliest calculated exponent corresponded to $3s$ after breaking, which is consistent with Battjes et al. As will be discussed in the following section, it was not possible to obtain velocity maps closer to breaking.

Thus other researchers have inferred a transition from 2d to 3d motion after

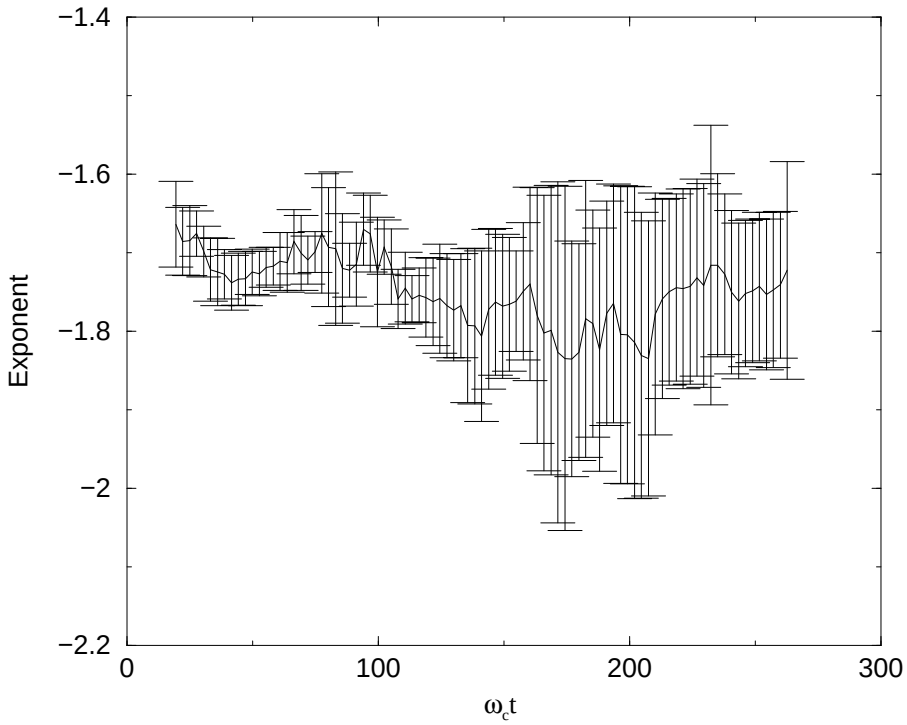

Figure 8.13: Graph of Spectral Exponent against Time

wave breaking by measuring a change in the exponent of the energy spectrum. The exponents obtained from these vector maps also suggest that the flow after breaking is three dimensional. However, in order to relate the calculated spectral exponent to the degree of isotropy, quantified in this thesis as the ratio of rms out-of-plane to rms in-plane motion, it would be necessary to obtain vector maps of a much larger region of mixing than has been done so far.

8.5 Dual-Plane PIV with 4-Camera System

Approximately $3s$ after breaking, the flow was sufficiently slow for dual-plane PIV to be performed using a single camera. Attempts were made to obtain 3d velocity measurements at breaking using the 4-camera system described in chapter 5 using a frame separation of $15ms$, but unfortunately these were unsuccessful.

The Pulnix TM-9701 cameras have an uncertainty of $5\mu s$ in their trigger response, so even triggering the cameras $1ms$ apart would result in a timing error of less than 1%. This is more than sufficient to obtain accurate velocity measurements at breaking.

The problem was that it was necessary to expose the cameras for considerably longer than this in order to obtain enough light. Even with an exposure time of $10ms$, twice that for the single camera experiment, regions of the image were still rather dark, for reasons discussed in section 5.5. The effect of this was that, around breaking, the image of a tracer particle was a streak (actually a line of dots due to separate scans of the laser beam), as can be seen in figure 8.14.

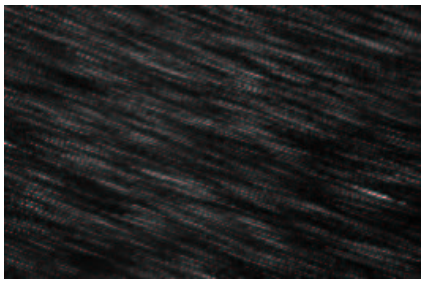

Figure 8.14: Blurring of Tracer Particles

Several seconds after breaking, the flow has slowed sufficiently such that good

correlations can be obtained using the 4-camera system. However, by this time it would be possible to revert to using the single camera once again, which avoids the need for compensating for image misalignment.

In order to use the 4-camera system for performing dual-plane PIV on flows faster than can be recorded with a single camera, it would be necessary to reduce the exposure time. This could be done if a more powerful laser and/or tracer particles better at scattering light than pollen were available. Alternatively, more sensitive cameras could replace the TM-9701s in the 4-camera system or, better still, smaller cameras were available such that the camera system could be rebuilt using a standard SLR lens.

Thus, although the 4-camera system could be used for dual-plane PIV, the illumination restriction limited the flow velocities it could record to those which a single Pulnix camera could measure.

8.6 Uncertainties in Dual-Plane PIV Results

In addition to the errors mentioned in chapter 4, there were a number of experimental artefacts which tended to increase the uncertainty in the values obtained for the out-of-plane motion. Some of these will be discussed in this section.

After passing through the sheet moving device, the laser beam is reflected off

three mirrors before passing through the glass tank bottom and $0.75m$ of water. For practical reasons, it was not possible to measure the beam profile in the region of interest; instead, the profile was recorded in air a comparable distance from the SMD. It is anticipated that the effect of this will be to underestimate the beam width.

The dual-plane correlation algorithm assumes that the beam profile is identical in both the original and displaced positions. However, as can be seen in figure 8.5, considerable scattering occurs when the laser passes through the glass aperture of the SMD. This has the effect of reducing the brightness of the displaced lightsheet, and may also affect the beam profile. It was not possible to measure the profile with the glass aperture in place due to a malfunction in the power meter.

While the problem mentioned above could be reduced by appropriate coating of the aperture glass, there is a more serious difficulty with the SMD. As mentioned before, the disk with the three apertures is rotated by a stepper motor. The size, and therefore the power of this motor, is limited by space constraints. In order to accelerate the disk from rest to the rotation rate determined by the pulse train to the Stepper Motor Driver, it was necessary to have a clutch mechanism within the motor shaft. The slack required for this clutch resulted in a slight wobble in the rotation of the aperture disk. The effect of this was to change the angle between the laser beam and the glass which in turn caused a shift in the lightsheet displacement. Not only did this introduce an error into the measured

lightsheet displacement, but the lightsheet actually moved during the exposure of the middle image of the PIV triplet.

This difficulty is less serious if the exposure time is short relative to the time taken for the glass aperture to pass by the laser beam, Δt. The resulting error will therefore be less for slow flows illuminated by intense light. For the experiments carried out using a single camera, the exposure time was only $\frac{1}{8}th$ of the frame separation, so it is not anticipated that the lightsheet would move significantly during this time. In the experiment involving the 4-camera system, however, the ratio of exposure time to frame separation was $\frac{2}{3}$, so there was significant movement of the displaced lightsheet during the exposure. This is a further reason why it would be necessary to increase the sensitivity of the 4-camera system before it could be used to obtain accurate measurements of faster flows.

It was not possible to accurately quantify the uncertainty in the out-of-plane displacement, though it was certainly larger than the in-plane error, of the order of 0.1 pixels. Nevertheless, the result obtained – that the relative importance of the out-of-plane to in-plane motion grows until all three velocity components are comparable – is certainly plausible.

The technique of dual-plane PIV was tested further by performing a contrasting control experiment: the motion of a non-breaking sinusoidal wave motion. The results from this experiment are presented in the following section.

8.7 Out-of-Plane Motion in Non-Breaking Waves

Dual-Plane measurements were taken of a sinusoidal wave motion of frequency $0.88Hz$, the central frequency of the breaking wave packet. The experiments were started after the initial ramp-up of the paddle, and the wave generation was stopped after $30s$. Two PIV image triplets were captured each second, for a total of $60s$. The mean and rms velocity components as a function of time are shown in figure 8.15.

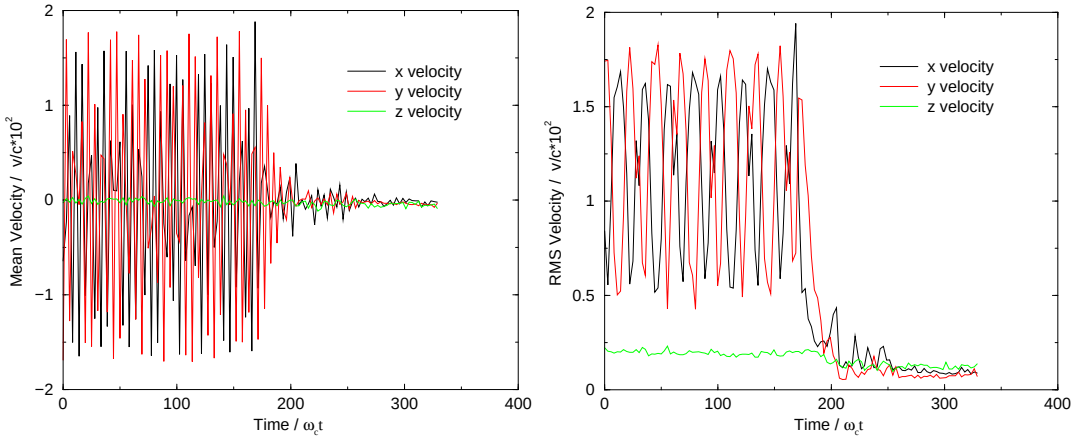

(a) (b)

Figure 8.15: Mean (a) and RMS (b) Velocity Components against Time

Throughout the experiment, the mean of all three velocity components is oscillating about zero. During the first $30s$, when the paddle is generating sinusoidal waves, the rms x and y velocity components are oscillating out-of-phase, while the rms z component is small but finite, and relatively uniform. After the paddle is stopped, all three velocity components decrease until they are approximately

equal.

The ratio of the out-of-plane rms velocity to the in-plane rms velocities for five repeats of this experiment is shown in figure 8.16.

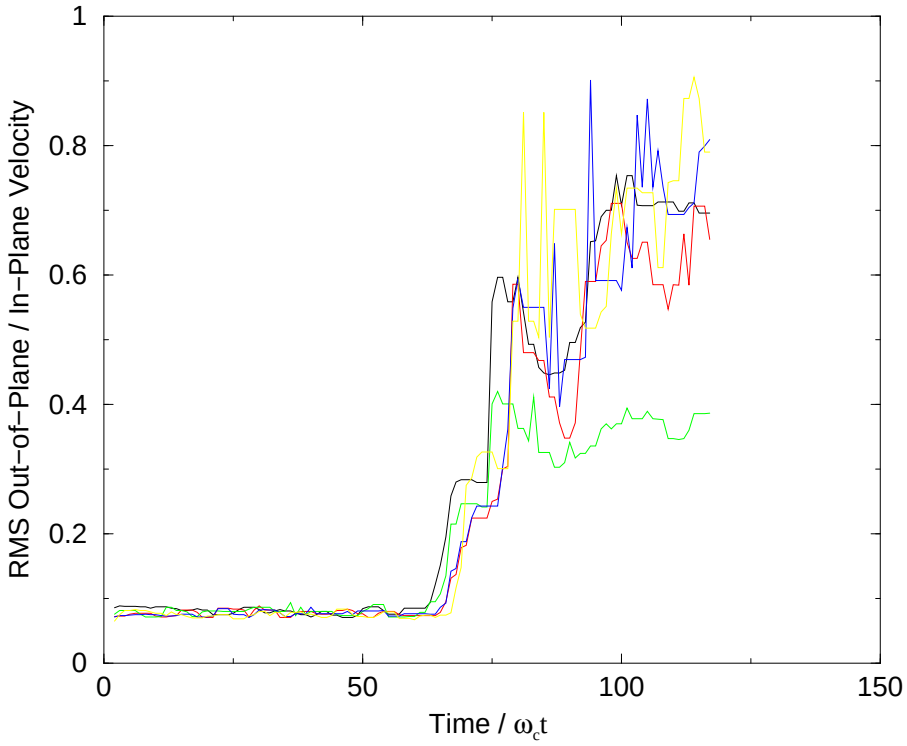

Figure 8.16: Out-of-Plane vs In-Plane Velocity against Time

As before, the data has been median filtered to remove the most extreme spikes, which were caused by ill-conditioning, as one small number was divided by another. In the presence of the sinusoidal waves, the ratio of out-of-plane to in-plane velocity is less than 0.1. As these waves decay, this ratio increases until all three components are of the same order.

The trajectory of a fluid element under such a wave correponds to the inter-

mediate depth scenario of figure 1.5 i.e. the motion is theoretically a combination of elliptical and circular motion, with no out-of-plane component. That the measured z component was non-zero implies that there is an asymmetry in the experiment; this could be caused by reflections off the end of the tank, cross-waves generated by non-parallel tank walls or a slight skewness in the paddle.

Nevertheless, this z component is small compared to the in-plane motion, and to the the out-of-plane motion measured after wave breaking, providing further evidence that the velocities obtained via the technique of dual-plane PIV are reasonable.

8.8 Relating PIV to LIF Measurements

The purpose of conducting both PIV and LIF experiments was to determine the relationship between the motion of the water after breaking and the dispersion of a surface film. Due to time constraints, however, it was not possible to obtain velocity measurements of the entire region in which dispersion of a surface film occurs, so a detailed comparison is impractical at this stage. Nevertheless, in this section an attempt to relate a result obtained from the LIF experiments to a result from this chapter will be proposed.

One effect of wave breaking is that the fluid motion evolves from an essentially 2d flow to a 3d flow. This occurs as the large eddy formed by the overturning

tip decays into smaller and smaller vortices, and was quantified using dual-plane PIV.

The interface between the rhodamine and the water after breaking was measured using LIF and was found to become increasingly contorted after breaking. This transition was believed to be due to the evolving turbulence and the energy cascade from large scales to small scales.

It is believed, therefore, that there must be a correlation between the increasing importance of the out-of-plane motion and the fractal dimension of the film outline. This was investigated by plotting the ratio of the out-of-plane rms velocity to the in-plane rms velocity, as depicted in figure 8.11 together with the increase in fractal dimension from unity. The graphs are shown in figure 8.17.

There does indeed appear to be a correlation, since both of the plotted parameters tend to increase rather rapidly at first before levelling off. Of course, more experiments would be necessary to establish the true relationship between these parameters. In particular, it would be necessary to obtain PIV measurements for the entire mixing region investigated using LIF.

8.9 Conclusions

The technique of dual-plane PIV was used to measure all three velocity components of water using a single camera. It was found that in non-breaking si-

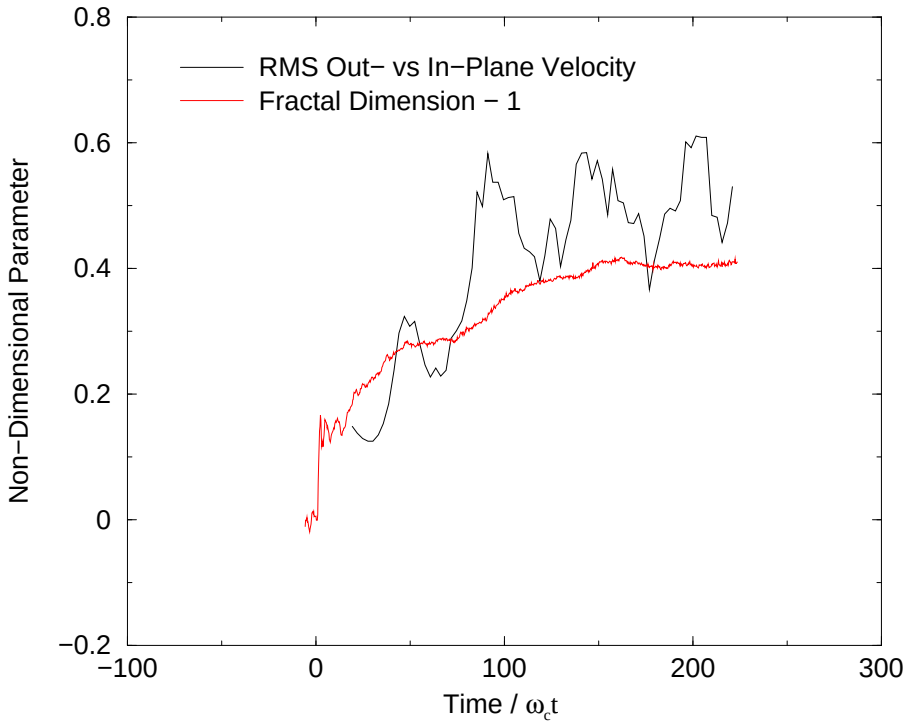

Figure 8.17: Out-of-Plane vs In-Plane Velocity and (Fractal Dimension -1) against Time

nusoidal waves, the ratio of the out-of-plane *rms* velocity to the in-plane *rms* velocities was less than 0.1. After wave breaking, however, this ratio increased from approximately 0.1 until the three components were approximately equal.

Chapter 9

Conclusions and Further Work

9.1 Review of Subject

Much of the world's open water is covered with surfactant material which both reduces and causes gradients in the surface tension of the water. The effect of these is to damp surface oscillations, particularly capillary waves, and this in turn reduces the energy transfer from the wind to longer gravity waves because the water surface is aerodynamically smoother.

Waves break and dissipate their energy via turbulence when the surface profile exceeds a critical steepness. The presence of surfactants can thus inhibit or suppress breaking completely. Although there are mechanisms by which surfactants disperse horizontally, they tend to remain on the water surface unless that

surface is broken, for instance by wave breaking. Surfactants therefore affect the mechanism primarily responsible for their dispersion beneath the surface.

The purpose of this research was to investigate the mixing of a surface film after wave breaking in a laboratory flume. The surface film consisted of a solution of $1g$ rhodamine B to $1l$ of methanol. Prior to breaking, the rhodamine/methanol solution remained on the surface as a thin film. Because the breaking event was caused by focusing gravity waves which are largely unaffected by surface tension, it was believed that the presence of the film had no discernible effect on the breaking process. Thus the rhodamine/methanol solution can be treated as a passive tracer which is driven by the motion of the water.

9.2 Experimental Techniques

The techniques of Laser Induced Fluorescence and Dual-Plane Particle Image Velocimetry were developed and used to obtain detailed concentration measurements of the rhodamine solution after breaking and the water motion responsible for this mixing.

9.2.1 Laser Induced Fluorescence

In the LIF experiments, a section of the wave flume, equidistant from each wall, was illuminated by a diverging laser lightsheet. LIF images of the spatial

distribution of a solution of rhodamine B and methanol were obtained simultaneously from two adjacent CCD cameras. These images were corrected for variation in the lightsheet intensity, calibrated such that their grey levels corresponded to known concentrations of the contaminant and combined into single, widescreen images. In each experimental run, 1000 such images were produced at a frame rate of $20Hz$.

From these widescreen images, various data were extracted using software written by the author. Specifically, the measured parameters were:

- Depth reached by material within film
- Area covered by material within film
- Motion of pollutant's centre of mass
- Dispersion coefficients and exponents
- Fractal Dimension of the contaminant-water interface

The repeatability of the dispersion after nominally identical breaking events and the effect of wave amplitude on dispersion were investigated. Furthermore, the LIF images were subjected to a PIV analysis, allowing the displacement of the concentration boundaries to be determined.

9.2.2 Dual-Plane Particle Image Velocimetry

Dual-Plane PIV was implemented to enable the measurement of all three velocity components of a breaking wave. This technique involves recording three images of tracer particles within the fluid, two in the original plane of the lightsheet, and a third in a displaced lightsheet. The lightsheet was displaced by a rapidly rotating angled disc which contained two air apertures and an aperture containing a piece of glass. Sychronisation electronics were designed to trigger an image when the appropriate aperture was in place.

The in-plane displacements were determined by locating the highest peak in the cross-correlation plane, and the out-of-plane displacement was found by comparing the normalised heights of these peaks. The PIV analysis software was written by the author.

The dual-plane experiments were carried out using a single Pulnix TM9701 camera, with a frame rate of $30Hz$. A 4-camera system consisting of a common imaging lens, a pyramid mirror and four CCD cameras was constructed to enable the technique to be applied to faster flows. The 4-camera system could produce a total of 120 images per second, or the individual cameras could be triggered in quick succession to record high-speed events. There was space for individual filters, allowing the possibility of performing simultaneous PIV and LIF. However, due to the lack of sensitivity of the CCD arrays, the lengthy exposure time required to record the tracer material adequately limited its applicability to slower

flows or experiments requiring less illumination.

9.3 Kinematics of Wave Motion and Dispersion

The tip of a plunging breaker creates an initial patch of film material beneath the surface which is stretched horizontally and vertically by the passing crests and troughs. A second distinct patch is formed downstream from the splash-up caused by impact of the overturning tip. These patches continue mixing both downstream and vertically downwards, rotating as they do so because of the large eddies formed by breaking. The spilling process occurs more gradually than a plunging event, so the resulting dispersion cloud is longer and shallower, and the presence of well-defined, individual patches is less obvious.

As the energy present in the vortices cascades to smaller and smaller scales, the boundary of the film material and the water becomes increasingly contorted. The "wiggliness" of the boundary was quantified by computing its fractal dimension, which increased from approximately unity around breaking to 1.3 for spilling and 1.4 for plunging breakers.

It was found that the gross parameters used to classify the concentration distribution of the contaminant were generally repeatable, but there were unpredictable variations in its precise shape. Measurements of the depth reached by the contaminant and the fractal dimension of its outline compared well with

related work.

Five different wave amplitudes, corresponding to breaking events ranging from weak spilling to strong plunging, were investigated. There was a clear distinction between the dispersion distributions caused by spilling and plunging: the area covered, depth reached and fractal dimension of the pollutant's outline were all significantly greater for plunging breakers. There were indications that these parameters were also larger for plungers of larger amplitude, though this result was less conclusive.

The film's velocity distribution was obtained using a standard PIV analysis routine, that is by cross-correlating images of the film taken a short time apart. The algorithm found the most likely displacements of the contours separating the different concentration bands. The vector maps revealed flow features such as the vortices produced by the breaking event and that the motion is stronger near the water surface.

The in-plane velocity vectors obtained from the PIV experiments also revealed the turbulent energy cascade, by which smaller vortices evolve from the large scale eddies created by the breaking event. All three velocity components decreased in magnitude after breaking, though the decrease was larger for the in-plane velocities. The relative importance of the out-of-plane to in-plane motion was quantified in terms of the ratio of the out-of-plane rms velocity to the sum of the in-plane rms velocities. It was found that in non-breaking waves, this ratio was

less than 0.1 whereas after breaking it increased from 0.1 to approximately 0.5. Prior to breaking, therefore, the water motion is largely two-dimensional, but the evolving turbulence after breaking results in three-dimensional motion, where all three velocity components are comparable. This transition from 2d to 3d motion was predicted from theory and measured by other researchers using less direct techniques.

9.4 Further Work

Much time has been spent designing the experiments, constructing the apparatus and writing the analysis software described in this thesis. For this reason, it was not possible to conduct a statistically significant number of LIF trials, or to obtain PIV measurements of the entire region of dispersion.

The LIF experiments carried out have hinted that there is a positive correlation between the amplitude of the breaking wave and dispersion parameters such as the depth reached and area covered by the contaminant, and the fractal dimension of the contaminant-water boundary. However, variations between supposedly identical experiments, due to small differences in the initial conditions, mean that any apparent trends cannot be confirmed. The next stage in this research would be to conduct a number of repeats to investigate the relationship between the wave amplitude and the dispersion parameters further.

A large number of other factors will also affect the film dispersion, and these too could be studied. The chemical composition of the film, its thickness, the frequency parameters of the wave, wind, currents in the water and beach slope will all influence the mixing process to a greater or lesser extent. One particularly relevant avenue of research would be to investigate the film dispersion due to a train of breaking waves on a beach, as this problem is closely related to oil-spill contamination on the coastline.

The dual-plane PIV method was applied to a single subsection of the region of interest in this project; an obvious extension would be to investigate the 3d motion of the entire area imaged in the LIF experiments. A comparison of the PIV velocities obtained from the tracer images and the velocities obtained by correlating the concentration contours in the LIF images would help determine the degree to which the contaminant is driven by the water motion. Further experiments would also promote understanding of the complex relationship between the evolving out-of-plane motion, energy transfer to smaller scales, turbulent mixing and fractal nature of the pollution distribution.

The mixing of a surface film due to breaking waves is a beautiful and environmentally significant process, which offers numerous possibilities for further research in the future.

Appendix A

Image Formation by a Lens

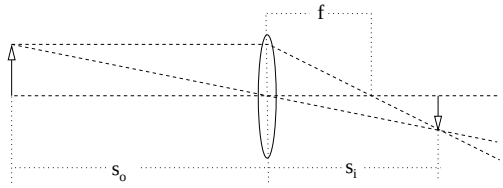

Figure A.1: Image Formation by Lens

A lens refracts the light from an object to produce an image. If the distance from the object to the optical axis of the lens is s_o and the lens has a focal length f, then the distance s_i from the optical axis to the image plane is given by:

$$\frac{1}{f} = \frac{1}{s_o} + \frac{1}{s_i} \tag{A.1}$$

Even neglecting the effects of diffraction, the image produced by a single lens is not geometrically similar to the object due to aberrations. There are seven first-order aberrations: axial and lateral (both chromatic aberrations), astigmatism,

coma, distortion, field aperture and spherical (monochromatic, also known as Seidel, aberrations). These can be removed by using lenses in combination; a minimum of three lenses is required to eliminate all first order aberrations.

To improve image quality, a camera lens therefore consists of a number of optical components. This combination can be considered to be a perfect lens of focal length f, even though none of the lens elements may have this particular focal length. The distances s_o and s_i are measured from the back principal plane of this lens.

For convenience, the camera lens is generally mounted a fixed distance from the image plane where the film is located. This distance is known as the back focal length, and is approximately $42mm$ for a standard SLR lens, or $80mm$ for a Hasselblad lens. To focus the camera, the location of the effective lens must be moved either towards of away from the image plane. When focussed, the magnification of the resulting image, M, is as follows:

$$M = -\frac{s_i}{s_o} \tag{A.2}$$

Since both s_o and s_i change as the effective lens position changes, it is convenient to consider the distance from the image plane to the object plane, L. The minimum value of L for which a real image is formed is $4f$. For given values of L and f, there are two symmetric lens positions at which a focussed image is

formed. For a camera, the solution where $s_i < s_o$ applies.

In this case, the magnification is

$$M = \frac{1 - \sqrt{1 + 4\frac{f}{L}}}{1 + \sqrt{1 + 4\frac{f}{L}}}, \qquad \frac{f}{L} < \frac{1}{4} \tag{A.3}$$

The magnification is negative because the image is inverted; its magnitude increases with increasing f and decreasing L.

Another useful lens parameter is the angular field of view of the lens, φ. This is defined as

$$\varphi = 2 \arctan\left(\frac{r}{2f}\right) \tag{A.4}$$

where r is the size of the image plane taken across the diagonal. The angular field of view is therefore inversely related to the magnification.

Choosing a suitable lens for an application generally involves a compromise between field of view and resolution.

Appendix B

Vector Validation

The velocity vectors obtained from PIV experiments are calculated using the cross-correlation function, as described in section 4.5. The velocity vectors produced are either accurate measurements with an associated error, or do not represent the flow at all. Spurious vectors, or *outliers*, are physically unrealistic, either of extreme velocity or unexpectedly different from their neighbours. Such vectors can be produced if an interrogation area contains insufficient or excessive seeding particles, strong velocity gradients are present in the flow, or a large out-of-plane motion exists [80], which would result in the correlation routine identifying a spurious peak. Even in a carefully controlled experiment, up to 5% of vectors may be outliers; factors such as turbulence in the flow, lens or mirror distortions, can increase this fraction substantially [43].

The presence of outliers is undesirable: they contaminate the vector map,

obscure valid features of the flow and can distort calculations of flow parameters such as vorticity and shear. These spurious vectors are readily detected by the eye. However a single PIV experiment can result in several hundred or more vector files. It would be tedious and time-consuming to validate each vector map by eye, and the validation criteria would be subjective and inconsistent. Hence there is a need for a validation algorithm capable of identifying and deleting outliers, and replacing them with more realistic velocity values.

In this appendix, several approaches to vector validation are described, and some difficulties discussed.

B.0.1 Mean and Median Validation Algorithms

Two commonly used methods compare the velocity of a vector to the *local mean* and *local median* velocities. If the difference between these velocities is less than critical value, a user-defined tolerance, the vector is judged to be valid. Otherwise, the vector is considered to be an outlier and, if required, replaced by a more plausible vector.

The size of the *local* region is generally taken to be a 3×3 matrix i.e. the eight nearest neighbours of the test vector are included in the calculation.

The main drawback of the mean validation algorithm is that the velocity which the test vector is compared to is the mean of *all* nearest neighbours, even

if they are outliers. Since an outlier has an extreme velocity, its presence in the calculation of the mean has the effect of shifting the mean velocity away from a physically realistic value. The presence of a single outlier may not corrupt the average sufficiently to affect the testing of a vector. If, however, a number of outliers are clustered together, then the value of the mean velocity may be such that a valid vector is rejected or, which is worse, an outlier is validated.

The median is the n^{th} of $2n+1$ values arranged in ascending or descending order. Unlike the mean, the median is nonlinear in that it does not depend on the absolute values of the extreme velocities, just their relative magnitudes. Since an outlier is unlikely to have the median velocity of the matrix containing the relevant vector and its nearest neighbours, its magnitude will not affect the validation condition of the test vector. Thus the median validation algorithm is generally successful, unless there is a cluster of outliers present in the vector map.

If a vector is judged to be spurious, it is often useful to replace it rather than leaving a gap in the map. In the case of the mean algorithm, replacement by the mean of the outlier's nearest neighbours is undesirable, as it has the effect of smoothing the data, which is already a low-pass filtered representation of the fluid motion. For the median algorithm, replacing the outlier with the median value is acceptable; indeed such a method is frequently used in image processing to replace noisy pixel values [81]. This method works because the median of a vector and its nearest neighbours is likely to correspond to one of the valid vectors

in the locality [43].

B.0.2 Coherence Algorithm

The mean and median algorithms tend to begin at one corner of the vector map and scan through it, row by row or column by column, testing each vector in turn. Such routines are straightforward to program, but to not represent how a human being would perform the validation. Data validation by an actual person seems to involve locating a zone where the vector field is coherent, and tracking local gradients in the field to identify spurious vectors significantly different from their coherent neighbours. Nogueira et al. [82] propose an algorithm that emulates this approach, by selecting a region where neighbouring vectors are similar and looping outwards to determine whether or not a vector belongs to the zone of coherence.

To determine whether a group of vectors is coherent, they calculated

$$val = \frac{\sum_i |v_i - v_0|}{\sum_i |v_i|} \tag{B.1}$$

where v_0 is the velocity of the central vector and v_i is the velocity of its 8 nearest neighbours. The vectors at the position where this value is a minimum are then validated. Once this has been done, the algorithm loops around this zone, comparing each vector in turn to the mean of the validated vectors. If they differ

by less than a user-defined amount, they too are validated; otherwise they are rejected. When no further vectors are validated, the algorithm looks for other zones of coherence.

This method is more effective than the median algorithm when there are clusters of outliers or discontinuous flow fields such as occur in turbulent jets in still water.

B.1 Validation Condition

The process of validation is complicated by the fact that a velocity vector by definition has both magnitude and direction. A vector can be an outlier if *either* quantity is significantly different from its neighbours. For a vector to be judged valid, it should therefore pass one condition for each component i.e. two for traditional 2d PIV or three for 3d PIV. Many validation programs ignore this problem and consider magnitude alone.

As mentioned previously, a vector is frequently compared to its nearest neighbours to determine whether or not it should be validated. Thus a typical validation condition for the x component is

$$comp_x = \frac{v_x - v_n}{v_n} < \epsilon_{thresh} \tag{B.2}$$

where v_x is the x component of the test vector's velocity, v_n is the comparison vector (e.g. mean or median of the nearest neighbours, or mean of the validated neighbours). If $comp_x$ is less than a user defined tolerance, ϵ_{thresh}, typically of the order 0.25, the x component is judged to be acceptable. A vector would need to pass this condition, plus equivalent conditions for the other velocity components, to be approved.

Although this approach works in principle, since it reveals vectors whose velocities are significantly different from their neighbours, there are two significant problems. Firstly, if a vector is near the horizontal or vertical, v_n will be close to zero, so the calculation of *comp* suffers from ill-conditioning. The *comp* term could therefore be arbitrarily large even though, to the human eye, the vectors appear to be valid. Another difficulty with this approach is regions where vectors may differ significantly from their neighbours, but in a regular way, for instance in vortices.

Both of these scenarios can be avoided by adding a mean velocity to the flow prior to validation, then subtracting the velocity afterwards, similar to the method of image shifting in auto-correlation PIV. The difficulty then is automatically determining an appropriate shift velocity.

The validation condition can be defined as an absolute comparison, rather than the relative comparison in equation B.2:

$$|v_x - v_n| < \epsilon_{thresh} \tag{B.3}$$

Although this removes the difficulty of ill-conditioning, choosing an appropriate value for ϵ_{thresh} is more difficult, especially in flows where there is a large range of flow velocities throughout the experiment.

B.1.1 Multiple Peak Validation

Outliers occur when the highest peak in the correlation plane does not correspond to the mean displacement between particle pairs, but to a random correlation between distinct particles. Nevertheless, a peak representing this mean displacement may still be present in the correlation plane, hidden by the noise peak.

The author's PIV analysis software allowed the option of storing locations of three subsidiary peaks. Then, if a vector is judged to be spurious, it is not simply rejected. Instead, the algorithm uses the position of the subsidiary peaks in turn to produce a new vector. This vector is then compared to its neighbours, and either accepted or rejected. If rejected, the next highest peak location is used, until the four highest peaks have all been tested. Only vectors which fail each of the four tests is labelled as an outlier. By using this approach, more valid vectors are obtained and there is less need for interpolation which results in

greater statistical independence between the velocity measurements.

This approach uses the correlation planes obtained from the raw images, rather than just the resulting vector map, to validate the velocity measurements. More sophisticated versions of this approach are undergoing development. Mark Wernet's PIVPROC software, widely used at NASA, uses fuzzy logic to determine the true particle displacement, even when it does not correspond to the highest peak in the correlation plane [46], [47],[83],[84]. A fuzzy processor evaluates possible particle paths from neighbouring correlation planes, and uses flow continuity to establish the most probable displacement. Such a method is similar to how a human would perform the validation, and also results in higher spatial resolution, as discussed in section 4.8.

B.2 Replacement of Missing Vectors

The velocity maps obtained from PIV experiments are often used to calculate properties of the motion such as vorticity, shear and momentum transfer. In order to accurately evaluate these quantities, it is necessary to have an accurate velocity value for each grid point. For this reason, it is often useful to replace the rejected velocities with more realistic values.

There are three possibilities for obtaining new improved velocity values for the deleted vectors: interpolation, extrapolation and filtering [82]. Interpolation

involves replacing a vector by a weighted mean of its neighbours, for instance a Gaussian, whose width is sufficiently small that low-pass filtering is minimised [36]. This approach is most effective if the outlier is isolated. If however, there is a cluster of outliers, a more effective method is to initially assign *reasonable* values to the gaps then filter these values. A discussion of filter criteria can be found in [85]. Extrapolation tends to amplify errors and is not generally used.

Appendix C

Papers Published

T. Schlicke, A. Arnott, J. Buick, C. Greated, N. Thomas (2001) "The Application of LIF to Study the Dispersion of a Surface Film Due to Wave Breaking Using a Two Camera System"

To appear in Surface Slicks and Remote Sensing of Air-Sea Interactions

Professional Engineering Publishing Limited

T. Schlicke, J. Buick, A. Arnott, C. Greated, N. Thomas (2000) "Effect of Surface Films on Wave Amplitude and Dispersion of a Film by Breaking Waves"

Submitted to Surface Slicks and Remote Sensing of Air-Sea Interactions

E. Schlicke, A. D. Arnott, J. M. Buick, J. Pullen, N. H. Thomas and C. A. Greated (2000) "Studies of the Interactions Between Surface Films and Water Waves" *Euromech Colloquium 416, Genova*

T. Schlicke, C. Greated (1999) "Application of LIF and PIV to dispersion of surface films" *Laser Anemometry Advanced and Applications, Rome*

T.Schlicke, C. Greated "PIV Fuzzy Logic Data Validation" (1999) *Scottish Fluid Dynamics Meeting, Glasgow*

T. Schlicke "Collection and Validation of 3D PIV data" (1998) *Mini-Symposium on Optical Techniques for Flow Diagnosis, Grasmere*

Bibliography

[1] Joel E. Cohen et al. Estimates of Coastal Populations. *Science (in Letters)*, 14:1209–1213, 1997.

[2] George L. Mellor. *Introduction to Physical Oceanography.* Springer, 1996.

[3] Robert A. Dalrymple Robert G. Dean. *Water Wave Mechanics for Engineers and Scientists.* World Scientific, 1993.

[4] Ivar G. Jonsson Ib A. Svendsen. *Hydrodynamics of Coastal Regions.* Technical University, Denmark, 1982.

[5] N. Emarat. *Particle Image Velocimetry Experiments on Surf-Zone Breaking Waves.* PhD thesis, University of Edinburgh, 2000.

[6] J. McCowan. On the Highest Wave of Permanent Type. *Philos. Mag. J.Sci*, 38, 1894.

[7] M.S. Longuet-Higgins. Progress Toward Understanding How Waves Break. *Twenty-First Symposium on Naval Hydrodynamics*, 1997.

[8] H. Qiao J. H. Duncan, V. Philomin and J. Kimmel. The Formation of Spilling Breaking Waves. *Phys. Fluids*, 6:2258–2260, 1994.

[9] T. Sawaragi. *Coastal Engineering- Waves, Beaches, Wave-Structure Interactions.* Elsevier, 1995.

[10] E. D. Christensen. *Turbulence in Breaking Waves: A Numerical Investigation.* PhD thesis, Tech. Univ. Denmark, 1998.

[11] Kuang-An Chang and Philip L.-F. Liu. Velocity, Acceleration and Vorticity under a Breaking Wave. *Phys. Fluids*, 10:327–329, 1998.

[12] J. T. Scott U. Lemmin and U. H. Czapski. The Development from Two-dimensional to Three-dimensional Turbulence Generated by Breaking Waves. *Journal of Geophysical Research*, 19:3442–3448, 1974.

[13] Pengzhi Lin and Philip L.-F. Liu. Turbulence Transport, Vorticity Dynamics, and Solute Mixing under Plunging Breaking Waves in Surf Zone. *Journal of Geophysical Research*, 103:15,677–15,694, 1998.

[14] T. Haydon. *Turbulence and Vorticity Generated by Breaking Waves.* PhD thesis, University of Edinburgh, 1997.

[15] Chanson H. Unsteady Air Bubble Entrainment at a Plunging Breaker: A Full-Scale Model. *Euromech Colloquium 416*, 2000.

[16] P. Bonmarin. Geometric Properties of Deep-Water Breaking Waves. *J. Fluid Mech.*, 209:405–433, 1989.

[17] R. J. Rapp and W. K. Melville. Laboratory Measurements of Deep Water Breaking Waves. *Phil. Trans. R. Soc. Lond.*, 331:735–800, 1989.

[18] Grant R. Bigg. *The Oceans and Climate*. Cambridge University Press, 1996.

[19] Physical Processes in the Microlayer and the Air-Sea Exchange of Trace Gases. *Gesamp Reports and Studies*, 59, 1995.

[20] John Scott. Private Communication, 2000.

[21] B. Franklin. Of the Stilling of Waves by means of Oil. *Philosophical Transactions*, 64:445–460, 1774.

[22] John Scott. *Oil on Troubled Waters*. Multi-Science Publication Co, 1979.

[23] E.H. Lucassen-Reynders and J. Lucassen. Properties of Capillary Waves. *Advances In Colloid and Interface Science*, 2:347–395, 1969.

[24] G. Rovener K. Dysthe and Y. Rabin. Damping of Capillary Waves by Polymeric Monolayers. Comparison with Hydrodynamic Theory. *Journal of Physical Chemistry*, 90:3894–3895, 1986.

[25] J. Pullen. *Particle Image Velocimetry Applied to Waves with Surface Active Films*. PhD thesis, University of Edinburgh, 1998.

[26] Horace Lamb. *Hydrodynamics*. Cambridge University Press, 1959.

[27] Heinrich Hühnerhuss Werner Alpers. The Damping of Ocean Waves by Surface Films: A New Look at an Old Problem. *Journal of Geophysical Research*, 94:6251–6265, 1989.

[28] J. Aitken. On the Effect of Oil on a Stormy Sea. *Proc. Roy. Soc. Edin.*, 12:56–75, 1883.

[29] Gregory Gartrell E. John List and Clinton D. Winant. Diffusion and Dispersion in Coastal Waters. *ASCE Journal of Hydraulic Engineering*, 116:1158–1179, 1990.

[30] Herterich K. and Hasselmann K. The Horizontal Diffusion of Tracers by Surface Waves. *Journal of Physical Oceanography*, 12:704–711, 1982.

[31] Durrani T.S. Greated C.A. Buick J. M., Morrison I.G. Particle Diffusion on a Three-dimensional Random Sea. *Experiments in Fluids*, 30:88–92, 2001.

[32] Brian G. Sanderson and David A. Booth. The Fractal Dimension of Drifter Trajectories and Estimates of Horizontal Eddy-Diffusivity. *Tellus*, 43A:334–349, 1991.

[33] A. Provenzale A.R. Osborne, A.D. Kirwan and L. Bergamasco. Fractal Drifter Trajectories in the Kuroshio Extension. *Tellus*, 41A:416–435, 1989.

[34] D. Skyner. *The Mechanics of Extreme Water Waves*. PhD thesis, University of Edinburgh, 1992.

[35] D. R. McCluskey C. Gray, C. A. Greated and W. J. Easson. An Analysis of the Scanning Beam PIV Illumination System. *Meas. Sci. Technol.*, 2:717–724, 1991.

[36] C. Willert M. Raffel and J. Kompenhans. *Particle Image Velocimetry A Practical Guide*. Springer, 1998.

[37] T. Dewhirst. *Multiple CCD Array Digital Particle Image Velocimetry*. PhD thesis, University of Edinburgh, 1998.

[38] E. Hecht. *Optics*. Springer, 1998.

[39] K.H. Drexhage. *Structure and properties of laser dyes*. Springer, 1973.

[40] A. Shawcross. PhD thesis, University of Edinburgh, 2001.

[41] A. Arnott C. Greated N. Thomas T. Schlicke, J. Buick. Effect of Surface Films on Wave Amplitude and Dispersion of a Film by Breaking Waves. *Submitted to Surface Slicks and Remote Sensing of Air-Sea Interactions*, 2000.

[42] H.C. van de Hulst. *Light Scattering by Small Particles*. Dover Publications, Inc., 1981.

[43] J. Westerweel. *Digital Particle Image Velocimetry*. Delft University Press, 1993.

[44] I. G. Morrison. *The Hydrodynamic Performance of an Oscillating Water Column Wave Energy Converter*. PhD thesis, University of Edinburgh, 1995.

[45] R. J. Adrian R. D. Keane and Y. Zhang. Super-Resolution Particle Image Velocimetry. *Meas. Sci. Technol.*, 6:754–768, 1995.

[46] Mark P. Wernet. Fuzzy Logic Enhanced Digital PIV Processing Software. *18th International Congress on Instrumentation for Aerospace Simulation Facilities*, 1999.

[47] Mark P. Wernet. Fuzzy Inference Enhanced Information Recovery from Digital PIV Using Cross-Correlation Combined with Particle Tracking. *SPIE Conference on Optical Diagnostics in Fluid and Thermal Flow*, 2546, 1995.

[48] M. Raffel O. Ronneberger T. P. Dewhirst, J. Kompenhans. Advanced Evaluation Methods in Particle Image Velocimetry.

[49] Klaus D. Hinsch. Three-dimensional Particle Velocimetry. *Meas. Sci. Technol.*, 6:742–753, 1995.

[50] N. J. Lawson and J. Wu. Three-dimensional Particle Velocimetry: Experimental Error Analysis of a Digital Angular Stereoscopic System. *Meas. Sci. Technol.*, 8:1455–1464, 1997.

[51] O. Ronneberger M. Raffel, M. Gharib and J. Kompenhans. Feasibility Study of Three-dimensional PIV by Correlating Images of Particles within Parallel Light Sheets. *Experiments in Fluids*, 19:69–77, 1995.

[52] Willert C Gharib M Raffel M, Westerweel J and Kompnhans J. Analytical and experimental investigations of dual-plane particle image velocimetry. *Opt Eng.*, 1996.

[53] C. Willert O. Ronneberger M. Raffel, A. Derville and J. Kompenhans. Dual-Plane Correlation for Three-dimensional Particle Image Velocimetry on Planar Domains.

[54] Ch. Brucker. 3-d PIV via Spatial Correlation in a Color-Coded Light-sheet. *Experiments in Fluids*, 21:312–314, 1996.

[55] G.E.A. Meier B. Stasicki. A Computer Controlled Ultra High-Speed Video Camera System. *SPIE Proceedings*, 2513:196–208, 1995.

[56] Will Hossack. Private Communication, 2000.

[57] D. Saupe H. Peitgen, H. Jurgens. *Chaos and Fractals New Frontiers of Science.* Springer-Verlag, 1992.

[58] Paul S. Addison. *Fractals and Chaos.* Institute of Physics Publishing, 1997.

[59] Pablo Huq. Private Communication, 1999.

[60] Julian Scott Jean Mathieu. *An Introduction to Turbulent Flow.* Cambridge University Press, 2000.

[61] C. Meneveau K.R. Sreenivasan. The Fractal Facets of Turbulence. *Journal of Fluid Mechanics*, 173:357–386, 1986.

[62] S. Lovejoy. Area-Perimeter Relation for Rain and Cloud Areas. *Science*, 216:185–187, 1982.

[63] Benoit Mandelbrot. How Long Is the Coast of Britain? *World Treasury of Physics, Astronomy and Mathematics.*, 1991.

[64] Bryan R. Kerman and Lucie Bernier. Multifractal Representation of Breaking Waves on the Ocean Surface. *Journal of Geophysical Research*, 99:16,179–16,196, 1994.

[65] Alistair Nisbet Paul S. Addison, Bo Qu and Gareth Pender. A Non-Fickian, Particle-Tracking Diffusion Model Based on Fractional Brownian Motion. *International Journal For Numerical Methods in Fluids*, 25:1373–1384, 1997.

[66] A.S. Ndumu L.T. Dougan P.S. Addison, W.M.C. McKenzie and R. Hunter. Fractal Cracking of Concrete: Parameterization of Spatial Diffusion. *Journal of Engineering Mechanics*, 125(6), 1999.

[67] Benoit Mandelbrot. A Multifractal Walk down Wall Street. *Scientific American*, 1999.

[68] Terry Sincich William Mendenhall. *Statistics for Engineering and the Sciences.* Dellen Publishing, 3rd edition, 1992.

[69] D.J. Tritton. *Physical Fluid Dynamics.* Oxford Science Publications, 1988.

[70] Robert C.Y. Koh Jörg Imberger Norman H. Brooks Hugo B. Fischer, E. John List. *Mixing in Inland and Coastal Waters.* Academic Press, Inc., 1979.

[71] G. I. Taylor. Diffusion by Continuous Moments. *Proceedings of the London Mathematical Society*, 20:196–212, 1922.

[72] Lewis F. Richardson. Atmospheric Diffusion shown on a Distance-Neighbour Graph. *Proc. R. Soc. Londo, Series An*, 110:709–737, 1926.

[73] Paul E. Dimtakis. Recent Advances in Turbulent Mixing. *Caltech ASCI Technical Report 065*, 2000.

[74] Howell Peregrine. Private Communication, 2000.

[75] K.R. Sreenivasan R.R. Prasad. The Measurement and Interpretation of Fractal Dimensions of the Scalar Interface in Turbulent Flows. *Physics of Fluids A*, 2:792–807, 1990.

[76] James A. Viecelli. Structure of Lagrangian Turbulence. *Phys. Fluids A*, 11:1836–1843, 1989.

[77] P.A. Quinn. *Breaking Waves on Beaches.* PhD thesis, University of Edinburgh, 1995.

[78] U. Frisch. *Turbulence.* Cambridge University Press, 1995.

[79] T. Sakai J.A. Battjes. Velocity Field in a Steady Breaker. *J. Fluid Mech.*, 111:421–437, 1981.

[80] D Dabiri H Huang and M Gharib. On Errors of Digital Particle Image Velocimetry. *Meas. Sci. Technol.*, 8:1427–1440, 1997.

[81] Richard E. Woods Rafeal C. Gonzalez. *Digital Image Processing.* Addison-Wesley Publishing Company, 1993.

[82] A Lecuona J Nogueira and P A Rodríguez. Data validation, False Vectors Correction and Derived Magnitudes Calculation on PIV Data. *Meas. Sci. Technol.*, 8:1493–1501, 1997.

[83] Mark P. Wernet. Fuzzy Logic Particle Tracking Velocimetry. *SPIE Conference on Optical Diagnostics in Fluid and Thermal Flow*, 2005, 1993.

[84] Mark P. Wernet. Particle Image Velocimetry Processing: PIVPROC.

[85] P A Rodríguez J Nogueira, A Lecuona and U. Ruiz-Rivas. On the design of some PIV postprocessing filters. *Laser Anemometry Advances and Applications*, pages 483–490, 1997.